Technische Universität München
TUM School of Natural Sciences

Highly Defined Supports for Near-ambient Pressure Investigations of Model Catalysts

Matthias Bruno Krinninger

Vollständiger Abdruck der von der TUM School of Natural Sciences der Technischen Universität München zur Erlangung eines

Doktors der Naturwissenschaften (Dr. rer. nat.)

genehmigten Dissertation.

Vorsitz: Priv.-Doz. Dr. Friedrich Esch

Prüfende der Dissertation:

1. Prof. Dr. Barbara A. J. Lechner
2. Prof. Dr. Marc-Georg Willinger
3. Prof. Dr. Jeppe V. Lauritsen

Die Dissertation wurde am 20.11.2024 bei der Technischen Universität München eingereicht und durch die TUM School of Natural Sciences am 05.12.2024 angenommen.

List of Publications and Conference Contributions

Publications that are part of this thesis

- Matthias Krinninger, Nicolas Bock, Sebastian Kaiser, Johanna Reich, Tobias Bruhm, Felix Haag, Francesco Allegretti, Ueli Heiz, Klaus Köhler, Barbara A. J. Lechner and Friedrich Esch
  On-Surface Carbon Nitride Growth from Polymerization of 2,5,8-Triazido-s-heptazine
  Chemistry of Materials **2023**, *35*, 6762–6770.
  DOI: 10.1021/acs.chemmater.3c01030

- Matthias Krinninger, Florian Kraushofer, Nils B. Refvik, Monika Blum, Barbara A. J. Lechner
  Interface Effects in the Stability of 2D Silica, Silicide, and Silicene on Pt(111) and Rh(111)
  ACS Applied Materials & Interfaces **2024**, *16*, 27481–27489.
  DOI: 10.1021/acsami.4c05137

- Florian Kraushofer*, Matthias Krinninger*, Sebastian Kaiser, Johanna Reich, Agnieszka Jarosz, Matthias Füchsl, Gaurav Anand, Friedrich Esch and Barbara A. J. Lechner (*These authors contributed equally)
  The influence of bulk stoichiometry on near-ambient pressure reactivity of bare and Pt-loaded rutile TiO_2(110)
  Nanoscale **2024**, *16*, 17825–17837.
  DOI: 10.1039/D4NR01702A

Publications beyond the scope of this thesis

- Sebastian Kaiser*, Johanna Plansky*, Matthias Krinninger, Andrey Shavorskiy, Suyun Zhu, Ueli Heiz, Friedrich Esch and Barbara A. J. Lechner (*These authors contributed equally)
  Does Cluster Encapsulation Inhibit Sintering? Stabilization of Size-Selected Pt Clusters on Fe_3O_4(001) by SMSI
  ACS Catalysis **2023**, *13*, 6203–6213.
  DOI: 10.1021/acscatal.3c00448

- Johanna Reich*, Sebastian Kaiser*, Alexander Bourgund, Matthias Krinninger, Ueli Heiz, Friedrich Esch and Barbara A.J. Lechner (*These authors contributed equally)
  Exploring the atomic-scale dynamics of Fe_3O_4(001) at catalytically relevant temperatures using FastSTM
  Surface Science **2025**, *752*, 122634.
  DOI: 10.1016/j.susc.2024.122634

Conference contributions

- Matthias Krinninger, Florian Kraushofer, Friedrich Esch and Barbara A. J. Lechner
  Presentation: *Near-ambient pressure studies of size selected clusters on ultrathin silica films*
  DPG Meeting of the Condensed Matter Section, Regensburg, September 2022

- Matthias Krinninger, Florian Kraushofer, Nils Refvik, Monika Blum and Barbara A. J. Lechner
  Presentation: *Growth of ultrathin silica films on Pt(111) and Rh(111): Influence of intermixing with the support*
  AVS 69th International Symposium and Exhibition, Portland (Oregon), November 2023

- Matthias Krinninger, Florian Kraushofer, Matthias Füchsl, Sebastian Kaiser, Johanna Reich, Monika Blum and Barbara A. J. Lechner
  Presentation: *Titania ≠ Titania: How the degree of reduction influences SMSI-induced Pt encapsulation*
  Workshop Advanced Spectroscopy for Energy Storage & Conversion, Munich, January 2024

Presentations at international network status meetings

- Matthias Krinninger, Nicolas Bock, Sebastian Kaiser, Johanna Plansky, Astrid De Clerq, Tobias Bruhm, Francesco Allegretti, Ueli Heiz, Barbara A. J. Lechner, Klaus Köhler and Friedrich Esch
  Presentation: *On-Surface Carbon Nitride Growth from Polymerization of 2,5,8-Triazido-s-heptazine*
  TUM-IAS "Exchange of Ideas Meeting" with the group of Ib Chorkendorff (DTU), Garching, April 2022

- Matthias Krinninger, Florian Kraushofer, Friedrich Esch and Barbara A. J. Lechner
  Presentation: *2D-Silica as a Cluster Support Material*
  ATUMS annual meeting, Bernried, November 2022

- Matthias Krinninger, Florian Kraushofer, Nils Refvik, Monika Blum, Friedrich Esch and Barbara A. J. Lechner
  Presentation: *Growth of ultrathin silicon dioxide films on Pt(111) and Rh(111): Influence of intermixing with the support*
  ATUMS annual meeting, Canmore, November 2023

Open source software and libraries

- proespm-py3: `https://github.com/matkrin/proespm-py3`
- quickplot: `https://github.com/matkrin/quickplot`
- gwy-z-module: `https://github.com/matkrin/gwy-z-module`
- xps-peaks: `https://github.com/matkrin/xps-peaks`
- spm-rs: `https://github.com/matkrin/spm-rs`
- vamas: `https://github.com/matkrin/vamas` or `https://pypi.org/project/vamas`
- mulfile: `https://github.com/matkrin/mulfile` or `https://pypi.org/project/mulfile`
- sm4file: `https://github.com/matkrin/sm4file` or `https://pypi.org/project/sm4file`

Abstract

Heterogeneous catalysis is a key tool for sustainable energy and chemical processes, yet our fundamental knowledge of the underlying mechanisms is incomplete. One particular challenge arises from the pressure gap between laboratory-scale experiments and conditions applied in industrial-scale reactions, which led to the development of near-ambient pressure (NAP) methods. In this thesis, a new NAP scanning tunneling microscopy (NAP-STM) setup was commissioned, further functionalities added, and data management tools developed. Moreover, three studies present different support materials and evaluate their suitability as model catalyst supports.

The first study introduces a novel, metal-free carbon nitride thin film synthesized on Au(111) following different reaction pathways. X-ray illumination and the resulting emission of secondary electrons, UV light illumination and subsequent annealing of the stable intermediate, and a merely thermal activation all lead to an amorphous, not fully closed, but mainly uniform 2D film.

The second study compares 2D silica films on Pt(111) and Rh(111). On Pt(111), fully closed films were achieved by creation of an interfacial buffer layer between the film and the underlying metal. This film shows a high stability against CO atmospheres at near-ambient pressures. On Rh(111), films with different morphologies could be synthesized successfully, but never a completely closed layer. In contrast to many other metal substrates, the film is fully reducible at high temperatures, forming a well-ordered silicide.

The third study explores two different TiO_2 rutile samples, one near-stoichiometric and the other highly-reduced, showing contrasting surface reactivity under the same, NAP atmospheres of O_2, CO_2, H_2 and CO at 600 K. The highly-reduced TiO_2 undergoes surface redox reactions, while the near-stoichiometric sample is more inert, in turn affecting their interaction with Pt nanoparticles.

Additional contributions include the design and construction of new Faraday cups for two cluster generation setups, enhancing cluster beam characterization and sample preparation as well as enabling studies of size-selected clusters under near-ambient pressure. Furthermore, software tools for data analysis and management that are aligned with FAIR principles to streamline and structure experimental data workflows have been developed.

Zusammenfassung

Die heterogene Katalyse ist ein Schlüsselinstrument für nachhaltige Energie- und Chemieprozesse, doch unser grundlegendes Wissen über die zugrunde liegenden Mechanismen ist unvollständig. Eine besondere Herausforderung ergibt sich aus der Drucklücke ("pressure gap") zwischen Experimenten im Labormaßstab und den Bedingungen, die bei Reaktionen im industriellen Maßstab angewandt werden, was zur Entwicklung von Methoden bei Umgebungsdruck (NAP) führte. In dieser Arbeit wurde ein neuer NAP-Rastertunnelmikroskopie-Aufbau (NAP-STM) in Betrieb genommen, weitere Funktionalitäten hinzugefügt und Datenmanagement-Tools entwickelt. Außerdem werden in drei Studien verschiedene Trägermaterialien vorgestellt und ihre Eignung als Modellkatalysatorträger bewertet.
Die erste Studie stellt eine neuartige, metallfreie Kohlenstoffnitrid-Dünnschicht vor, die auf Au(111) durch verschiedene Reaktionswege synthetisiert wurde. Röntgenbeleuchtung und die daraus resultierende Emission von Sekundärelektronen, UV-Licht-Beleuchtung und anschließendes Ausheizen des stabilen Zwischenprodukts sowie eine lediglich thermische Aktivierung führen zu einem amorphen, nicht vollständig geschlossenen, aber weitgehend gleichmäßigen 2D-Film.
Die zweite Studie vergleicht 2D-Siliziumoxid auf Pt(111) und Rh(111). Auf Pt(111) wurden vollständig geschlossene Filme durch die Schaffung einer Grenzflächenpufferschicht zwischen dem Film und dem darunter liegenden Metall erreicht. Dieser Film weist eine hohe Stabilität gegenüber CO-Atmosphären bei nahezu Umgebungsdruck auf. Auf Rh(111) konnten Filme mit unterschiedlichen Morphologien erfolgreich synthetisiert werden, jedoch nie eine vollständig geschlossene Schicht. Im Gegensatz zu vielen anderen Metallsubstraten ist dieser Film bei hohen Temperaturen vollständig reduzierbar und bildet ein geordnetes Silizid.
Die dritte Studie untersucht zwei verschiedene TiO_2-Rutilproben, eine nahezu

stöchiometrische und die andere hochreduziert, welche unter den gleichen NAP-Atmosphären von O_2, CO_2, H_2 und CO bei 600 K eine unterschiedliche Oberflächenreaktivität aufweisen. Das stark reduzierte TiO_2 unterliegt Redoxreaktionen an der Oberfläche, während die nahezu stöchiometrische Probe reaktionsträge ist, was sich wiederum auf ihre Wechselwirkung mit Pt-Nanopartikeln auswirkt.
Zu den weiteren Beiträgen gehören die Entwicklung und der Bau neuer Faraday-Becher für zwei Clustergenerierungsanlagen, die die Charakterisierung von Clusterstrahlen und die Probenvorbereitung verbessern und Studien von Clustern mit ausgewählten Größen unter nahezu Umgebungsdruck ermöglichen. Darüber hinaus wurden Software-Tools für die Datenanalyse und -verwaltung entwickelt, die sich an den FAIR-Prinzipien orientieren, um experimentelle Datenabläufe zu rationalisieren und zu strukturieren.

Contents

1 Introduction

Catalysis plays a critical role in modern chemistry, enabling efficient and selective chemical transformations that are fundamental to various industries, including petrochemical and refinery[1,2], in processes like, e.g., cracking, reforming, hydrotreating and hydrocracking or chemical synthesis.[3,4] Prominent examples are the production of ammonia, sulfuric acid or methanol. Further, the areas of pharmaceuticals[5,6], renewable and environmentally friendly energy[7,8] (e.g., fuel cells, biofuel production), textile and polymer industry[9,10] (e.g., fiber polymerization like nylon, dye manufacturing) as well as agriculture[3] (fertilizer, pesticide production), vastly benefit from the progress in catalytic processes since first observations in the late 17th / early 18th century.[11]

In particular, heterogeneous catalysis, in which catalysts in a different phase than the reactants facilitate key reactions on their surfaces, is in the focus of the industrial usage.[8,12] A typical example of a heterogeneous catalyst can consist of a support material, often an oxide in the form of granules, pellets or powders on which a small amount of catalytically active metal is dispersed. Despite the extensive applications and advancements in catalysis across various industries, a deeper understanding of the fundamental mechanisms governing catalytic processes remains essential. This is where model catalysis comes into play. By focusing on simplified, well-defined systems, model catalysis allows for the investigation of surface interactions and reaction mechanisms at the atomic level. These studies provide valuable insights into the nature of active sites, reaction pathways, and the influence of different parameters on catalytic behavior. This knowledge then helps in the development of new catalysts with enhanced capabilities, ultimately bridging the gap between fundamental research and industrial applications.

Advances in surface science and computational chemistry have significantly expanded our understanding of model catalytic systems. The advent of experimental techniques such as low energy electron diffraction (LEED, 1960s)[13], X-ray photoelectron spectroscopy (XPS, 1960s)[14] and scanning tunneling microscopy (STM, 1980s)[15] as well as computational methods like density functional theory (DFT, 1960s)[16,17] calculations have provided atomic-level insights into these atomic-scale mechanisms.

Building on these methods, model catalysis using size-selected metal clusters has emerged as a powerful approach to further unravel the complexities of catalytic systems. By generating and studying clusters with a precisely controlled number of atoms, observations in the non-scalable size regime become possible. In this regime, with typical cluster sizes of fewer than 100 atoms, the behavior of the material cannot be extrapolated from its bulk properties because of the presence of discrete energy levels rather than a continuous band structure, as found in bulk materials. This is often referred to as the quantum size effect.[18] For example, Au as a bulk material is relatively inert, but Au clusters were shown to have an increased activity in the CO oxidation reaction, which is most pronounced in bilayer clusters due to the emergence of a band gap.[19] This quantization of the electronic structure leads to a high sensitivity to the number of atoms where the addition or the removal of a single atom can drastically alter the properties of the cluster.[20] More precisely, unlike single crystals, small isolated clusters can exhibit structures of altering symmetry depending on the number of atoms, which influences the degeneracy of their electronic states, i.e., a break in symmetry leads to a lower degeneracy, as well as the availability of low coordination adsorption sites.[21,22] Moreover, clusters in this non-scalable size regime show a high surface-to-volume ratio, i.e., a large fraction of atoms is exposed to the surface, where catalytic reactions occur, which can lead to an enhancement in catalytic activity or selectivity. Additionally, changes in the geometric arrangement of atoms within these small clusters, such as the dynamic structural fluxionality between structural isomers, can further influence their properties.[23]

For the creation of these size-selected clusters in the gas phase, specialized cluster generation setups need to be used. Techniques such as arc discharge[24], laser ablation[25] or (magnetron) sputtering[26], involve vaporizing a target material and allowing it to cool and condense into clusters. The cluster nucleation is influenced by various parameters such as temperature, pressure, and the type of material being used. For filtering out a single cluster size, a mass spectrometry-based approach where clusters are separated based on their mass-to-charge ratio (m/z) using a mass filter (e.g., quadrupole or time-of-flight) is employed.

Once generated, these size-selected clusters can be investigated in the gas phase by using an ion trap.[27,28] However, in order to closer mimic catalysts that are employed in industrial scale reactions, it is necessary to deposit them onto well-defined substrates, where their interaction with the surface becomes a key factor in determining their properties.[29] Again, as they are widely used in industry, metal oxides, and their thin films are of particular interest as catalyst supports. Upon landing on the surface, the clusters can undergo structural changes, electronic redistribution and form new chemical bonds with the substrate, which can further influence their catalytic activity. Further, the interaction of reactant molecules with the surface, like diffusion behavior, spillover[30] or reverse spillover[31] becomes an additional factor in reaction mechanisms.[32] A reducible oxide support like magnetite can even provide lattice oxygen atoms that can contribute to reactions.[33] An additional factor is the acidity of the oxide, as shown in a recent study about the ethylene hydrogenation catalyzed by platinum. For the same cluster size (Pt_{13}), a change from an acidic (electron accepting) SiO_2 to a basic (electron donating) MgO thin film changed the reaction rate drastically.[34] Furthermore, the former system of Pt_{13} on SiO_2 shows different reaction rates for the same reaction, depending on the stoichiometry of the silica where an oxygen-rich film showed increased activity.[35] Another important mechanism, often referred to as strong metal-support interaction (SMSI), plays a critical role in the stabilization as well as in the modification of reactivity[36], selectivity[37,38] and sintering behavior[39] of clusters and nanoparticles, by encapsulation of the metal by the oxide.[40–46]

Understanding how these clusters and nanoparticles behave when supported is essential for translating insights from isolated systems into real-world applications, where catalysts must function in complex environments and under practical conditions. However, challenges remain in bridging the gap between these idealized systems and the complexity of industrial catalysts. One of these challenges is the "complexity gap", i.e., the fact that model catalysis investigates simplified systems of well defined surfaces with adsorbed nanoparticles and clusters while applied catalysts are in the form of powders, often with pores that are not easily accessible for atomic-scale characterization. Additionally, many of these surface science characterization techniques traditionally need to operate in ultra high vacuum (UHV), either because a contaminant-free surface is needed or the inelastic mean free path (IMFP) of the probe particles would be otherwise too short which also differs significantly from applied processes. Hence, relatively new advances in the instrumentation of, e.g., scanning tunneling microscopy (STM) and X-ray photoelectron spectroscopy (XPS) strive towards the feasibility of measurements in higher pressure regimes with the goal of closing this "pressure gap".

One of the aims of this thesis is to evaluate a carbon-based, a non-reducible, and a reducible oxide surface as model supports for fundamental studies in heterogeneous catalysis and to tackle the challenge of the pressure gap. Therefore, a new UHV system with a near ambient pressure STM (NAP-STM) was successfully commissioned and further extended, which is described in the following chapter. Furthermore, chapter 2 and 3 provide an overview of measurement techniques and self-written analysis software that were used throughout this thesis, respectively. In order to produce well-defined model systems, two Faraday cups were built as characterization devices of cluster beams in, firstly, a well-established laser ablation cluster source and, secondly, a new magnetron sputter source. Once finished, the latter will open the door for future studies of size-selected clusters inside the NAP-STM. Chapter 4 gives detailed information about design decisions and how the constructions of these new Faraday cups were implemented. Chapter 5 provides three key publications from this thesis that aims to contribute to our understanding of model catalysts, particularly with a focus on the support material and, to some extent, its interaction with catalytically active nanoparticles. As men-

tioned, the substrate's influence can be a key factor in the catalytic activity thus we investigated the synthesis of a novel thin film made from a carbon nitride precursor, a material that shows promising properties, especially in photocatalysis[47–50] but also, combined with highly oriented pyrolytic graphite (HOPG), as a novel, cheap and metal-free support with defined anchoring centers for single atoms and clusters.[51,52] Furthermore, to gain deeper insights into the stability of vitreous silica bilayer thin films, which make the – as a bulk material – non-conductive SiO_2 accessible to STM, we compared their growth and properties on two different single crystals, viz. Pt(111) and Rh(111). The last study shines deeper light on the interaction of Pt nanoparticles with TiO_2 and various gas atmospheres at near-ambient conditions. The insights gained from these studies may help improve our understanding of catalytic processes and could contribute to the development of more effective and sustainable catalysts.

2

Experimental Methods

UHV conditions, typically defined as pressures below 10^{-8} mbar, are crucial for maintaining extremely clean surfaces. At higher pressures, even trace amounts of gas can adsorb onto surfaces and thus contaminate them. This can easily be seen by the relation between the impingement rate Z_{w}, i.e., the number of gas atoms or molecules hitting a surface per unit of time and the pressure p in the Hertz-Knudsen equation

$$Z_{\mathrm{w}} = \alpha \frac{p}{\sqrt{2\pi m k_{\mathrm{B}} T}}, \tag{2.1}$$

where α is the sticking coefficient, i.e., the probability of an impacting particle to stick to the surface, m the mass of the particle, k_{B} the Boltzmann constant and T the temperature. This means, at room temperature N_2 would cover an entire surface, assuming 1×10^{15} surface atoms per cm^2 in a monolayer and $\alpha = 1$, in about a single second at a pressure of 1×10^{-6} mbar.[53]

Another important reason for working in UHV conditions is the inverse proportionality between the pressure and the inelastic mean free path, the distance a particle can translate before a collision with another particle occurs, which is on the order of nanometers at ambient conditions but of several kilometers in UHV. This becomes especially important in electron spectroscopy methods where electrons must overcome a significant distance from the sample to the detector.[53]

Maintaining constant UHV conditions requires all-metal sealed stainless steel chambers that are continuously pumped. In the publications of this thesis, mainly three vacuum systems at TUM were used, with the addition of beamline 9.3.2 at the Advanced Light Source (ALS) at the Lawrence Berkeley National Lab.[54] The majority

of the data shown in section 5.1 was acquired with a setup that includes a Scienta-Omicron *VT-AFM/STM*, an XPS with a SPECS *XR 50* X-ray source and an Omicron *EA 125* energy analyzer, a so-called Sniffer setup[55,56] for specialized TPDs, as well as a laser ablation cluster source[25] for producing size-selected metal clusters (referred to as VT-SPM setup from here on). This cluster source was complemented by the single-electrode Faraday cup, developed and built in this thesis, which is described in section 4.1. Detailed information about this UHV setup can be found elsewhere.[39,57,58] For LEIS and XPS measurements in the publication in section 5.3, another setup at TUM was used that contains a NAP-XPS with a *PHOIBOS 150* NAP hemispherical analyzer by SPECS and a monochromated X-ray source (*XR 50 MF* with *μFOCUS 600*, SPECS). The same analyzer and a scannable ion source (IQE 12, SPECS) were used for LEIS. Here, sample heating was achieved using a laser heater with a wavelength of 976 nm (OsTech DioSource).

In the following, the third, the NAP-STM setup with which the majority of experiments of sections 5.2 and 5.3 have been conducted is described. The chapter starts with elucidating this vacuum system, followed by sections outlining the experimental methods used in this thesis from both a theoretical and – in the case they belong to this setup – also a practical point of view.

2.1 Vacuum System

The vacuum system started as a commercial system by SPECS GmbH. Over the course of this doctorate, several components were added to enhance the functionality and enable additional measurement techniques. Figure 2.1 gives a schematic overview of the entire apparatus, showing the most important components. The system can be divided into two parts, the preparation chamber and the microscopy chamber, which are located on different frames, connected by only a bellow to prevent the propagation of vibrations. In the following, the relevant components of both of these chambers are described.

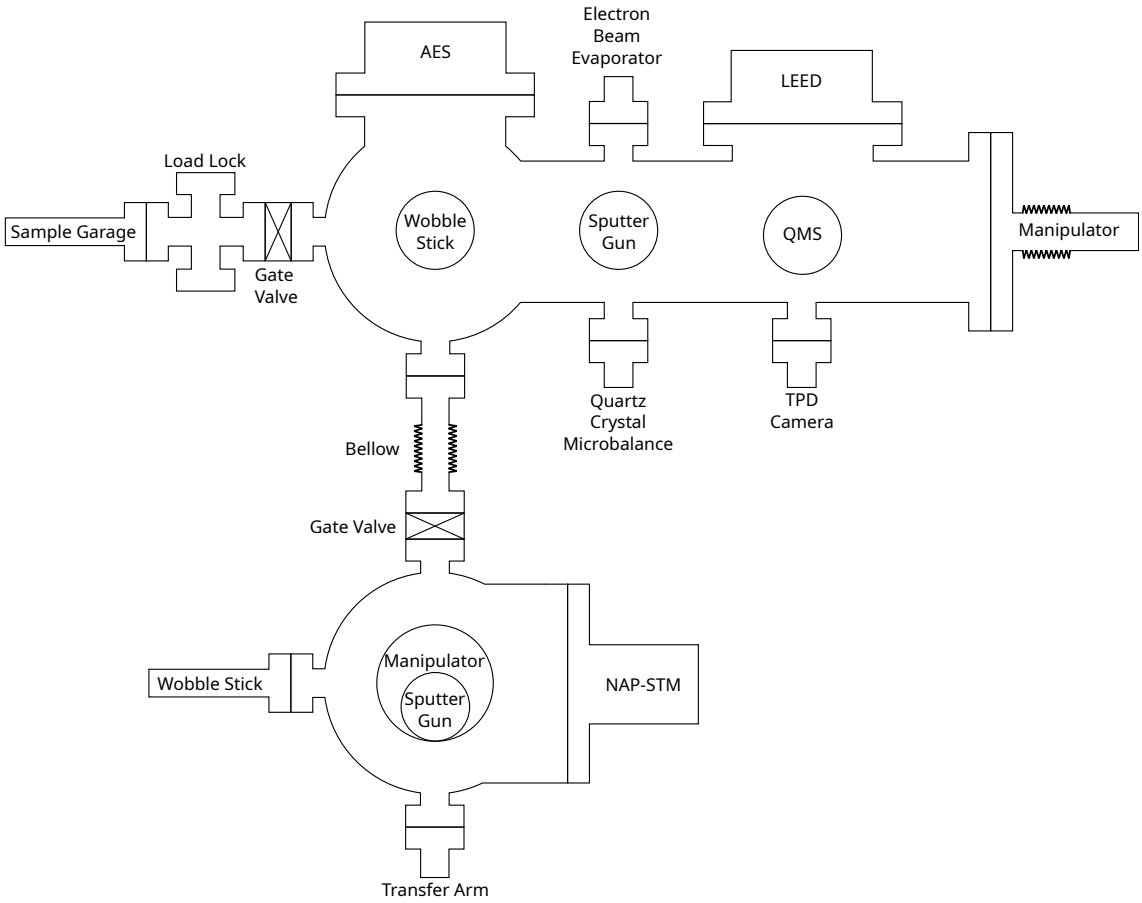

Figure 2.1: Schematic of the NAP-STM setup (not true to scale). Everything above the bellow belongs to the preparation chamber that houses, besides equipment for sample preparation, an Auger electron spectrometer and a low-energy electron diffraction device. Everything below to the bellow belongs to the microscopy chamber, which accommodates the NAP-STM.

2.1.1 Preparation Chamber

As the name suggests, the preparation chamber is used to conduct sample preparation, although additional measurement instruments can be found here. It is pumped by a turbo molecular pump (*HiPace 300*, Pfeiffer Vacuum), backed by a scroll pump (*Scrollvac 7 Plus*, Leybold), and a titanium sublimation pump (Gamma Vacuum) to achieve a base pressure of $p < 2 \times 10^{-10}$ mbar. The main parts needed for sample cleaning are a 4-axes (x, y, z, θ) manipulator, equipped with an elec-

tron beam heater, as well as a sputter gun (*IQE 11*, SPECS). The manipulator also enables the movement of the sample according to the needed lateral positions as well as the correct working distance for the additional experimental methods Auger Electron Spectroscopy (AES), Low Energy Electron Diffraction (LEED) and Temperature Programmed Desorption/Reaction (TPD/TPR), which are further described in sections 2.4, 2.5 and 2.6, respectively.

For metal atom deposition to form clusters or nanoparticles on a sample, an electron beam evaporator (*EBS-1*, SPECS) is used. To achieve a controlled coverage, the evaporation rate can be determined with a quartz crystal microbalance (OmniVac) which is mounted on the opposite side, orthogonal to the evaporator and can be brought into the same position as the sample via a linear transfer.

The introduction of samples into the UHV system is done via a small load lock, which is attached to the preparation chamber, separated by a gate valve and pumped by a turbo molecular pump (*HiPace 80*, Pfeiffer Vacuum), which therefore allows independent venting. A sample garage which can be moved through the gate valve into the preparation chamber is used for the efficient insertion of up to four samples simultaneously into the system. A wobble stick, mounted on an upwards-facing flange of the preparation chamber, is used to pick up a sample at a time and place it on the manipulator. This wobble stick is additionally used to transfer samples from the preparation into the microscopy chamber.

2.1.2 Microscopy Chamber

In the microscopy chamber, mainly one instrument can be found, the NAP-STM (*SPM Aarhus 150 NAP*, SPECS), which is further described in the next section (2.2). The reason why the STM is located in a separated chamber than all other devices is, on the one hand, as mentioned, the best possible vibrational insulation from other running devices and, on the other hand, to maintain clean conditions and have the best possible control over the gas atmospheres the samples are exposed to. Hence, the microscopy chamber is, besides a turbo molecular pump (*HiPace*

300, Pfeiffer Vacuum) and a TSP, additionally equipped with an ion pump. A transfer arm, reaching to the preparation chamber is used to transfer samples into the microscopy chamber. Here, they can be picked up by a wobble stick and either put into a sample garage (not shown in Figure 2.1) or directly into the STM.

As the NAP-STM does not allow for a tip exchange in situ, a sputter gun is located above the STM tip, mounted on a one-axis manipulator to adjust the working distance for ion bombardment.

2.1.3 Gas Distribution System

As the NAP-STM can operate at elevated pressures by filling a small cell with gas, a system that allows for dosing of contamination-free gases and gas mixtures is crucial. Also the preparation of sample crystals requires gases like argon for sputtering or oxygen to maintain the stoichiometry of oxide substrates. Finally, TPD is reliant on precise dosing of gases. Therefore, the experimental system has a gas distribution system that fulfills all these needs and is shown in Figure 2.2. The initial system that was installed by SPECS as part of the commercial setup [Figure 2.2 (a)] and only served the NAP-STM was extended by several parts, of which some are depicted in Figure 2.2 (b). The entirety of the system illustrated schematically in Figure 2.2 (c), can be pumped via a roots pump, which was added to the system, for pressures up to 10^{-3} mbar and a pumping station, including a turbomolecular pump and a membrane pump for lower pressures.

Two stationary gas cylinders with pressure regulators for argon and oxygen were added to deliver gas to the sputter guns of the preparation chamber and microscopy chamber as well as a leak valve at the latter chamber, respectively. All leak valves at the preparation chamber were modified with stepper motors which allows their opening and closing over their full range via software and thus a fully automated sample preparation. Furthermore, a panel was added that allows for the connection of additional minican gas bottles as well as vials for liquids with sufficient vapor pressure for dosing into the preparation chamber. For gas dosage

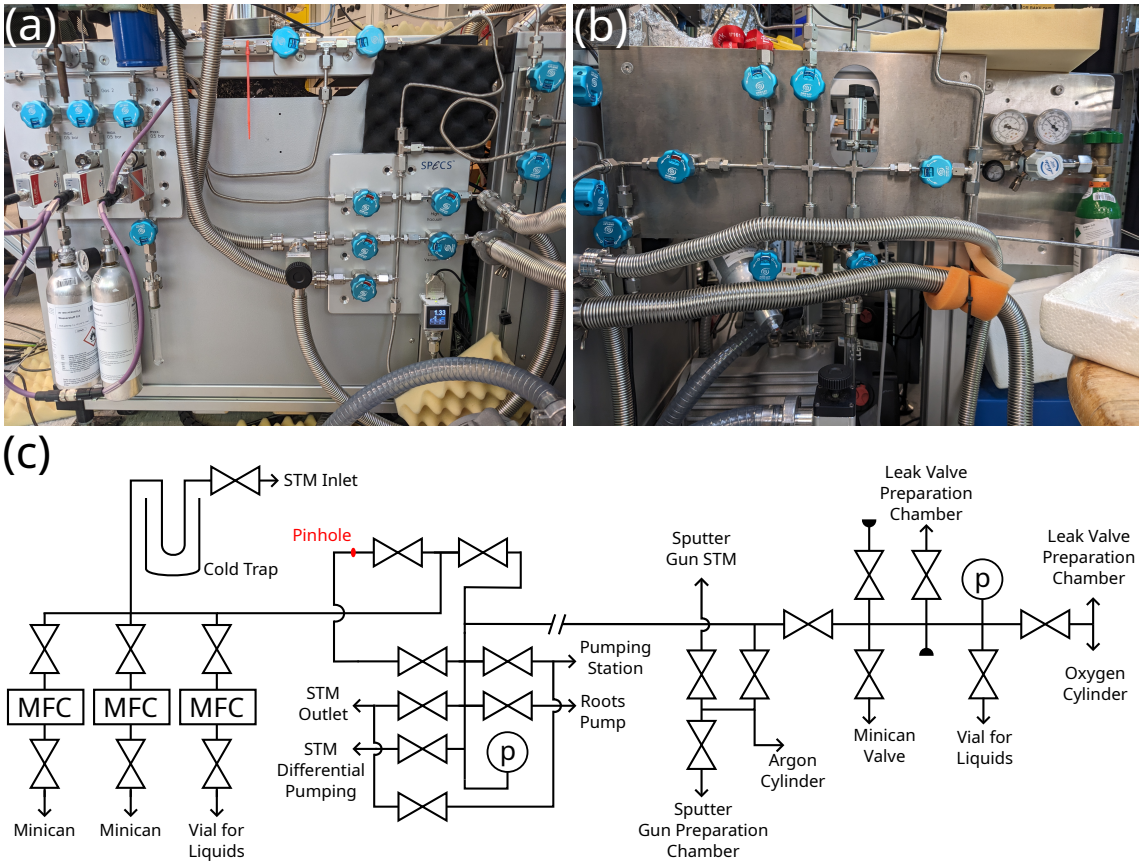

Figure 2.2: Photos (a), (b) and schematic (c) of the gas distribution system that, after additions and modifications, serves both the preparation and microscopy chamber and enables the NAP-STM measurements under a gas flow.

into the NAP-STM, a cold trap was added to remove water traces from hydrogen. All connections for the NAP-STM have additional mass flow controllers (MFC), which give control over gas mixture ratios. For operating the NAP-STM in a static gas atmosphere, the tubes above the mass flow controllers (MFC) can be simply filled with gas, which is then dosed via a leak valve. The more advanced operation under a gas flow requires a sufficient pressure gradient between the dosing (STM inlet) and the pumping side (STM outlet). The MFCs are used to maintain a constant pressure at the dosing side, of which a small fraction is leaked into the STM and a larger fraction is pumped by the roots pump via a pinhole [red mark in Figure 2.2 (c)]. Only the outlet of the STM is pumped via the pumping station. Here, the small diameter of the capillaries inside the STM is enough to

maintain a comparably high, quickly adjustable pressure. To facilitate this separated pumping, a bypass from the STM outlet to the turbomolecular pump was added in collaboration with SPECS.

2.2 Scanning Tunneling Microscopy

Scanning tunneling microscopy (STM) was invented by Binnig and Rohrer in 1981, who were awarded with the Nobel Prize in 1986.[59,60] Using piezoelectric actuators, a very sharp metal tip – ideally with an apex consisting of a single atom – can be positioned with sub-Ångström precision above the sample. If this tip-sample-distance d is small enough and an external bias voltage V_b is applied on the sample with respect to the tip, electron tunneling between tip and sample atoms can occur, giving rise to a tunneling current I_t. According to a one-dimensional approximation, the relation

$$I_\mathrm{t} \propto \mathrm{e}^{-2\kappa d} \tag{2.2}$$

with

$$\kappa = \sqrt{\frac{2m}{\hbar}(eV_\mathrm{b} - E)} \tag{2.3}$$

where m is the mass of an electron, $\hbar$ the reduced Planck constant, e the elementary charge and E the energy of the state from which tunneling occurs, shows the strong dependence of the tunneling current with the distance, i.e., bisecting the distance leads to an increase of the tunneling current by an order of magnitude.[53]

Figure 2.3 (a) shows a simplified schematic of an STM assembly. Rastering the sample with the tip in a grid while maintaining a constant tunneling current by immediate height adjustments controlled by a feedback loop results in an image of the electronic structure of the sample, which can be correlated to its topography. The bias voltage V_b causes the Fermi levels of tip and sample to be separated by

the energy eV, as depicted in Figure 2.3 (b). Within this energy, electrons can tunnel, horizontally in energy (illustrated by red arrows), from occupied states of the tip into unoccupied states of the sample ($+V_\mathrm{b}$), or vice versa, dependent on the sign of the bias voltage. This makes it evident that STM relies on samples that are conductive and have states close to the Fermi level.

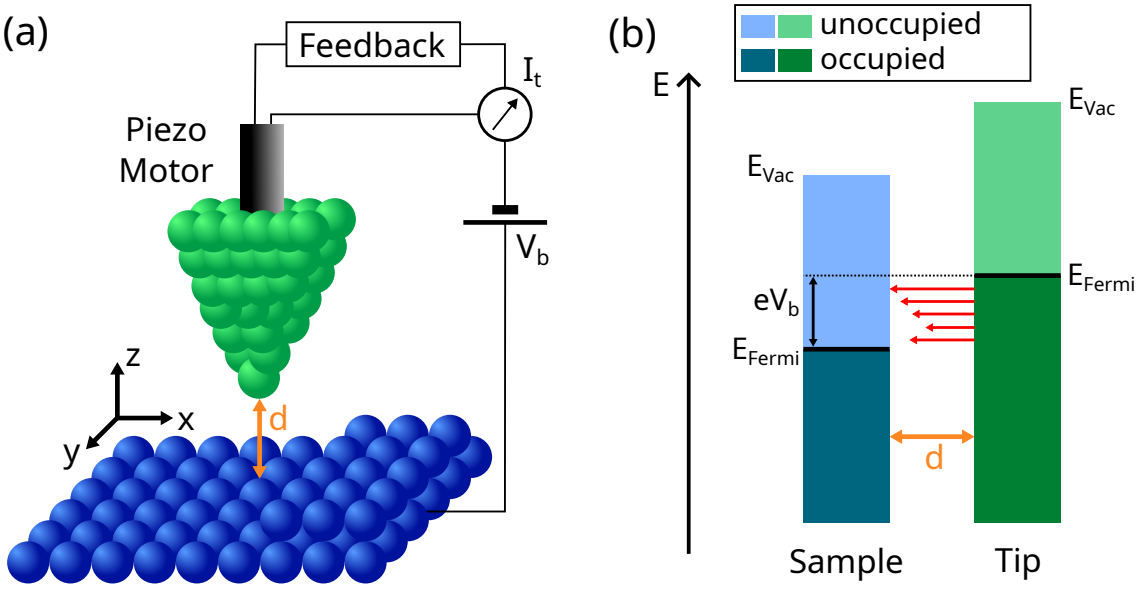

Figure 2.3: Working principle of scanning tunneling microscopy. (a) A sharp metal tip (green) is positioned close to the sample surface (blue) and a bias is applied between the two. The piezoelectric motor controls the precise movement of the tip in all three directions (x, y, z), while a feedback loop maintains a constant tunneling current by adjusting the tip height. (b) The applied bias voltage (V_b) separates the Fermi levels of the tip and sample by an energy of eV_b. Electrons can tunnel between the occupied states of the tip and the unoccupied states of the sample with different probabilities, depending on the density of states, which is illustrated by red arrows of varying lengths.

As STM is not limited to UHV and is fully functional in air, the desire to overcome the aforementioned pressure gap led to investigations in controlled gas atmospheres. The simplest approach is to backfill the vacuum chamber with gas which is limited to a pressure of 1 bar by the resilience of the chamber's viewports. More importantly, since the entire chamber is filled with gas the convective heat transfer becomes the biggest disadvantage as e.g., the scan head or the sample support are also heated when sample heating is performed, which results in in-

creased thermal drift. Additional downsides are that molecules can desorb from the chamber walls which leads to contamination in the gas phase as well as an increased safety risk when working with toxic gases because of the large volume. This lead to the development of special STM systems with a small cell where the gas is confined in.[61] Prominent examples of such systems are the ones developed in the groups of Somorjai[62] at the Lawrence Berkeley National Lab, Frenken[63] at Leiden University, Wintterlin[64] at LMU Munich and Besenbacher[65] at the University of Aarhus.

The latter is marketed commercially by SPECS GmbH under the name *SPM Aarhus 150 NAP* and used in the setup mentioned above. Its NAP-cell that is specified for pressures of up to 100 mbar, allows for fast switching between UHV and in situ operation by closing a lid with a wobble stick. With the filament being located on top of the lid, separated from the cell inside by a window and therefore in UHV but right behind the sample crystal, radiative heating at temperatures of up to 850 K in UHV and 550 K at 10 mbar can be achieved.[66] The sandwich design of the sample holder with its spring-loaded crystal mounting even allows for imaging during shallow heating ramps.[67]

We further improved the pressure readout sensitivity of the NAP-STM by relocating the full-range gauge from the outlet of the NAP-cell to the inlet and by installing two additional Baratron capacitance manometers at both the inlet and outlet. The former simplifies gas dosing in low pressure ranges, as the gas has to pass capillaries to and from the NAP-cell which can significantly delay the readout. The latter enables a more precise pressure readout in the range of $10^{-2} - 100$ mbar, independent of the gas type.

2.3 X-ray Photoelectron Spectroscopy

Its high surface sensitivity, as well as its provision of chemical information makes XPS commonly used in the field of surface science. Einstein laid the foundation for this technique with his explanation of the photoelectric effect[68] which was

awarded with the Nobel prize in 1921. Under irradiation, an atom can absorb a photon with the energy $h\nu$, with h being Planck's constant and ν the radiation's frequency. If, after absorption, the energy of the core level electron with binding energy E_{bind} is high enough to overcome the work function Φ, (the energy needed to remove an electron from the solid beyond the vacuum level), this electron gets ejected into the vacuum with the kinetic energy

$$E_{\mathrm{kin}} = h\nu - E_{\mathrm{bind}} - \Phi, \tag{2.4}$$

according to a single particle picture.[69] Before the detector counts the number of photoelectrons, an analyzer is used to separate them by kinetic energy. It is common to plot E_{bind} in a reversed scale, calculated with equation (2.4), instead of E_{kin} for the resulting spectrum. As the core level binding energies are element specific, they give direct qualitative information about the elemental composition of the irradiated sample surface. Similar to nuclear magnetic resonance spectroscopy, chemical shifts can be obtained in XPS. These are caused by a more efficient screening of the nuclear charge for negative oxidation states or a less efficient screening for positive oxidation states, respectively. Therefore, XPS can also give information about the chemical environment of the atoms.[70]

The high surface sensitivity of XPS originates in the short inelastic mean free path (IMFP) of electrons in solids which follows a general trend depending on the kinetic energy of the electron. As the trend of the IMFP is rather independent of the material, this results in a universal curve.[71] In the range between 15 and 1000 eV, the values for the IMFP are limited to less than 1-2 nm. Hence, only a few atomic layers are probed.[69]

As XPS is widely used in investigations to obtain chemical information about samples, very soon the desire to make it work in elevated pressures higher than UHV rose. However, the two parts of an XPS that must be kept at UHV are the electron analyzer as well as the X-ray source. First solutions to overcome the above mentioned decrease of the IMFP of the photoelectrons utilized differentially pumped stages between the sample surface and the unmodified electrostatic lens system of the electron analyzer, separated by small apertures.[72–76] At the synchrotrons ALS

and BESSY II, this design was further improved by additional lenses inside the differential pumping stages which focus the electrons onto the apertures, leading to an increased sensitivity.[72,77–79] Today, also the commercially available, lab-based systems from SPECS and Scienta-Omicron are based on this design.

Several different XPS systems were used for the publications contained in this thesis. All XPS measurements in the publication in section 5.1 used the UHV-XPS in the VT-SPM setup mentioned above. The same system as well as the NAP-XPS system were used in section 5.3. Section 5.2 exclusively contains XPS data measured at beamline 9.3.2 at the ALS.

2.4 Auger Electron Spectroscopy

As mentioned in section 2.3 it is possible to remove a core level electron by photoexcitation which results in an ionized state caused by the creation of a core level hole. Extending the former single particle picture, results in another electron, either from another core or valence level, to fill this hole.[53] Since the filling electron originates from a higher energy level, the difference in energy can either be released by the emission of a photon or it can lead to the ejection of another electron from the same or an even higher energy level. The former is called X-ray fluorescence while the latter process is an Auger transition, which was first described by Pierre Auger in 1925.[80] The resulting kinetic energy of the ejected electron only depends on the involved energy levels and is independent of the primary excitation energy. The initial hole creation can not only be caused by irradiation with X-rays but also by bombardment with ions or – as mainly used in application – with electrons [red in Figure 2.4 (a)].[69]

An example for the full mechanism is depicted in Figure 2.4 (a). First, an incoming electron (red) knocks out a core electron from the K level which creates a hole. This causes an electron from the L_1 level to fill the hole (orange) and simultaneously an electron from the L_2 level is ejected in the vacuum (green). This ejected

electron is called Auger electron, the entire process according to the energy levels involved KL_1L_2 Auger transition.[53]

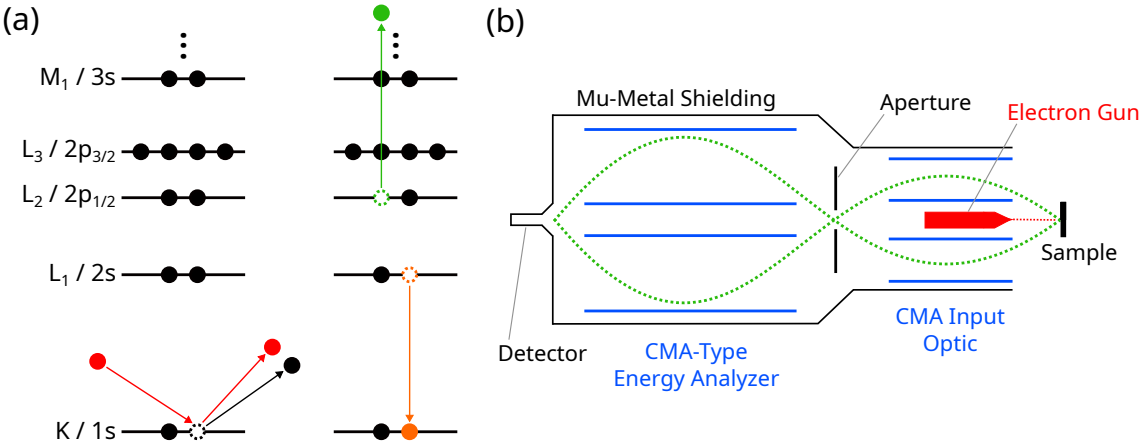

Figure 2.4: Working principle of Auger electron spectroscopy. (a) In the Auger process, an incoming electron (red) removes a core level electron, resulting in a hole on that energy level (left side). An electron from a higher level fills that hole (orange) and concurrently another Auger electron gets ejected (green) in the vacuum (right side). (b) Schematic of the Auger electron spectrometer. Electrons of certain kinetic energy get generated in the electron gun (red) and accelerated orthogonally onto the sample. The resulting Auger electrons get selected by their kinetic when guided through both CMA elements and subsequently detected by the detector.

All AES spectra in the following publications were acquired with a *Double-Pass DESA 100 Energy Analyzer* by STAIB Instruments GmbH, using a primary electron energy of 5 keV. A simplified schematic of the cross section of this instrument, which uses a double pass cylindrical mirror analyzer (CMA), is shown in Figure 2.4 (a). Each of the two CMA elements (blue) consists of inner and an outer cylindrical electrode, between which an electric field is applied. Electrons produced by the electron gun (red) which is located in the middle of the device are shot orthogonal onto the sample, typically with an energy of 3–5 keV. The Auger electrons then have to pass both CMA elements as well as an aperture in the middle of the two (green, dashed line). With variation of the strength of the electric field between the inner and outer cylinders, the passing electrons can be selected according to their kinetic energy. Therefore, only electrons of a certain energy can reach the

channeltron detector which enhances the signal.[81,82] Typical channeltron voltages of 1500 - 1600 eV were chosen to prevent detector saturation.

2.5 Low Energy Electron Diffraction

Another highly surface sensitive experimental method which gives information about the structure is low energy electron diffraction (LEED). Here, an electron beam with defined kinetic energy E_{kin} is shot orthogonally onto the sample surface whereby electrons get scattered elastically. Treating the electrons as a wave with the de Broglie wavelength

$$\lambda = \frac{h}{\sqrt{2 m_{\mathrm{e}} E_{\mathrm{kin}}}}, \tag{2.5}$$

with h being Planck's constant and m_{e} being the mass of an electron, and utilizing electrons with an energy of $\sim$30-200 eV results in a wavelength of $\sim$1-2 Å, which is on the order of interatomic distances and thus satisfies the diffraction condition. Analogous to XPS, the low kinetic energy of the electrons and the thus resulting short IMFP is the reason for the high surface sensitivity of LEED.[69,82] Generalizing the Bragg condition to two dimensions leads to the Laue conditions

$$a_1(s - s_0) = h_1 \lambda \tag{2.6}$$

$$a_2(s - s_0) = h_2 \lambda, \tag{2.7}$$

with the lattice constants a_1 and a_2; s_0 and s are the directions of the incident beam which generally is orthogonal to the surface and the direction of the diffracted beam intensity maxima, respectively. The integers h_1 and h_2 identify the diffraction reflexes with $h_1 = h_2 = 0$ being the specular reflex that is elastically scattered without diffraction.[53]

A schematic of a LEED setup is illustrated in Figure 2.5 (a). An electron gun produces monoenergetic electrons that are accelerated onto the sample due to a negative voltage applied to the electron gun's cathode. After the scattering of

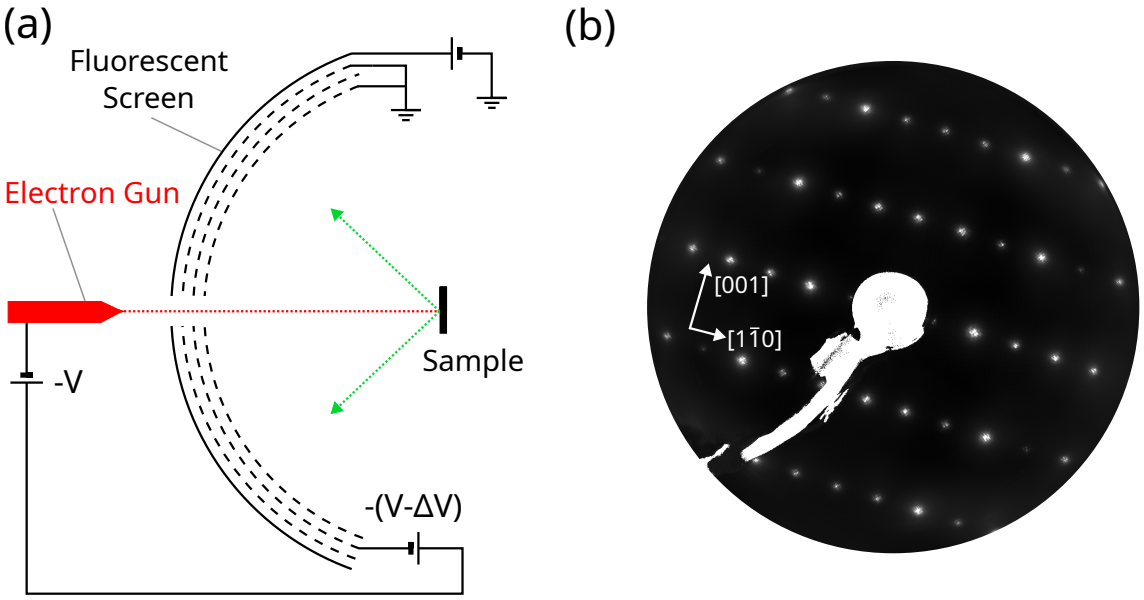

Figure 2.5: (a) Schematic of a LEED instrument. Electrons generated by an electron gun (red) get accelerated orthogonally onto the sample surface, where they get diffracted. After energy filtering by a retarding field, they get detected with a fluorescent screen. (b) LEED pattern of $TiO_2(110)$ rutile, as it is shown on the fluorescent screen.

the electrons on the sample surface, they move through three grids, of which the middle one is on a potential close to the one of the cathode of the electron gun but slightly offset by ΔV, which causes the inelastically scattered electrons to be rejected. Thus, increasing ΔV causes a brighter LEED pattern at the cost of an increased background. After filtering, the remaining electrons get reaccelerated due to a positive potential (~ 5 keV) of the fluorescent screen to achieve sufficient brightness. The two outer grids are on ground and shield the field caused by the potential on the middle grid and the fluorescent screen to maintain a field-free space, preventing deviations of the electrons' trajectory.[82] Figure 2.5 (b) shows a resulting LEED image of $TiO_2(110)$ with an energy of 200 eV of the primary electrons. From this image, it becomes evident that the resulting pattern reflects the periodicity of surface atoms in reciprocal space. The distances in the $[001]$ direction (along the 5-fold coordinated Ti) are larger compared to the $[1\bar{1}0]$ direction, which is the reverse of what is observed in the actual crystal structure.

All following LEED data was acquired with a *ErLEED 150* by SPECS that is part of the NAP-STM setup.

2.6 Temperature Programmed Desorption / Reaction

Another technique that can give information about the ad- and desorption, as well as reaction mechanisms of gases on the sample surface is temperature programmed desorption (TPD) or temperature programmed reaction (TPR), respectively. Here, a sample is, usually at low temperatures, exposed to a gas atmosphere at a certain pressure for a specific time length. Subsequently, the sample is heated in front of a quadrupole mass spectrometer (QMS) with a heating rate β in the range of $0.1 - 25\ \mathrm{K/s}$. In the QMS the desorbents/products are ionized and detected depending on their mass-to-charge ratio (m/z). The rate of desorption r, which is defined as the change of adsorbate coverage θ over time t, can be determined by

$$r = -\frac{d\theta}{dt} = k_{\mathrm{des}}\theta^n = \nu(\theta)\theta^n e^{-\frac{E_{\mathrm{des}}(\theta)}{RT}} \tag{2.8}$$

with

$$T = T_0 + \beta t, \tag{2.9}$$

and the reaction rate constant for desorption k_{des}, the order of desorption n, the pre-exponential factor of desorption ν, the activation energy of desorption E_{des}, the gas constant R as well as the starting temperature T_0.[69] From TPD data, information about the binding strength, adsorption sites, desorption/reaction order and saturation coverage can be obtained.

All TPD data was measured using the Sniffer of the VT-SPM setup.

2.7 Low Energy Ion Scattering

Another extremely surface sensitive technique that is especially useful in the field of catalysis is low energy ion scattering. Here, the sample is bombarded by a beam of noble gas ions, typically He^+ or Ne^+, of which a fraction is scattered at the surface upon which they lose energy. The resulting kinetic energy after scattering therefore depends on the mass of the ions, the mass of the surface atom with which scattering occurs and the initial kinetic energy of the ions which is typically in the range of 0.1–10 keV. Similar to measuring the kinetic energy of photoelectrons in XPS, the scattered ions get counted depending on their energy. In fact, the same analyzer used in XPS can also be used for LEIS if the polarity is switched such that positively charged ions can be analyzed rather than electrons. The reason LEIS is still very surface sensitive, even with ion energies of 10 keV, is that ions, which are scattered in the first surface layer and can enter the solid have a very high probability of neutralization, e.g., 99 % for He^+ ions which penetrate through a single layer and, as mentioned above, an electrostatic analyzer is used which only detects ions and not neutrals. Depending on the energy and mass of the noble gas ions that are used, the substrate surface can be additionally sputtered, i.e., the bombarding ions can release surface ions out of the lattice. Hence, care must be taken not to change the sample surface to be analyzed by sputtering, but on the other hand, this effect can be utilized to achieve depth profiling of the sample.[69]

The LEIS data shown in section 5.3 was acquired in the above mentioned NAP-XPS setup.

3

Custom Software for Data Management and Analysis

To analyze STM data effectively, a reliable and versatile tool is essential. For this purpose, *Gwyddion*, a prevalent, open-source software designed for scanning probe microscopy (SPM) data analysis was used. Its functionality includes essential tasks such as image correction, noise filtering, and image export.[83] However, primarily to enhance convenience in the image analysis, additional software packages as well as several custom extensions within *Gwyddion* were developed. These tools were specifically tailored to work with the data that is produced at the NAP-STM setup on a daily basis, addressing limitations in existing solutions. However, as other scientists might have similar needs, all of them provide open source access on Github under `https://github.com/matkrin` where all contributions are welcome, be it in the form of issue reports, pull requests, or other.

gwy-z-module

The custom *Gwyddion* extensions in *gwy-z-module*[84] were developed using *Gwyddion's* module system that is accessible through a C-based application programming interface (API). The file format used by the NAP-STM can contain up to 64 images, which can lead to a lack of a high-level overview when only small, unprocessed thumbnails are visible, like in *Gwyddion's* data browser. Therefore, the functionality to apply the *Plane Level* function to all images at the same time was implemented. Furthermore, an alternative data browser for single files and entire folders with larger image previews was developed.

proespm-py3

To further optimize a high-level overview of measurement data, the software *proespm*[85] was rewritten from scratch in Python 3 with several enhancements, such as a graphical user interface (GUI). Furthermore, functions for image correction were implemented in Python, which allowed for the removal of all *Gwyddion* bindings. This, however, made it necessary to handle parsing of different proprietary file formats in Python, which led to the development and publication of the following libraries to the Python Packaging Index (PyPI): *mulfile* for .mul files (NAP-STM), *sm4file* for .sm4/.SM4 files (RHK SPM 100) and *vamas* for .vms files (several spectroscopy techniques). With its core functionality of creating interactive, shareable HTML reports from scientific data, including basic processing like SPM image corrections, the resulting *proespm-py3*[86] establishes a data management structure on the file server to simplify access to stored raw data.

quickplot

Another program that is based on the same idea is the created tool *quickplot*[87], which can create similar reports, however on-the-fly as it comes in the form of a web application, deployed via *github pages* and available under `https://matkrin.github.io/quickplot`, therefore allowing ultimate accessibility. There is no communication of data to a server as all functionality is implemented client-side in TypeScript with performance-intensive tasks, like image plane subtraction, in Rust compiled to WebAssembly. However, this tool was developed especially for the NAP-STM setup and therefore does not offer the same versatility as *proespm-py3*, only supporting the .mul file format used by the NAP-STM, .vms files created by the AES, mentioned in section 2.4 as well as log-files produced by the SPECS software *Prodigy* were all parameters such as temperature and pressure are logged during measurements. All AES data, which can be smoothed via a Savitzky-Goley[88] filter and normalized with respect to each other over a selected range, are plotted together, which enables fast and reliable comparison.

xps-peaks

The software *xps-peaks*[89] is a web application that provides a fast and interactive search for the positions of XPS peaks for one or more chemical elements and is available at `https://matkrin.github.io/xps-peaks`. All expected signals are visualized in a zoomable plot as well as a table. Furthermore, it allows for choosing the excitation energy of the X-rays, which enables a fast identification if photoelectron peaks might overlap with Auger peaks, making it an ideal helper tool for the planning of synchrotron measurements.

spm-rs

The last created program, which was explicitly designed as a helper tool for usage during STM measurements, is *spm-rs*[90] that is fully written in Rust. This, at this point, highly experimental software provides an image browser that contains the images of all .mul files inside a chosen folder. The images are automatically corrected with subtraction of a fitted plane and a line-by-line mean subtraction. Choosing one image opens a resizable window with a detailed view of it where the image contrast can be adjusted by creating a rectangle whose contents maximum and minimum height are used to readjust the color map, thus enabling fast identification of surface features. Additionally, after one image is saved in the NAP-STM control software, it is automatically added to the image browser as the chosen folder is watched for changes in another thread.

4

Development of two Faraday Cups for Cluster Beam Detection

As mentioned in the introduction, small metal clusters enable access to the non-scalable size regime. Hence, their size selection is a crucial factor to be able to investigate unique properties as a function of number of atoms they contain. Thorough characterization of cluster beams inside and at the exit of cluster sources is therefore of high significance for the availability of well-defined samples. As the clusters generated in our sources are always charged particles, Faraday cups are suitable tools for this kind of analysis. Thus, two new Faraday cups were designed and constructed. The first one is used in a laser ablation cluster source[25], where the Faraday cup enables concurrent sample preparation or surface characterization and cluster beam characterization together with fine-tuning of parameters. The second Faraday cup will be part of a new magnetron sputter cluster source[26], which is a facility of the e-conversion Cluster of Excellence of the German Research Foundation (DFG) and can be used in future studies using, for example, the NAP-STM as well as a new NAP-XPS setup.

A Faraday cup is essentially a metal device designed to capture ions or electrons in a vacuum. By measuring and quantifying the charge of these particles, it becomes possible to determine the number of ions or electrons striking the cup. The principle behind the Faraday cup is that electromagnetic fields vanish inside conductive materials, which also holds true for those with cavities. This phenomenon is observable even in perforated metal surfaces or cages, a concept commonly known as a Faraday cage. The field-free interior of the cup ensures that the particles

are measured without any interference, allowing for precise detection even in the picoampere range.[91]

Figure 4.1 illustrates the basic design of a Faraday cup. When charged particles enter the cup and transfer their charge to its walls, electrons must flow either into or out of the cup to maintain a constant potential at the detector. This electron flow is detected by measuring the voltage drop across a high-ohmic resistor through which the electrons move. According to Ohm's law, a high resistance is required to measure low currents, such as those in the picoampere range. Given that the charge of a singly charged particle is approximately 1.6×10^{-19} C, a measured current of 1 nA corresponds to the detection of billions of singly charged ions per second hitting the Faraday cup.

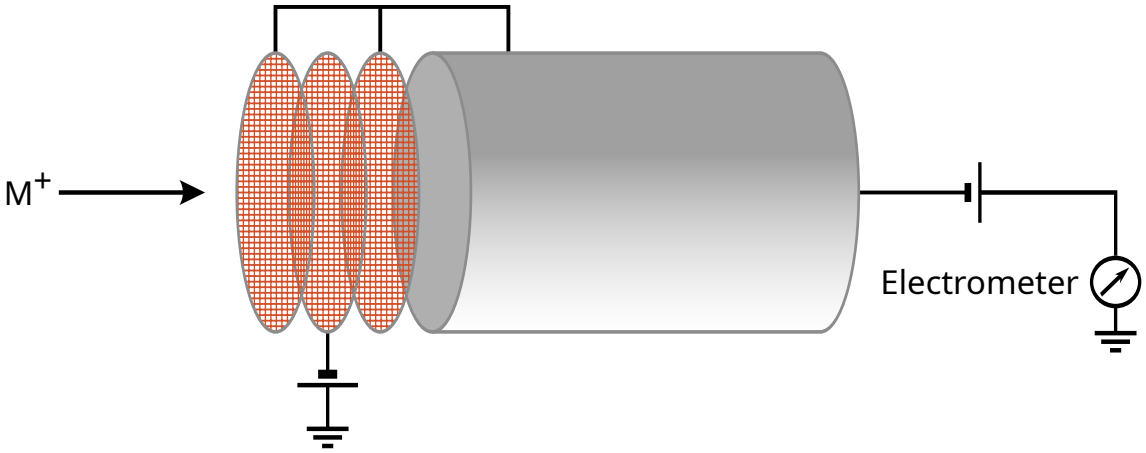

Figure 4.1: Working principle of the designed Faraday cups. Metal ions (M^+) enter the Faraday cup by passing three copper grids. The middle grid can be used to apply a retarding field which is shielded due to the outer grids, which are on the same potential as the Faraday cup. Upon contact with the walls of the cup, cations get neutralized by electrons, resulting in a current that is measured by an electrometer.

To prevent the leakage of reflected ions, electrons, or re-emitted secondary electrons, a negatively charged suppressor electrode, in our case in the form of a highly transmissive copper grid, is placed at the entrance of the cup. However, the potential applied to the grid induces an electric field that affects the charged particles as they approach the cup as well as inside the cup, potentially causing distorted

measurements. To prevent this, we designed both new Faraday cups with three copper grids, as depicted in Figure 4.1. By placing the retarding voltage grid between two additional grids that are on the same potential as the cup, this field is effectively shielded, a configuration that is also commonly used in low-energy electron diffraction (LEED) instruments.

Thus, our design enables the Faraday cups to measure both beam intensity, i.e., how many particles arrive per time unit, as well as kinetic energy of arriving particles by variation of the retarding potential, which is crucial to determine the resulting coverage and to guarantee soft landing conditions (typically $0.1 - 1$ eV per atom), respectively.[92,93]

The aforementioned cluster sources always yield charged particles by selecting the sign of the charge using a quadrupole deflector. As these clusters pass through the electric field, they are deflected based on their mass-to-charge ratio, while neutral clusters remain unaffected.[25,26]

4.1 Single-Electrode Faraday Cup

The first Faraday cup was built for the cluster source of the VT-SPM setup, mentioned in chapter 2. It was installed on a sandwich flange with a CF-16 at the end of a tube that is orthogonal to the beam direction, between two lens stacks, after the quadrupole mass filter, and before the bellow that connects the cluster source with the preparation chamber. Hence, the inner diameter of the tube demanded a compact design. Figure 4.2 shows computer-aided design (CAD) drawings of this Faraday cup, with its cuboid format and a total size of $27\ \text{mm} \times 13\ \text{mm} \times 5\ \text{mm}$ (height $\times$ width $\times$ depth).

The only part that needs to be machined is the mount that holds all parts together, gets fastened on the linear transfer and resembles three of the six cuboid sides. The detector electrode, the inner shield, the retarding electrode as well as the outer shield/case were constructed from Ta foil with a thickness of $0.1\ \text{mm}$. Figure 4.2

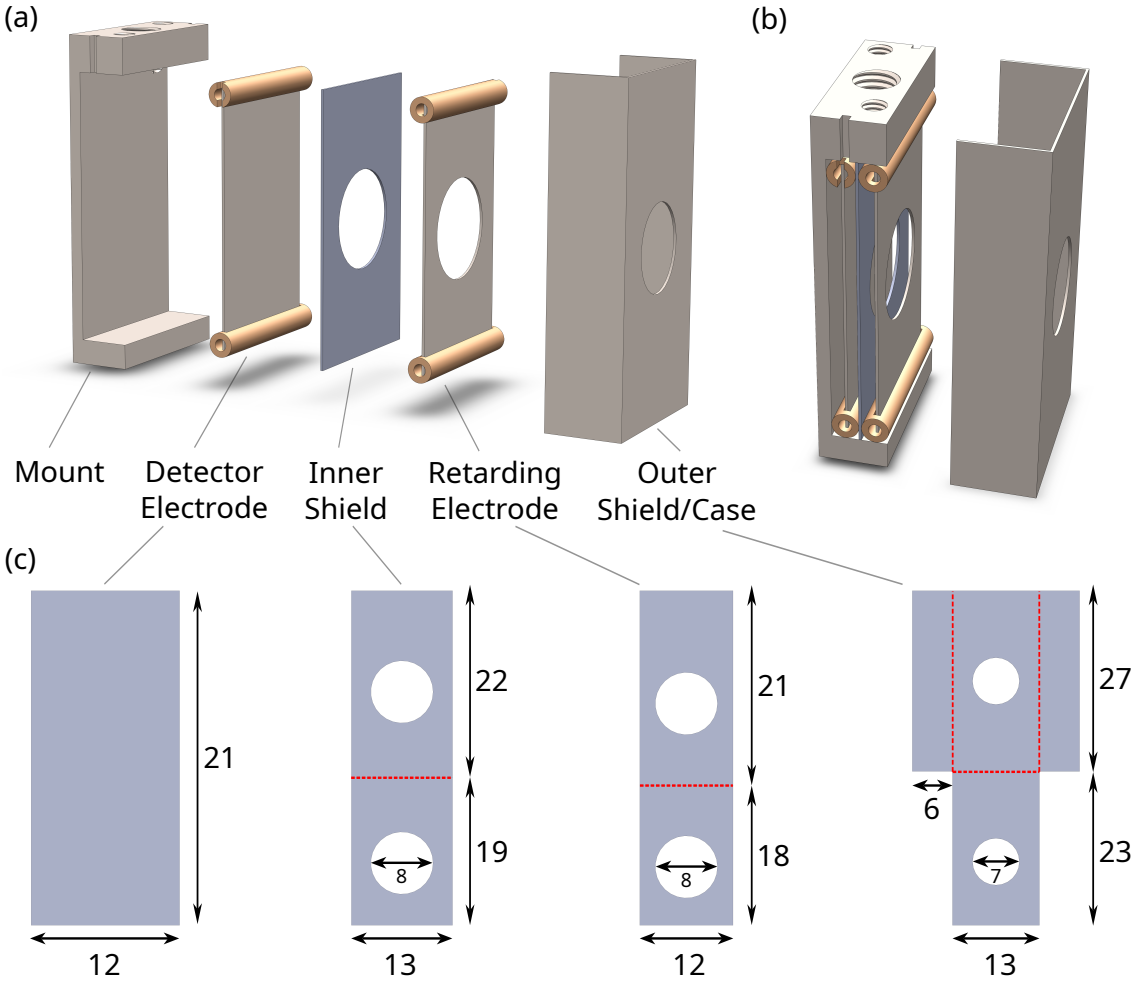

Figure 4.2: Computer-assisted design (CAD) drawings of the single-electrode Faraday cup. (a) Fully exploded view, (b) Assembled with the cover removed, (c) Layouts of the detector electrode, inner shield, retarding electrode and outer shield/case. The parts in (c) were cut out of a Ta foil with $0.1\ \mathrm{mm}$ thickness, folded along the dotted red lines, hole-punched and spot-welded together with copper grids between the folded halves. All size specifications in mm.

(c) shows the layouts of these parts as they were cut from the foil. Subsequently, they were folded along the dotted red lines and hole punched with a punching iron. After unfolding, a highly transmissive copper grid (Solid Surface Laboratory, 8 line/mm, 88–92 % Transmission) was placed between the two halves that were then folded back and spot-welded together. For the outer shield/cover, the smaller sides were additionally folded by just $90\,\mathrm{deg}$, resulting in the remaining three sides

of the final cuboid. Single-hole ceramic tubes ($d_{\text{outer}} = 2\ \text{mm}, d_{\text{inner}} = 1\ \text{mm}$) were slit on one side with a small angle grinder, covering the ends of the detector and the retarding electrode. Afterward, insulated copper cables were spot-welded on the two electrodes and guided through small slits at the end of the ceramic tubes as well as the top side of the mount. Thus, these two electrodes are insulated from the rest of the Faraday cup, allowing a precise, field-free measurement as well as applying a voltage to create a retarding field simultaneously. Figure 4.2 (b) shows how the individual electrodes are located in the mount, kept in place, and separated from each other by the ceramic tubes. Finally, the outer shield is imposed on the mount and spot-welded in place.

Figure 4.3: Photos of the single-electrode Faraday cup. (a) Top view of the full assembly with the Faraday cup mounted at the end of a linear transfer that is connected to a four-way CF-16 cross together with two BNC feedthroughs. (b) Magnified view of the Faraday cup. (c) + (d) Backside of the Faraday cup inside the cluster source taken from the preparation chamber through a lens stack with the position of the linear transfer at (c) $62\ \text{mm}$ and (d) $75\ \text{mm}$.

The top view of the final assembly is then screwed on the linear transfer, as can be seen in Figure 4.3 (a) and (b), thus the outer shell as well as the inner shield are ultimately grounded via chamber walls. The cables are guided along the rod of the linear transfer, through the four-way cross and connected to the BNC feedthroughs via cable crimps. Note that enough cable length needs to be provided to guarantee

a sufficiently large travel of the linear transfer, as its inner rod is moving against the four-way cross.

Ideally, the entrance hole of the Faraday cup is centered concentrically with respect to the lens stack in front of it. To ensure this during the installation without having to disassemble parts of the cluster source, a light was shone through the chamber of the cluster source, directing from the bender to the preparation chamber. At the latter end, the position was checked with a magnifying camera. Figure 4.3 (c) shows the lower end of the Faraday cup vertically centered with respect to the lens stack, corresponding to a position of the linear transfer of $62\ \mathrm{mm}$. By adding $13\ \mathrm{mm}$ which is the distance from the lower edge to the center, an optimal position for measurements of $75\ \mathrm{mm}$ [Figure 4.3 (d)] was obtained.

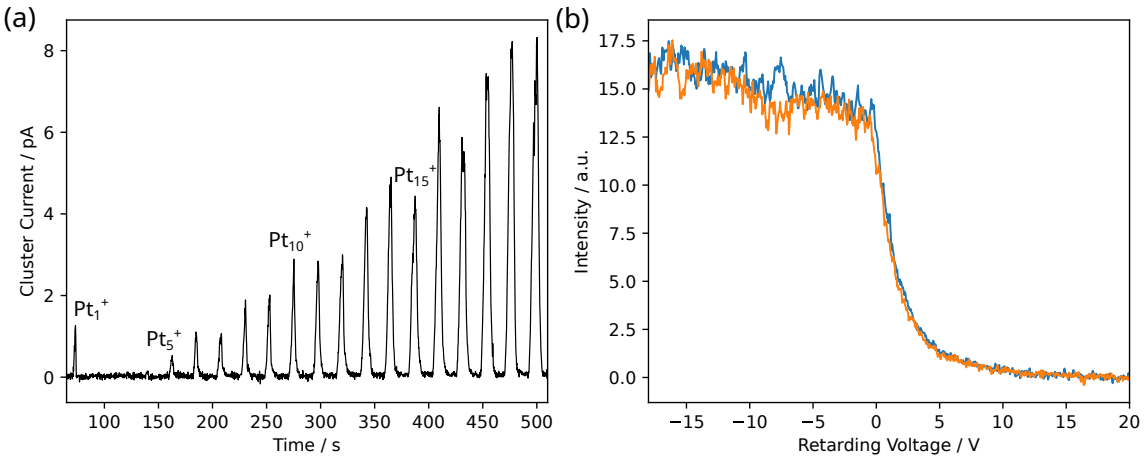

Figure 4.4: (a) Mass scan from Pt_1^+ to Pt_{20}^+ (50 ms/data point) and (b) and potential sweeps for Pt_{20}^+ from -18 to 20 V with increasing (blue) and decreasing (orange) potential measured with the singe-electrode Faraday cup (20 ms/data point, 20 data points/V, 10 sweeps each averaged).

Figure 4.4 (a) depicts a mass scan from Pt_1^+ to Pt_{20}^+ using the new single-electrode Faraday cup, showing a high signal-to-noise ratio for cluster sizes larger than Pt_4^+ with a noise level in the fA range and clearly separated peaks. The potential sweeps in Figure 4.4 (b) clearly illustrate that the determination of the kinetic energy, using a retarding potential applied to the middle grid, is also possible. Hence, upgrading the laser ablation cluster source with this Faraday cup enhances sample

throughput as the decisive parameters can now be determined during measurements or sample preparation.

4.2 Five-Electrode Faraday Cup

As the five-electrode Faraday cup is part of a cluster generation setup that is a shared facility associated with the DFG excellence cluster e-conversion, and therefore, the type of samples is very diverse, a versatile design is required. Considering this, the following design decisions were made. Firstly, the measurement position of the Faraday cup should be located at the same position as a sample on which clusters get deposited. Thereby, the cluster beam characteristics can be determined and optimized with the Faraday cup before the deposition as a simultaneous recording of, e.g., the cluster current requires special sample holders with an insulated sample. Secondly, as the sizes of samples can vary, a special design with five electrodes was chosen to provide the best possible local resolution and the possibility to characterize the beam profile.

To fulfill the former requirement, a linear transfer with a travel of 150 mm and a port aligner are part of the full assembly as it is depicted in Figure 4.5 (a). These two parts are connected to a four-way CF-40 cross at which two BNC feedthroughs, each with four connections, are mounted. A CF-40 blind flange with drill holes for the framework that holds the Faraday cup is connected to the last flange of the CF-40 cross. The framework consists of three threaded rods that are connected by two additional spacer discs to improve stability due to increased rigidity.

For the latter requirement, the diameter of the inner electrode was chosen to be 3 mm, which is less than the surface of the smallest single crystal used by the associated groups of e-conversion. The diameter of the inner combined with the four outer electrodes is 13 mm which corresponds roughly to the biggest possible sample size that is mountable on flag-style sample holders that are used in the setup's deposition chamber. To obtain the position of the maximum in cluster current and, therefore, the most time-efficient deposition, the Faraday cup is movable

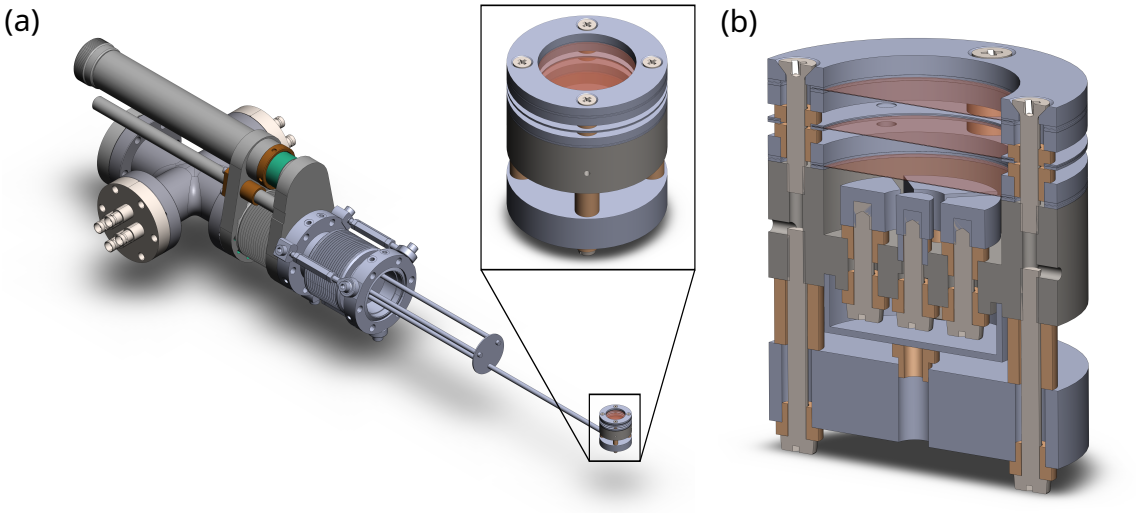

Figure 4.5: CAD drawings of the five-electrode Faraday cup. (a) Full assembly consisting of four-way CF-40 cross, linear transfer, port aligner, two BNC feedthroughs with 4 connections each, blind flange with threaded rods that hold the Faraday cup (inset) at the other end. (b) Cut view of the Faraday cup with the main parts from bottom to top: the base plate where the threaded rod is connected, casing with the five electrodes inside (darker gray), stack of three copper grids. Ceramic parts are illustrated in brown.

inside the chamber via the linear transfer and the port aligner. Combining this mobility with the fact that its five electrodes can be read out independently from each other allows for a characterization of the beam profile, up to a resolution in the single-digit millimeter range.

As mentioned, two BNC feedthroughs with four connections each are used, which gives a total of eight separate electrical connections. Five of these connections are used for the measuring electrodes, one for the case that surrounds the electrodes as well as the outer and inner grid, and one for the inner grid that is used for the creation of a retarding field for kinetic energy determination. Hence, in contrast to the single-electrode Faraday cup, this design allows having the shielding part on a different potential than common ground, e.g., the potential of the last focusing lens of the mass-separating part of the cluster generation setup. In fact, the only part that is always grounded is the base plate that is connected to the long threaded rod of the framework. For all electrical connections, kapton insulated coaxial cables were used, of which the core was exposed and, in the

case of the electrodes and the shielding case, soldered onto the screw heads on which the electrodes are mounted and the backside of the case, respectively. The screw heads are additionally shielded by a small metal cap. For the retarding grid, which was – like all grids – assembled by spot welding together two thin metal discs with the grid placed between, the insulated core of the cable [the separated one in Figure 4.6 (a) and (b)] is guided through a small drill hole at the side of the shielding case, as can be seen in Figure 4.6 (a) and the exposed core additionally spot-welded between the discs.

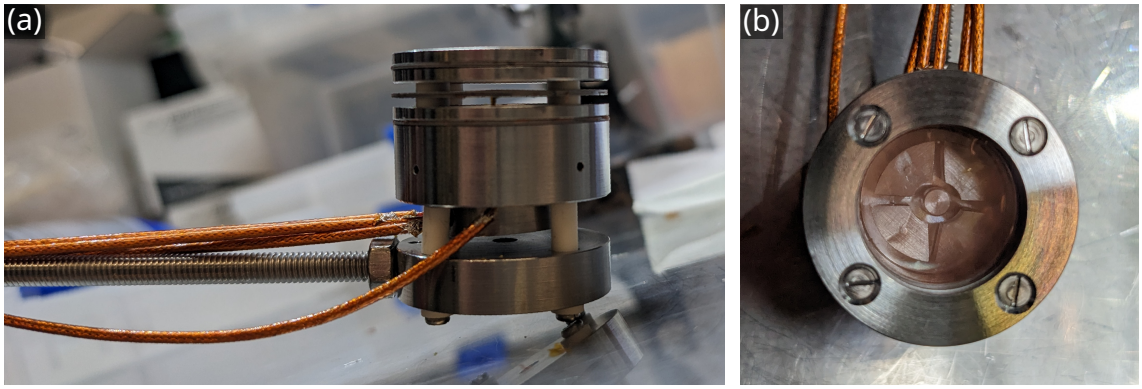

Figure 4.6: Photos of the five-electrode Faraday cup. (a) Side view showing the base plate mounted at the long threaded rod of the framework and the separated cable passed through the front-facing side of the shielding case. The end of the cable can be seen at the lower gap between the grids. (b) Top view illustrating the five electrodes underneath the copper grids.

Since the new cluster source does not produce clusters yet, the Faraday cup could not be tested but it is anticipated to help in the generation of samples with size-selected, supported clusters, which will enable new studies in our near-ambient pressure setups.

5 Publications

5.1 On-Surface Carbon Nitride Growth from Polymerization of 2,5,8-Triazido-*s*-heptazine

Title: On-Surface Carbon Nitride Growth from Polymerization of 2,5,8-Triazido-*s*-heptazine

Authors: Matthias Krinninger, Nicolas Bock, Sebastian Kaiser, Johanna Reich, Tobias Bruhm, Felix Haag, Francesco Allegretti, Ueli Heiz, Klaus Köhler, Barbara A. J. Lechner and Friedrich Esch

Journal: Chemistry of Materials **2023**, *35*, 6762–6770.

Status: Published August 23, 2023

DOI: 10.1021/acs.chemmater.3c01030

Contributions

This investigation was a key project of mine over many years, where I coordinated several different experiments in various labs. My contributions as part of my doctoral thesis are experiments under UHV, the analysis and visualization of the experimental data, and the writing of the publication. This project started already in my Master studies, where I synthesized and characterized the carbon nitride

precursor molecule 2,5,8-Triazido-*s*-heptazine (TAH) during a research internship in the group of Klaus Köhler under the supervision of Tobias Bruhm. Section S2 of the supporting information summarizes these results and is therefore not part of this doctoral thesis. There are additional results from my Master's thesis and Nicolas Bock's doctoral thesis,[85] who was my supervisor at that time, that overlap with the content of this publication: The results on the TAH evaporation process (section S3, supporting information), some of the TPD data shown in Figure 3 as well as the STM images shown in Figure 4 can be found in both former theses. The STM measurements in air and the corresponding XPS experiments shown in Figure 5 are also part of my Master's thesis. The inset STM image in Figure 2 (b) can be found in Nicolas Bock's thesis. Felix Haag and Francesco Allegretti provided the XPS instrument for the measurement shown in Figure 5 (b), as well as preliminary XPS results, which are not contained in the publication. All other XPS, as well as UHV-STM measurements, were performed with Sebastian Kaiser and Johanna Reich. Ueli Heiz was involved in the funding acquisition and discussions. Barbara A. J. Lechner and Friedrich Esch also provided funding, supervision, took part in discussions, and were involved in the writing process.

Content

In this publication, we investigate a carbon-based model catalyst support. Specifically, we demonstrate the polymerization of TAH on Au(111) and HOPG surfaces following different reaction pathways. The reaction and the resulting 2D carbon nitride were investigated with STM, XPS and TPD. The synthesis of TAH followed established procedures, starting from melamine.[94,95] Prerequisite for the polymerization is a successful deposition. We showed that intact TAH can be evaporated at a temperature just below the onset of the reaction. The three different reaction pathways we investigated take place (i) via X-ray illumination and the resulting emission of secondary electrons, (ii) via UV light illumination and subsequent annealing of the stable intermediate and (iii) via merely thermal activation. All three pathways result in an amorphous, not fully closed, but mainly homogeneous 2D

film, as shown in STM images and corresponding line profiles. Its stoichiometry, obtained by XPS, indicates a mixture of different linking motifs. Furthermore, the deposited TAH and the final film show a high stability against ambient conditions as we obtain a flat film after UV induced reaction in low vacuum, even after exposing the sample to air after the deposition step. Additionally, we draw the comparison to HOPG, where a purely thermal reaction is not possible due to weaker bound TAH. However, a lower amount of secondary electrons induced by XPS enables following the decomposition during illumination. Subsequent annealing results in a seemingly loosely bound network as STM tip-induced displacement occurs in subsequent images.

CHEMISTRY OF MATERIALS

pubs.acs.org/cm
Article

On-Surface Carbon Nitride Growth from Polymerization of 2,5,8-Triazido-*s*-heptazine

Matthias Krinninger, Nicolas Bock, Sebastian Kaiser, Johanna Reich, Tobias Bruhm, Felix Haag, Francesco Allegretti, Ueli Heiz, Klaus Köhler, Barbara A. J. Lechner, and Friedrich Esch*

Cite This: *Chem. Mater.* 2023, 35, 6762–6770

ABSTRACT: Carbon nitrides have recently come into focus for photo- and thermal catalysis, both as support materials for metal nanoparticles as well as photocatalysts themselves. While many approaches for the synthesis of three-dimensional carbon nitride materials are available, only top-down approaches by exfoliation of powders lead to thin-film flakes of this inherently two-dimensional material. Here, we describe an in situ on-surface synthesis of monolayer 2D carbon nitride films as a first step toward precise combination with other 2D materials. Starting with a single monomer precursor, we show that 2,5,8-triazido-*s*-heptazine can be evaporated intact, deposited on a single crystalline Au(111) or graphite support, and activated via azide decomposition and subsequent coupling to form a covalent polyheptazine network. We demonstrate that the activation can occur in three pathways, via electrons (X-ray illumination), via photons (UV illumination), and thermally. Our work paves the way to coat materials with extended carbon nitride networks that are, as we show, stable under ambient conditions.

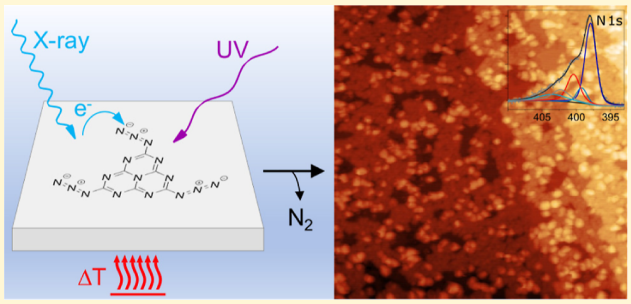

INTRODUCTION

The long-established carbon nitrides, consisting of the earth-abundant elements carbon and nitrogen, have recently moved into the focus of research for their potential as (photo)catalysts in water splitting or carbon dioxide photoreduction.[1−3] The term carbon nitride generally describes polymers consisting predominantly of C and N species. More specifically, (graphitic) carbon nitrides (g-C_3N_4) are categorized as 1D or 2D networks based on the *s*-triazine and *s*-heptazine building blocks, in line with Lau and Lotsch.[4] Networks consisting of heptazine building blocks can be connected via tertiary amine links, forming true g-C_3N_4 sheets where nitrogen atoms provide a coordination environment in the pores. Alternatively, connection via secondary amines leads to the formation of hydrogen-containing chains (melon) or cyclic arrangements in 2D poly(heptazine imides). Beyond the ideal structure of g-C_3N_4, defective modifications have been designed to tune the electronic properties.[4−6]

Besides their direct application for metal-free catalysis,[5,7] the porous nanostructures provide binding sites for catalytically active metal ions or particles. The coordination of metals to the nitrogen atoms of the carbon nitride pores is flexible enough to provide access for reactants while also immobilizing the active sites efficiently against dissolution and sintering. As the group of Ramirez showed, Suzuki coupling can be sustainably performed even on single Pd ions that remain coordinated in the carbon nitride pores throughout the involved redox process.[8] Furthermore, the addition of metal and metal oxide cocatalysts into the pores has been shown to overcome sluggish charge transfer kinetics in the photo-(electro)catalytic water splitting by carbon nitrides.[4] More generally, the ability to bind catalyst particles from single atoms to entire clusters in an ordered manner[9] could provide a platform to systematically access size effects in the catalysis on small clusters at the non-scalable limit.[10,11]

Synthesis of purely 2D-linked, hydrogen-free g-C_3N_4 networks is experimentally highly challenging.[4] Starting from a variety of precursors,[12] the thermal condensation of melamine typically leads to the formation of only 1D melon chains, while a guided synthesis mediated by salt melts or on crystalline salt surfaces induces the 2D order via formation of poly(heptazine imides) without terminating primary amines.[4,13] A variety of more complex approaches have been reported toward a 2D preparation of g-C_3N_4, namely laser-electric discharge methods,[14] chemical vapor deposition,[15] electrodeposition,[16] spray deposition,[17] liquid−gas interface separation,[18] and exfoliation.[19] Furthermore, in an alternative

Received: May 2, 2023
Revised: July 14, 2023
Published: August 23, 2023

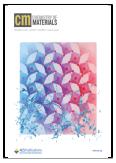

https://doi.org/10.1021/acs.chemmater.3c01030
Chem. Mater. 2023, 35, 6762−6770

synthetic approach, Gillan and later the Kroke groups demonstrated that extended networks can be formed starting from single triazine or heptazine azide precursors.[20−24] Here, via thermal activation, without the need for a catalyst, powders of carbon nitride networks form. This route proceeds in the solid state via the intermediate formation of a highly reactive nitrene species; upon reaction, the sp^2 ring character is maintained. The authors showed that the final hydrogen content and thus the degree of interlinking strongly depend on pressure conditions, humidity, exposure time, and especially on heating rate upon thermal activation. This autocatalytic one-pot reaction is highly exothermic and occurs in a temperature range where the background slope of the thermogravimetric analysis might be interpreted as the onset of evaporation. The various products that can be envisaged are summarized in Supporting Information Figure S1—from primary, secondary, and tertiary amines to azo coupling, introducing hydrogen to the reactive nitrene sites of the network that is picked up from the ambient environment. Interestingly, the authors discuss only amine linking as the final connection motif.

The challenge now is to bring the polymerization reactions known for powders of carbon nitride networks onto a highly defined 2D support in order to obtain single-layer carbon nitrides as controllable interfaces. Since the formation of single atomic layers is still hardly accessible with current methods,[25] we chose the catalyst-free Gillan approach as the most promising one for the translation of a powder to an on-surface synthesis. In this work, we present an azide-based polymerization route on two highly defined, atomically flat materials, i.e., Au(111) and highly oriented pyrolytic graphite (HOPG), that have the potential to be used as model electrodes for more applied future studies. As the single precursor, we opted for the hydrogen-free 2,5,8-triazido-*s*-heptazine (TAH, see Figure S1) where three $-N_3$ azide groups can react both thermally[21,22] and light-induced[26,27] and, as we will show, also induced by electrons. For similar azides, a tradeoff between volatility and reactivity has been demonstrated to allow intact sublimation and deposition,[28,29] maintaining the azide reactivity, for example, for a "click" reaction.[28] The TAH precursor forms layered, close-packed crystals that indicate the feasibility of coplanar adsorption and flat 2D coupling on the surface.[21] The decomposition, under the formation of gaseous nitrogen as the only byproduct, leads to the formation of planar, rigid building blocks with directional, active nitrene linkers and therefore represents one of three reaction stimuli discussed to prepare ordered covalent organic frameworks (COFs, via the "single reaction pathway" in ref 30).

We base the discussion of our results on two recent ultrahigh vacuum (UHV) studies on on-surface reactions of similarly functionalized molecules: A first study on the thermally induced reactivity of single azide-functionalized phenanthrenes by highly resolving, cryogenic non-contact atomic force microscopy could discern three different reaction channels on Ag(111). Starting from a postulated silver-nitrenoid intermediate, the authors observed either the nitrene insertion into a C−H bond, its dimerization, or hydrogenation.[29] In comparison, our choice of the TAH precursor is free of hydrogen, allowing us to exclude the C−H insertion pathway, which would lead to heptazine ring modifications, and thus we expect linking predominantly via azo bonds. In a second, rare example of surface-bound azide photochemistry, Luo et al. postulate a mechanism for 4-methoxyphenyl azide on Cu(100) that proceeds via an upright arylnitrene-intermediate where the reactive nitrene is stabilized by a bond to the support before coupling among the molecules to form a planar azoarene.[31]

In this paper, we focus on the various non-catalytic methods to activate the TAH azide groups, namely thermally, by photons, and by electrons, and characterize the resulting films with a particular view on density, flatness, homogeneity, and composition. Furthermore, we show the stability of the resulting film in air, thus presenting a universal approach to anchoring catalytically active particles in highly controlled interfaces of porous carbon nitride networks on supports or in 2D-layered heterostructures.[32,33]

EXPERIMENTAL SECTION

The carbon nitride precursor TAH was synthesized from melamine over melem and 2,5,8-trihydrazino-*s*-heptazine.[23,34] Au(111) single-crystal samples were prepared by several cycles of sputtering (Ar^+, 4×10^{-5} mbar, 2.0 keV, 15 min) and subsequent annealing (900 K, 10 min). For heating, a boron nitride heater located in the sample holder was used. The temperature was measured via a thermocouple (type K) attached to the crystal. For scanning tunneling microscopy (STM) measurements in air, we used Au(111) laminated on mica samples (Georg Albert PVD-Beschichtungen) which were flame-annealed in a hydrogen flame for several seconds. Evaporation of TAH was performed with a home-built molecular evaporator consisting of a small tantalum crucible spot-welded on to a wire connected to an electrical feedthrough. Additionally, a thermocouple (type K) was spot-welded to the crucible and was heated via resistive heating. STM measurements in ultrahigh vacuum (UHV, $p_{bg} < 1 \times 10^{-10}$ mbar) were performed with an Omicron VT-SPM in constant current mode with electrochemically etched tungsten tips at room temperature (RT). STM in air was performed with an STM built by the Wandelt group,[35] equipped with the SPM 100 control electronics by RHK. Here, tips were cut from a Pt/Ir wire (80/20, Temper hard, $d = 0.25$ mm, $R = 6.81\ \Omega\ m^{-1}$). For temperature-programmed reaction (TPR) measurements, a so-called sniffer was used. A detailed description of this device can be found elsewhere.[36] In short, desorption and reaction products are guided through a quartz tube, which is in close vicinity to the sample surface (∼100−200 μm), to a differentially pumped quadrupole mass spectrometer (QMS, Pfeiffer Vacuum GmbH, QMA 200 Prisma Plus). X-ray photoelectron spectroscopy measurements were performed with the Al Kα-line of a SPECS XR 50 X-ray source and an Omicron EA 125 energy analyzer.

RESULTS AND DISCUSSION

A prerequisite for the clean preparation of polyheptazine films from an azide precursor is the feasibility of physical vapor deposition of the pure precursor, which was synthesized from melamine over melem and 2,5,8-trihydrazino-*s*-heptazine,[23,34] as described in the Supporting Information, Section S2; precursor purity and reactivity agree with the literature.[22] Hereby, two effects have to be balanced: While the high reactivity of the TAH azide functional groups calls for the lowest possible evaporation temperature, considerable intermolecular interactions within the TAH packing, due to the C/N alternation and charge distribution, imply rather high evaporation temperatures. We thus first had to determine whether we could evaporate the molecule intact or already activated. To this purpose, a few milligrams of the substance were heated in high vacuum ($p_{bg} < 5 \times 10^{-8}$ mbar) with the crucible placed in front of a QMS while monitoring the mass scan. As seen in Figure S3, a distinct peak of intact TAH (C_6N_{16}, $m/z = 296$) can be detected around 470 K, as well as several fragment signals in the range between $m/z = 52$ and $m/z = 132$, most likely originating from fragmentation in the QMS. We assign the fragment $m/z = 78$ to *s*-triazine (C_3N_3),

https://doi.org/10.1021/acs.chemmater.3c01030
Chem. Mater. 2023, 35, 6762−6770

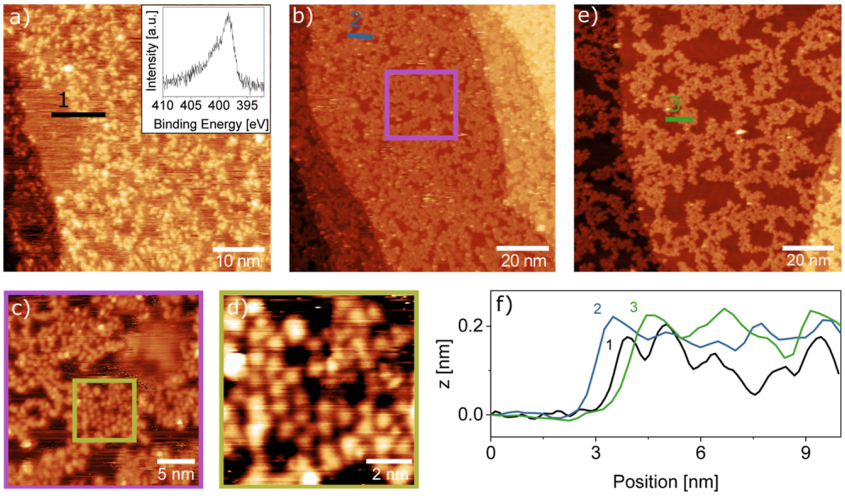

Figure 1. STM images of the on-surface synthesis of 2D carbon nitride via X-ray-induced electron activation at RT. (a) TAH molecules evaporated onto Au(111) and subsequently illuminated by an X-ray source form a disordered network of molecules which covers most of the surface, with some streaky patches of mobile species. The inset shows an XPS measurement of the N 1s region, demonstrating that the azides have already been fully reacted. (b) Annealing the same surface to 573 K leads to a less corrugated film and fewer streaks. (c,d) Zooming into the network reveals small areas of ordered molecules, which appear to remain intact upon polymerization. (e) A final annealing step to 673 K followed by further X-ray illumination opens up larger holes in the film. (f) Height profiles across the films in (a), (b), and (e) show that the overall height is similar in all three cases, corresponding to a monolayer. STM imaging parameters: U_b = 1.5 V, (a–d) I_t = 300 pA, (e) I_t = 10 pA.

which has a comparatively strong intensity due to its stabilizing π-system. Further signals are present throughout the entire temperature range and arise from residual gases in the vacuum chamber, i.e., H_2O (m/z = 18), CO (m/z = 28), and CO_2 (m/z = 44). In the entire measurement range from m/z = 1 to 600, we only observe signals from the monomer, its fragments, and residual gases.

Distinct spikes in the fragment signals around the TAH desorption maximum hint at possible molecule ejection caused by autocatalytic microexplosions at slightly hotter spots inside the crucible-located powder. Since both, the decomposition of TAH upon evaporation and the fragmentation of the evaporated TAH in the QMS, contribute to the atomic N signal (m/z = 14), we discriminate between the two by overlaying the TAH signal onto its initial rise: The polymerization reaction thus sets in at the temperature where the nitrogen curve starts to deviate from the TAH curve (indicated by a vertical dashed line in the right panel of Figure S3). We therefore deduce the ideal evaporation temperature range to be just below 445 K.

In the next step, we dosed TAH onto a clean Au(111) surface and investigated three different pathways toward on-surface polymerization: (i) via X-ray illumination (and thus secondary electron excitation), (ii) via UV illumination, and (iii) thermally.

Electron-Induced Polymerization (via X-rays). We start with the polymerization induced by X-ray photons, as shown in Figure 1. The network resulting from X-ray illumination at room temperature shows a random arrangement of bright protrusions of around 0.2 nm height from immobilized molecules, which confine similarly high streaks resulting from species that are mobile under the STM tip (Figure 1a). The quality of the network can be improved and the streaks removed by heating it to 573 K. This temperature is sufficient to desorb unreacted monomers and to complete the azide activation while avoiding further decomposition of the carbon backbone (see thermogravimetric data of TAH powder)[22] and is therefore generally chosen for annealing. The resulting network (Figure 1b) appears more homogeneous in height (still 0.2 nm), as clearly seen in the height profiles in Figure 1f. We find that the network still covers the surface evenly, without a net preference for nucleation at steps. When zooming in successively from Figure 1b–d, we can resolve round features, which in some places form a quasi-hexagonal network. From the measured average distance of about 0.9 ± 0.1 nm, approximately matching the molecule distances when azo-bridged (0.8 nm for free-standing dimers), we assign these features to individual heptazine molecules. The increased hole size upon further heating to 673 K in Figure 1e suggests that the network contracts. Comparing height profiles shows that the corrugation within the polymer islands remains as flat as after the first annealing step.

To obtain further information on the chemical composition immediately after TAH deposition, we look at the N 1s X-ray photoelectron spectroscopy (XPS) spectrum taken right after starting the X-ray illumination (Figure 1a inset). As we will discuss in more detail below, this shape is characteristic of TAH molecules that have already lost their azide functional groups.[37] The same effect appears much slower on the less reactive HOPG surface, where we initially can record reference spectra of the intact precursor (a time-resolved XPS series on HOPG is shown in Section S4). The N 1s spectrum in Figure 1a shows that the azide reacts quasi-instantaneously upon exposure to X-rays, and only the heptazine core and the linking nitrogen species remain. This difference in reactivity suggests that secondary electrons generated in the support play a prominent role in X-ray activation.

When comparing the films that result after annealing under the STM, their different mobility is striking: under similar scanning conditions, the network on HOPG gets continuously displaced (see Figure S5), while the one on Au(111) is stable. This indicates a stronger interaction that could tentatively be assigned to a stronger charge transfer and coordination of the Au atoms with the heptazines' π-system and the central tertiary amine group, as well as to image charge interactions of the

https://doi.org/10.1021/acs.chemmater.3c01030
Chem. Mater. 2023, 35, 6762–6770

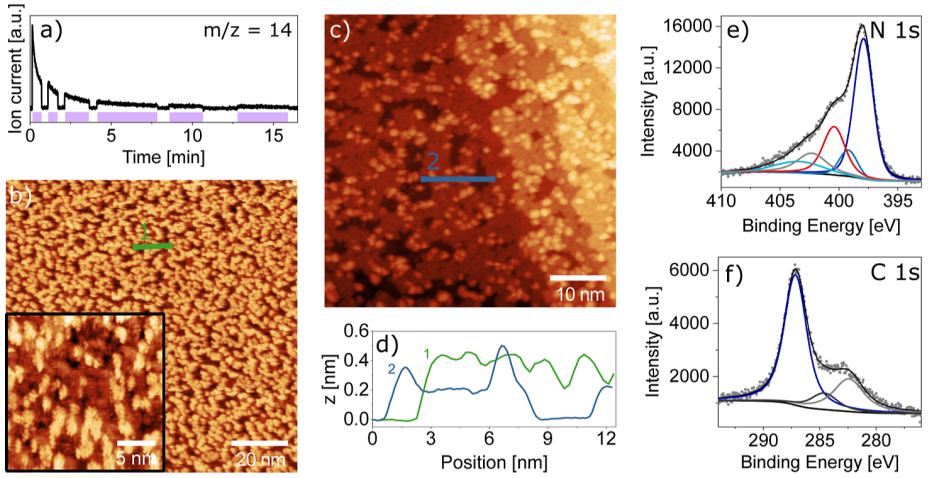

Figure 2. Room-temperature STM images and XPS data of 2D carbon nitride by photoinduced synthesis at 150 K. (a) The nitrogen (m/z = 14) mass trace demonstrates reproducible N_2 release concomitantly to illumination with 365 nm UV light of TAH deposited onto Au(111). The purple shading indicates when the sample was illuminated. (b) STM images of the illuminated surface show an amorphous arrangement of molecules. The zoomed-in region in the inset reveals a fern-like appearance of molecule assemblies, which we interpret as stacked, upright-standing molecules. (c) Annealing the same surface to 573 K leads to a flat, nearly complete monolayer with individual molecules in the second layer. (d) Height profiles of the images in (b,c) show that the fern-like structure appears of a similar height as the second-layer molecules. (e) XPS data in the N 1s region of the preparation shown in (c) reveal the unchanged heptazine unit, represented by the conjugated heptazine peak (dark blue), the central tertiary amine (blue), and a red peak at the position of linking amines and azo components (for the XPS analysis, see Section S5). Characteristic peaks of the azide groups are absent. In analogy to the literature, we assign the light-blue peak to π-excitation, while the gray peak is an unidentified component. (f) The corresponding C 1s peak contains components of heptazine (dark blue), adventitious carbon (black), and an unknown component (gray). STM imaging parameters: U_b = 1.5 V, I_t = 300 pA.

polar C−N bonds in the heterocycle with the highly polarizable Au support.

Photoinduced Polymerization (UV Light). Next, we look at the photoinduced synthesis by UV illumination with an LED at 365 nm, as shown in Figure 2. Turning the UV lamp on and off in front of a mass spectrometer shows the release of nitrogen only during illumination (Figure 2a). To avoid competing thermal reaction channels, we performed this activation at 150 K and found that the reaction proceeds with an exponentially decaying rate that becomes negligible after a total illumination time of 10 min. The resulting film shown in Figure 2b appears at first sight to be similarly holey to that in Figure 1. However, height profiles across the structures show a film thickness that is up to twice as high, and zooming in reveals fern-like details at different apparent heights. These parallel stripes at a distance of some Å appear as though heptazine molecules standing upright are stacked in vertical sheets. Such upright geometries have previously been reported on Cu(111) for nitrenoids[31] and for thermally activated melamine molecules,[38] while the sheet stacking recalls the layered 3D crystal structure (0.3 nm interlayer distance).[21] This interpretation would suggest that we do not have a fully polymerized film at this stage. While we found that the as-deposited molecules are bound too weakly for stable STM imaging, here we now have only a partially reacted precursor state that we can image successfully, most likely thanks to direct nitrene-gold bonds. Indeed, a subsequent annealing step to 573 K leads to a flat, nearly complete single-layer polymer with additional individual molecules or small agglomerates in the second layer. The height profile shown in Figure 2d shows almost no corrugation within the monolayer areas of this annealed film. The single flat layer shows an apparent height of 0.2 nm, similar to the values observed in Figure 1, while second-layer molecules have roughly twice the apparent height.

XPS measurements of the annealed film in the N 1s and C 1s regions indicate that the heptazine core remains unmodified by the polymerization reaction (blue peaks in Figure 2e,f), while an additional smaller peak at 400.4 eV (red peak) indicates amine and/or azo groups. These include bridging amine and azo linkers as well as chain-terminating primary amines. Note that the hydrogenation of nitrenoid compounds to amines most likely occurs by reaction with residual hydrogen and water. The precise assignment based on the literature (ref 37 and references therein) and the relative peak intensities are given in Section S5 (Table S3).

Thermal Polymerization. In order to better understand the chemical reaction occurring during the polymerization, we performed highly sensitive TPR measurements using our sniffer setup.[36,39] In the N_2 temperature-programmed desorption (TPD) spectrum, we observe four components. We discuss the N_2 TPD by comparing the overall N_2 formation (m/z = 28 trace) with molecular desorption (using the most intense accessible TAH fragment, m/z = 78). We use HOPG as a reference for intact desorption (Figure 3a). Here, we find that the m/z = 28 and 78 signals have precisely the same shape, implying that they arise from fragmentation of the intact, desorbed TAH molecule in the QMS. By overlaying the two traces, we determine a sensitivity multiplication factor of 3800. Notably, the onset of desorption just beyond room temperature implies that the interaction of TAH with the HOPG support is substantially weaker than within the bulk material.

Applying the same scaling factor to a sub-monolayer sample on Au(111), shown in Figure 3b, we observe that about 50% of the molecules desorb intact, while the remaining molecules react. To better illustrate the different components in the TPD curve, we show the difference spectra of the m/z = 28 and the scaled m/z = 78 signals in red in the right panels of Figure 3. The difference curve for sub-ML/Au(111) shows a reactivity maximum of around 450 K, which corresponds to the

https://doi.org/10.1021/acs.chemmater.3c01030
Chem. Mater. 2023, 35, 6762−6770

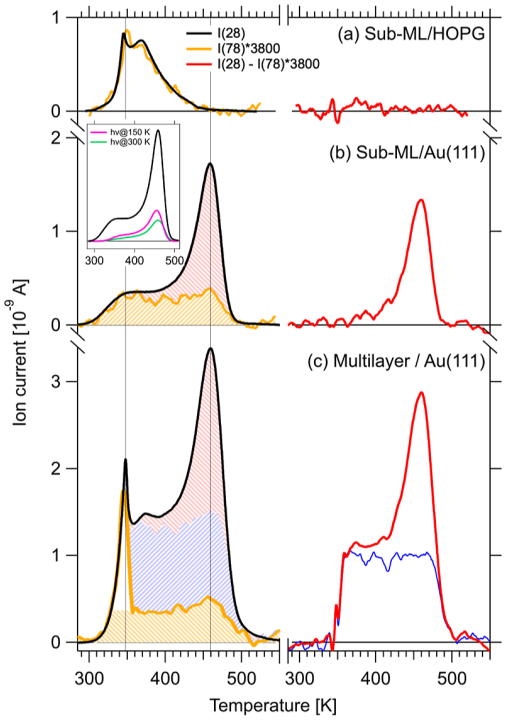

Figure 3. TPD measurements during thermal on-surface carbon nitride synthesis. For each experiment, the mass traces for TAH molecules (m/z = 78) and for N_2 from azide decomposition (m/z = 28) are shown in orange and black, respectively (left panels), and the difference between the two traces in red (right panels). (a) By studying the desorption from HOPG, where no reaction but only multi- and monolayer desorption takes place, we calibrate the intensity difference to be a factor of 3800, which we apply to the m/z = 78 traces on Au(111) in (b,c). (b) Desorption of a sub-ML coverage preparation on Au(111) shows two components: intact molecules desorbing in a broad peak between 300 and 500 K (orange) and reaction products from network formation around 450 K (red shaded area and difference trace). The inset compares the purely thermally treated sample with two that were previously illuminated for photoreaction at 150 (pink) and 300 K (green). Each spectrum starts from a similar TAH coverage. (c) At a higher TAH coverage, molecules desorb from multilayer sites around 350 K (white area in orange trace) and in the same broad peak again. Reaction products are now observed not only in the 450 K peak but an additional broad component also appears (the blue curve is a difference between the red curve in (c) and the red curve from (b) scaled by a factor of 1.4, resulting in the blue shaded area).

decomposition temperature of the pure powder precursor. In the m/z = 28 curve (left), we can thus distinguish two components: intact desorption (shaded in orange) and reacted precursors (shaded in red), respectively. Notably, the orange component has a tabletop-like shape corresponding to a wide range of activation energies of desorption, thus indicating a wide range of binding configurations (e.g., unspecific adsorption sites or varying intermolecular interactions). Once again, the molecular desorption from the surface starts well below the temperature observed for powders.

When increasing the dosed TAH coverage to a multilayer equivalent, two more components appear in the TPD (Figure 3c): A sharp peak at 350 K (white area in the orange trace) is observed in both traces with intensities that match the scaling factor determined on HOPG. Note that the same peak is also apparent in the HOPG trace. We tentatively assign this peak to weakly, van der Waals-bound molecules in a highly disordered multilayer. The remaining yellow contribution is likely comparable to that of the sub-monolayer preparation, i.e., the desorption of intact molecules. When subtracting both traces from each other, the same reaction peak at 450 K (red) is again observed, but with a slightly higher intensity and on a tabletop background. To shade the different components in the multilayer TPD trace, we further subtracted the red curve in Figure 3b, scaled by a factor of 1.4, from the red curve in Figure 3c and thus obtained the fourth component, i.e., the blue curve and the blue shaded area, respectively. The blue component shows a similar behavior as the yellow one and originates therefore most probably also from the desorption of intact molecules. The reason for the missing signature in the m/z = 78 trace remains unclear at this point.

From our TPD experiments, we conclude that the polymerization reaction can indeed be quantitatively confirmed for up to 50% of the deposited molecules by comparison of the peak areas of the different components. Surprisingly, the temperature where the reaction reaches a maximum coincides with the reaction onset for TAH in powder form (see Figure S3). The catalytic contribution of Au(111) to the polymerization reaction is thus minimal, suggesting that the film growth presented here is not support-specific and thus likely translatable. However, for purely thermal activation, the support must bind the TAH molecules sufficiently strongly to prevent complete desorption before the reaction temperature (as observed on HOPG).

Such films formed on Au(111) by thermal synthesis are only shown in Figure 4. At very low coverages (Figure 4a), small monolayer islands are formed that seem to follow the herringbone reconstruction by occupying preferentially fcc areas. Interestingly, at higher coverages (Figure 4b), second-layer molecules and agglomerates are observed before the first layer is completed, reflected in a highly corrugated line profile (Figure 4c) similar to that observed for the photochemical activation followed by annealing. The height levels of the monolayer and second-layer molecules correspond to those observed for the other activation methods. The XPS spectra in the N 1s and C 1s regions also appear similar to those in Figure 2. The main peaks arising from the heptazine ring and core (and their shake-up peak labeled "π-excitation"[37]), as well as the combined side group signal of bridging and terminal nitrogen atoms, from here on called N (side) atoms, correspond in their intensities (see Section S5 and Table S3 therein).

A direct, quantitative evaluation of the nitrogen species present in the N 1s spectra (Section S5) can help elucidate the carbon nitride stoichiometry and hence the type of network linking. In Table S3, we calculate the ratio of N (side) atoms per heptazine unit as the ratio of the relative intensities of the N (side) peak—that takes into account azo and amine linker species—to the heptazine core and ring N 1s signals, which together represent 7 N atoms or one heptazine unit. For both, the thermal and the photochemical + thermal preparations discussed in Figures 2 and 4, we obtain similar values in the range of 2.0−2.5 N (side) atoms per heptazine unit. We can compare these values with the numbers expected for different linking motifs (Table S2) and conclude that the obtained network contains more linking nitrogen atoms per heptazine unit than expected for a perfect 2D network formed by tertiary (1.0) or secondary amine nodes (1.5)—the linking motifs postulated, e.g., by Gillan for TAH-derived carbon nitride

https://doi.org/10.1021/acs.chemmater.3c01030
Chem. Mater. 2023, 35, 6762−6770

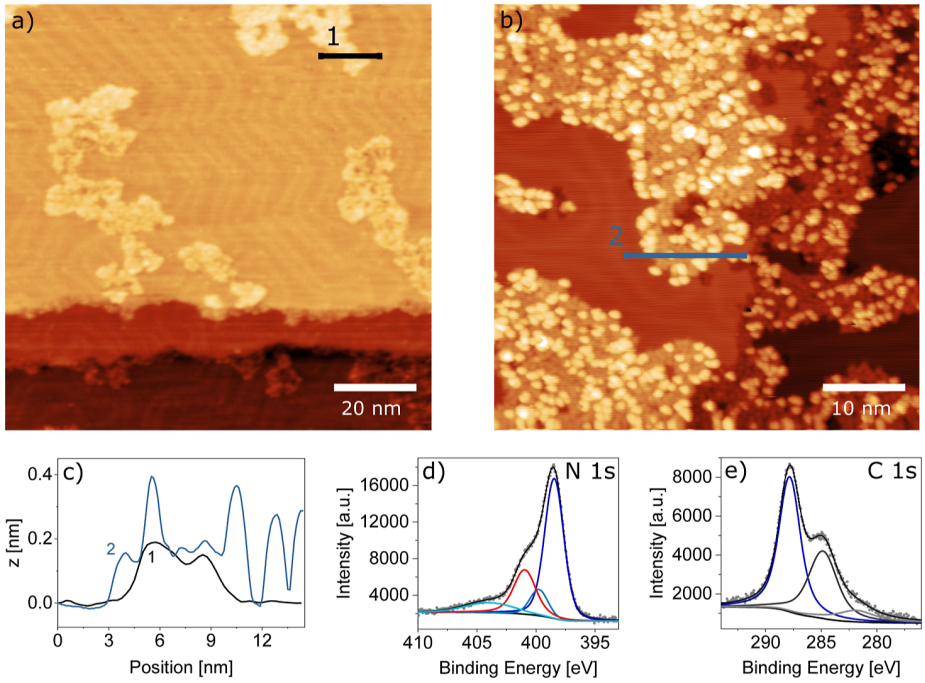

Figure 4. Thermal on-surface synthesis of carbon nitride films. (a) At a low coverage, it becomes apparent that the network grows in small islands which are constrained predominantly into the fcc areas of the Au(111) herringbone reconstruction. (b) At a higher coverage, the island area increases. Again, second-layer molecules are observed and reveal an inherent tendency of the molecules to stack. Both STM images were recorded after thermal polymerization. (c) Height profiles from (a,b) show single-layer islands for the low-coverage and single-layer islands with second-layer molecules on top for the higher coverage preparation. (d,e) XPS data in the N 1s and C 1s regions, respectively, show that the film formed by the thermal reaction is comparable to that from photoreaction shown in Figure 2. Peak colors are assigned as before: Conjugated heptazine ring (dark blue), central tertiary amine (blue), π-excitation (light blue), and linking amines and azo components (red). The corresponding C 1s peak contains components of the heptazine (dark blue), adventitious carbon (black), and an unknown component (gray). STM imaging parameters: U_b = 1.5 V; (a) I_t = 300 pA and (b) I_t = 200 pA.

powders.[22] Azo groups, instead, and terminal amines have more N (side) atoms per heptazine unit (3.0). Thus, we can as well exclude that our networks are exclusively azo-linked. The irreversible covalent bond formation upon polymerization favors rather amorphous and defect-rich networks with a high amount of terminal amines. Without their separate quantification, a clear attribution of the linking motifs remains elusive.

The N_2 TPD traces resulting from these two preparation pathways (see inset in Figure 3b) indicate that after the photoreaction—UV illumination at 150 (pink), resp. 300 K (green)—a third of the azide groups still remains intact. This intensity ratio supports the hypothesis that two of the three azide groups per molecule have reacted to a nitrene. If their reactivity is quenched by a direct nitrenoid bond to the gold support, this would point to an upright adsorption geometry of the molecules, as hypothesized for the striped patterns observed via STM in Figure 2b and in analogy to the structures discussed in the literature by Luo et al.[31] and Lin et al.[38] Furthermore, we note a slight difference in the shape of the TPD traces concerning the onset of the table-top desorption signal that occurs at slightly higher temperatures for the previously illuminated sample.

In the final step, we evaluated the stability of the carbon nitride film on Au(111) in air. For this purpose, the as-evaporated TAH film was transported through air and subsequently exposed to UV light in a tube furnace under vacuum. The resulting surface observed by ambient STM shown in Figure 5a exhibits a remarkably flat film with a similarly holey network as the films prepared under UHV

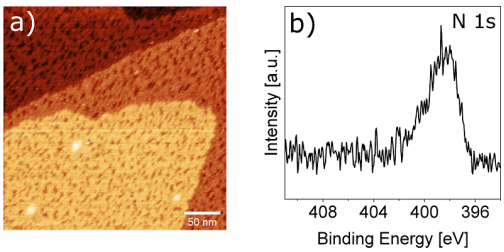

Figure 5. Stability of the carbon nitride film in air. (a) STM image of the film under ambient conditions (air, RT) after evaporation in a high vacuum setup, transport through air, and subsequent illumination with UV light (385 nm) at RT in an evacuated quartz tube with a background pressure of 1 × 10^{-2} mbar. STM imaging parameters: U_b = −215 mV, I_t = 200 pA. (b) XPS N 1s region after equivalent preparation conditions.

conditions. The N 1s spectrum taken after transferring back into a UHV chamber agrees well with the equivalent measurements in Figures 1−4, but we refrain from fitting the spectrum due to a poorer signal-to-noise ratio. The interpretation of the C 1s region is more difficult due to the presence of a large adventitious carbon peak from air-borne adsorbates. Nevertheless, we can conclude that the obtained carbon nitride films are stable in air and can thus be used as supports for ambient pressure experiments.

CONCLUSIONS

In conclusion, we have demonstrated several pathways for on-surface synthesis of carbon nitride films starting from a single,

https://doi.org/10.1021/acs.chemmater.3c01030
Chem. Mater. 2023, 35, 6762−6770

azide-functionalized precursor with a heptazine core, namely TAH. The simplicity of our approach lies in this particular, highly reactive precursor that has previously already been explored in powder chemistry. Here, we showed that we can successfully evaporate this relatively large molecule just before thermal activation of the azide occurs. We successfully polymerized the deposited TAH molecules by (a) X-ray illumination (and concomitant secondary electron emission), (b) UV light illumination and subsequent annealing, and (c) purely thermal activation. All three pathways lead to a similar, somewhat holey, 2D film that is stable in UHV and ambient conditions. We demonstrate that the created amorphous film is largely homogeneous, its stoichiometry pointing to various linking motifs. The UV-illuminated film provides an interesting insight into a partially reacted intermediate state before full polymerization by thermal annealing. We interpret the intermediates as upright-standing nitrenoids with strong direct nitrene−gold bonds. While gold thus stabilizes intermediates, it does not have a catalytic role in the thermal polymerization reaction.

The presented synthesis route constitutes a highly versatile tool for preparing thin 2D carbon nitride films, which can be included in stacked 2D materials or utilized as supports for nanoparticle experiments in vacuum, gas phase, and likely also liquid environments. Similar preparations have been shown to successfully immobilize even single metal ions for catalytic applications. Here, we anticipate particularly their use as highly stable confining pores for supported nanoparticles in harsh (electro)catalytic environments. Specifically, we envisage the combination of the on-surface synthesis of 2D carbon nitride films with our recently demonstrated approach to deposit size-selected clusters from polyoxometalate precursors in situ to be highly promising for atomic-scale studies on photo(electro)-catalytic water splitting environments.

■ ASSOCIATED CONTENT

Supporting Information

The Supporting Information is available free of charge at https://pubs.acs.org/doi/10.1021/acs.chemmater.3c01030.

Reaction scheme of the polymerization reaction; description of the TAH synthesis and characterization of its purity; mass spectra of the TAH evaporation process; XPS and STM reference measurements on the TAH azide activation on HOPG via X-ray-induced electron activation; and XPS analysis of the heptazine network on Au(111), as formed by the photo + thermal and the purely thermal reaction (PDF)

■ AUTHOR INFORMATION

Corresponding Author

Friedrich Esch − *TUM School of Natural Sciences, Department of Chemistry, Chair of Physical Chemistry, Technical University of Munich, Garching D-85748, Germany; Catalysis Research Center, Technical University of Munich, Garching D-85748, Germany;* orcid.org/0000-0001-7793-3341; Email: friedrich.esch@tum.de

Authors

Matthias Krinninger − *TUM School of Natural Sciences, Department of Chemistry, Chair of Physical Chemistry and TUM School of Natural Sciences, Department of Chemistry, Functional Nanomaterials Group, Technical University of Munich, Garching D-85748, Germany; Catalysis Research Center, Technical University of Munich, Garching D-85748, Germany;* orcid.org/0000-0002-8357-9323

Nicolas Bock − *TUM School of Natural Sciences, Department of Chemistry, Chair of Physical Chemistry, Technical University of Munich, Garching D-85748, Germany; Catalysis Research Center, Technical University of Munich, Garching D-85748, Germany;* orcid.org/0000-0002-4990-8533

Sebastian Kaiser − *TUM School of Natural Sciences, Department of Chemistry, Chair of Physical Chemistry, Technical University of Munich, Garching D-85748, Germany; Catalysis Research Center, Technical University of Munich, Garching D-85748, Germany;* orcid.org/0000-0001-8474-6261

Johanna Reich − *TUM School of Natural Sciences, Department of Chemistry, Functional Nanomaterials Group, Technical University of Munich, Garching D-85748, Germany; Catalysis Research Center, Technical University of Munich, Garching D-85748, Germany;* orcid.org/0000-0001-5065-5871

Tobias Bruhm − *TUM School of Natural Sciences, Department of Chemistry, Professorship of Inorganic Chemistry, Technical University of Munich, Garching D-85748, Germany; Catalysis Research Center, Technical University of Munich, Garching D-85748, Germany*

Felix Haag − *TUM School of Natural Sciences, Department of Physics, Chair of Experimental Physics (E20), Technical University of Munich, Garching D-85748, Germany*

Francesco Allegretti − *TUM School of Natural Sciences, Department of Physics, Chair of Experimental Physics (E20), Technical University of Munich, Garching D-85748, Germany;* orcid.org/0000-0001-6141-7166

Ueli Heiz − *TUM School of Natural Sciences, Department of Chemistry, Chair of Physical Chemistry, Technical University of Munich, Garching D-85748, Germany; Catalysis Research Center, Technical University of Munich, Garching D-85748, Germany;* orcid.org/0000-0002-9403-1486

Klaus Köhler − *TUM School of Natural Sciences, Department of Chemistry, Professorship of Inorganic Chemistry, Technical University of Munich, Garching D-85748, Germany; Catalysis Research Center, Technical University of Munich, Garching D-85748, Germany;* orcid.org/0000-0003-3008-7875

Barbara A. J. Lechner − *TUM School of Natural Sciences, Department of Chemistry, Functional Nanomaterials Group, Technical University of Munich, Garching D-85748, Germany; Catalysis Research Center, Technical University of Munich, Garching D-85748, Germany; Institute for Advanced Study, Technical University of Munich, Garching D-85748, Germany;* orcid.org/0000-0001-9974-1738

Complete contact information is available at: https://pubs.acs.org/10.1021/acs.chemmater.3c01030

Notes

The authors declare no competing financial interest.

■ ACKNOWLEDGMENTS

The authors thank Astrid De Clercq, Peter S. Deimel, Peter Feulner, Johannes Küchle, and Johannes V. Barth for experimental support and helpful discussions. This work was funded by the Deutsche Forschungsgemeinschaft (DFG,

German Research Foundation) under Germany's Excellence Strategy EXC 2089/1-390776260, through the project CRC1441 (project number 426888090), as well as by the grant ES 349/4-1 and TUM International Graduate School of Science and Engineering (IGSSE) via DFG, GSC 81. It received funding from the European Union's Horizon 2020 research and innovation programme under grant agreement no. 101007417 within the framework of the NFFA-Europe Pilot Joint Activities and under grant agreement no. 850764 from the European Research Council (ERC). B.A.J.L. gratefully acknowledges financial support from the Young Academy of the Bavarian Academy of Sciences and Humanities.

REFERENCES

(1) Wang, X.; Blechert, S.; Antonietti, M. Polymeric graphitic carbon nitride for heterogeneous photocatalysis. *ACS Catal.* **2012**, *2*, 1596−1606.
(2) Kumar, P.; Vahidzadeh, E.; Thakur, U. K.; Kar, P.; Alam, K. M.; Goswami, A.; Mahdi, N.; Cui, K.; Bernard, G. M.; Michaelis, V. K.; Shankar, K. C3N5: a low bandgap semiconductor containing an azo-linked carbon nitride framework for photocatalytic, photovoltaic and adsorbent applications. *J. Am. Chem. Soc.* **2019**, *141*, 5415−5436.
(3) Schlomberg, H.; Kröger, J.; Savasci, G.; Terban, M. W.; Bette, S.; Moudrakovski, I.; Duppel, V.; Podjaski, F.; Siegel, R.; Senker, J.; Dinnebier, R. E.; Ochsenfeld, C.; Lotsch, B. V. Structural insights into poly (heptazine imides): a light-storing carbon nitride material for dark photocatalysis. *Chem. Mater.* **2019**, *31*, 7478−7486.
(4) Lau, V. W.-h.; Lotsch, B. V. A Tour-Guide through Carbon Nitride-Land: Structure-and Dimensionality-Dependent Properties for Photo (Electro) Chemical Energy Conversion and Storage. *Adv. Energy Mater.* **2022**, *12*, 2101078.
(5) Wang, X.; Maeda, K.; Thomas, A.; Takanabe, K.; Xin, G.; Carlsson, J. M.; Domen, K.; Antonietti, M. A metal-free polymeric photocatalyst for hydrogen production from water under visible light. *Nat. Mater.* **2009**, *8*, 76−80.
(6) Yu, X.; Ng, S.-F.; Putri, L. K.; Tan, L.-L.; Mohamed, A. R.; Ong, W.-J. Point-defect engineering: leveraging imperfections in graphitic carbon nitride (g-C3N4) photocatalysts toward artificial photosynthesis. *Small* **2021**, *17*, 2006851.
(7) Li, Y.-Y.; Si, Y.; Zhou, B.-X.; Huang, W.-Q.; Hu, W.; Pan, A.; Fan, X.; Huang, G.-F. Strategy to boost catalytic activity of polymeric carbon nitride: synergistic effect of controllable in situ surface engineering and morphology. *Nanoscale* **2019**, *11*, 16393−16405.
(8) Chen, Z.; Vorobyeva, E.; Mitchell, S.; Fako, E.; Ortuño, M. A.; López, N.; Collins, S. M.; Midgley, P. A.; Richard, S.; Vilé, G.; Pérez-Ramírez, J. A heterogeneous single-atom palladium catalyst surpassing homogeneous systems for Suzuki coupling. *Nat. Nanotechnol.* **2018**, *13*, 702−707.
(9) Hosseini, S. M.; Ghiaci, M.; Farrokhpour, H. The adsorption of small size Pd clusters on a g-C3N4 quantum dot: DFT and TD-DFT study. *Mater. Res. Express* **2019**, *6*, 105079.
(10) Crampton, A. S.; Rötzer, M. D.; Landman, U.; Heiz, U. Can support acidity predict sub-nanometer catalyst activity trends? *ACS Catal.* **2017**, *7*, 6738−6744.
(11) Fukamori, Y.; König, M.; Yoon, B.; Wang, B.; Esch, F.; Heiz, U.; Landman, U. Fundamental insight into the substrate-dependent ripening of monodisperse clusters. *ChemCatChem* **2013**, *5*, 3330−3341.
(12) Kessler, F. K.; Zheng, Y.; Schwarz, D.; Merschjann, C.; Schnick, W.; Wang, X.; Bojdys, M. J. Functional carbon nitride materials—design strategies for electrochemical devices. *Nat. Rev. Mater.* **2017**, *2*, 17030−17117.
(13) Guo, F.; Hu, B.; Yang, C.; Zhang, J.; Hou, Y.; Wang, X. On-surface polymerization of in-plane highly ordered carbon nitride nanosheets toward photocatalytic mineralization of mercaptan gas. *Adv. Mater.* **2021**, *33*, 2101466.
(14) Burdina, K. P.; Zorov, N. B.; Kravchenko, O. V.; Kuzyakov, Y. Y.; Kim, J. I.; Kulinich, S. A. Synthesis of crystalline carbon nitride. *Mendeleev Commun.* **2000**, *10*, 207−208.
(15) Kouvetakis, J.; Todd, M.; Wilkens, B.; Bandari, A.; Cave, N. Novel synthetic routes to carbon-nitrogen thin films. *Chem. Mater.* **1994**, *6*, 811−814.
(16) Li, C.; Cao, C.-B.; Zhu, H.-S. Graphitic carbon nitride thin films deposited by electrodeposition. *Mater. Lett.* **2004**, *58*, 1903−1906.
(17) Sima, M.; Vasile, E.; Sima, A.; Preda, N.; Logofatu, C. Graphitic carbon nitride based photoanodes prepared by spray coating method. *Int. J. Hydrogen Energy* **2019**, *44*, 24430−24440.
(18) Algara-Siller, G.; Severin, N.; Chong, S. Y.; Björkman, T.; Palgrave, R. G.; Laybourn, A.; Antonietti, M.; Khimyak, Y. Z.; Krasheninnikov, A. V.; Rabe, J. P.; Kaiser, U.; Cooper, A. I.; Thomas, A.; Bojdys, M. J. Triazine-based graphitic carbon nitride: a two-dimensional semiconductor. *Angew. Chem., Int. Ed.* **2014**, *53*, 7450−7455.
(19) Bojdys, M. J.; Severin, N.; Rabe, J. P.; Cooper, A. I.; Thomas, A.; Antonietti, M. Exfoliation of crystalline 2D carbon nitride: thin sheets, scrolls and bundles via mechanical and chemical routes. *Macromol. Rapid Commun.* **2013**, *34*, 850−854.
(20) Gillan, E. G. Synthesis of nitrogen-rich carbon nitride networks from an energetic molecular azide precursor. *Chem. Mater.* **2000**, *12*, 3906−3912.
(21) Miller, D. R.; Swenson, D. C.; Gillan, E. G. Synthesis and structure of 2, 5, 8-triazido-s-heptazine: An energetic and luminescent precursor to nitrogen-rich carbon nitrides. *J. Am. Chem. Soc.* **2004**, *126*, 5372−5373.
(22) Miller, D. R.; Holst, J. R.; Gillan, E. G. Nitrogen-rich carbon nitride network materials via the thermal decomposition of 2, 5, 8-triazido-s-heptazine. *Inorg. Chem.* **2007**, *46*, 2767−2774.
(23) Saplinova, T.; Bakumov, V.; Gmeiner, T.; Wagler, J.; Schwarz, M.; Kroke, E. 2,5,8-Trihydrazino-s-heptazine: A precursor for heptazine-based iminophosphoranes. *Z. Anorg. Allg. Chem.* **2009**, *635*, 2480−2487.
(24) Schwarzer, A.; Saplinova, T.; Kroke, E. Tri-s-triazines (s-heptazines)-From a "mystery molecule" to industrially relevant carbon nitride materials. *Coord. Chem. Rev.* **2013**, *257*, 2032−2062.
(25) Jiang, J.; Ou-yang, L.; Zhu, L.; Zheng, A.; Zou, J.; Yi, X.; Tang, H. Dependence of electronic structure of g-C3N4 on the layer number of its nanosheets: a study by Raman spectroscopy coupled with first-principles calculations. *Carbon* **2014**, *80*, 213−221.
(26) Zheng, W.; Wong, N.-B.; Wang, W.; Zhou, G.; Tian, A. Theoretical study of 1, 3, 4, 6, 7, 9, 9b-heptaazaphenalene and its ten derivatives. *J. Phys. Chem. A* **2004**, *108*, 97−106.
(27) L'abbe, G. Decomposition and addition reactions of organic azides. *Chem. Rev.* **1969**, *69*, 345−363.
(28) Diaz Arado, O.; Mönig, H.; Wagner, H.; Franke, J.-H.; Langewisch, G.; Held, P. A.; Studer, A.; Fuchs, H. On-surface azide−alkyne cycloaddition on Au (111). *ACS Nano* **2013**, *7*, 8509−8515.
(29) Hellerstedt, J.; Cahlík, A.; Stetsovych, O.; Švec, M.; Shimizu, T. K.; Mutombo, P.; Klívar, J.; Stará, I. G.; Jelínek, P.; Starý, I. Aromatic azide transformation on the Ag (111) surface studied by scanning probe microscopy. *Angew. Chem.* **2019**, *131*, 2288−2293.
(30) Haase, F.; Lotsch, B. V. Solving the COF trilemma: towards crystalline, stable and functional covalent organic frameworks. *Chem. Soc. Rev.* **2020**, *49*, 8469−8500.
(31) Luo, Y.-W.; Chou, C.-H.; Lin, P.-C.; Chiang, C.-M. Photochemical Synthesis of Azoarenes from Aryl Azides on Cu (100): A Mechanism Unraveled. *J. Phys. Chem. C* **2019**, *123*, 12195−12202.
(32) Yan, G.; Feng, X.; Xiao, L.; Xi, W.; Tan, H.; Shi, H.; Wang, Y.; Li, Y. Tuning of the photocatalytic performance of gC 3 N 4 by polyoxometalates under visible light. *Dalton Trans.* **2017**, *46*, 16019−16024.
(33) Bock, N.; De Clercq, A.; Seidl, L.; Kratky, T.; Ma, T.; Günther, S.; Kortz, U.; Heiz, U.; Esch, F. Towards Size-Controlled Deposition of Palladium Nanoparticles from Polyoxometalate Precursors: An

https://doi.org/10.1021/acs.chemmater.3c01030
Chem. Mater. 2023, 35, 6762−6770

Electrochemical Scanning Tunneling Microscopy Study. *ChemElectroChem* **2021**, *8*, 1280−1288.
(34) Sattler, A. Investigations into s-Heptazine-Based Carbon Nitride Precursors. Ph.D. Thesis, Ludwig-Maximilians-Universität (LMU), Munich, 2010.
(35) Wilms, M.; Kruft, M.; Bermes, G.; Wandelt, K. A new and sophisticated electrochemical scanning tunneling microscope design for the investigation of potentiodynamic processes. *Rev. Sci. Instrum.* **1999**, *70*, 3641−3650.
(36) Kaiser, S.; Maleki, F.; Zhang, K.; Harbich, W.; Heiz, U.; Tosoni, S.; Lechner, B. A.; Pacchioni, G.; Esch, F. Cluster catalysis with lattice oxygen: Tracing oxygen transport from a magnetite (001) support onto small Pt clusters. *ACS Catal.* **2021**, *11*, 9519−9529.
(37) Zhang, J. R.; Ma, Y.; Wang, S. Y.; Ding, J.; Gao, B.; Kan, E.; Hua, W. Accurate K-edge X-ray photoelectron and absorption spectra of g-C3N4 nanosheets by first-principles simulations and reinterpretations. *Phys. Chem. Chem. Phys.* **2019**, *21*, 22819−22830.
(38) Lin, Y.-P.; Ourdjini, O.; Giovanelli, L.; Clair, S.; Faury, T.; Ksari, Y.; Themlin, J.-M.; Porte, L.; Abel, M. Self-assembled melamine monolayer on Cu (111). *J. Phys. Chem. C* **2013**, *117*, 9895−9902.
(39) Bonanni, S.; Aït-Mansour, K.; Hugentobler, M.; Brune, H.; Harbich, W. An experimental setup combining a highly sensitive detector for reaction products with a mass-selected cluster source and a low-temperature STM for advanced nanocatalysis measurements. *Eur. Phys. J. D* **2011**, *63*, 241−249.

https://doi.org/10.1021/acs.chemmater.3c01030
Chem. Mater. 2023, 35, 6762−6770

Supporting Information for On-Surface Carbon Nitride Growth from Polymerization of 2,5,8-Triazido-*s*-heptazine

Matthias Krinninger,[†,‡,¶] Nicolas Bock,[†,‡] Sebastian Kaiser,[†,‡] Johanna Reich,[¶,‡] Tobias Bruhm,[§,‡] Felix Haag,[‖] Francesco Allegretti,[‖] Ueli Heiz,[†,‡] Klaus Köhler,[§,‡] Barbara A.J. Lechner,[¶,‡,⊥] and Friedrich Esch[*,†,‡]

†*Technical University of Munich, TUM School of Natural Sciences, Department of Chemistry, Chair of Physical Chemistry, Lichtenbergstr. 4,D-85748 Garching, Germany*

‡*Catalysis Research Center, Technical University of Munich, Ernst-Otto-Fischer-Str. 1, D-85748 Garching, Germany*

¶*Technical University of Munich, TUM School of Natural Sciences, Department of Chemistry, Functional Nanomaterials Group, Lichtenbergstr. 4, D-85748 Garching, Germany*

§*Technical University of Munich, TUM School of Natural Sciences, Department of Chemistry, Professorship of Inorganic Chemistry, Lichtenbergstr. 4, D-85748 Garching, Germany*

‖*Technical University of Munich, TUM School of Natural Sciences, Department of Physics, Chair of Experimental Physics (E20), James-Franck Str. 1, D-85748 Garching, Germany*

⊥*Institute for Advanced Study, Technical University of Munich, Lichtenbergstr. 2a, D-85748 Garching, Germany*

E-mail: friedrich.esch@tum.de

S1. Polymerization reaction

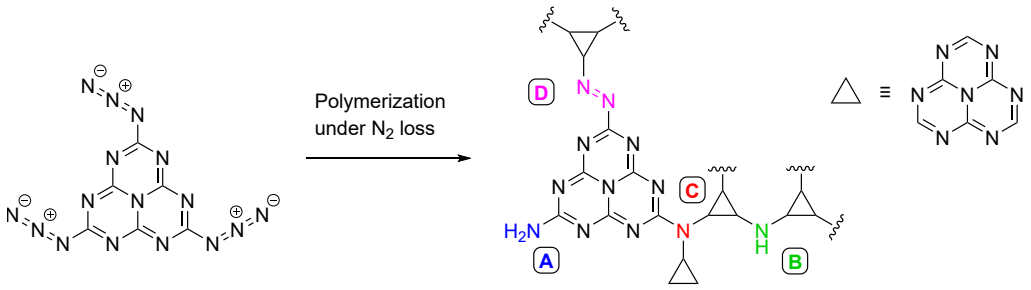

Figure S1: Reaction scheme showing the suggested pathway from 2,5,8-triazido-s-heptazine (TAH) to the 2D polyheptazine-based network. The azide groups decompose under nitrogen loss, forming nitrene intermediates. Their coupling, assuming that the π-bonded core remains intact, is discussed in the literature to proceed to the indicated products: terminal primary amines (A), linking via secondary amines - leading to poly(heptazine imides) - (B), 2D linking via tertiary amines (C) or via azo groups (D). Tertiary amines, found in the polymerization of TAH powders, might be formed by the sequential nitrene attack of azo-coupled nitrogens, under N_2 loss.

S2. TAH synthesis and characterization of purity

The synthesis of 2,5,8-triazido-*s*-heptazine (TAH) followed the reports of Sattler et al.[1] and Saplinova et al.[2] In a first step, melamine was heated to 663 K in a porcelain crucible, covered with a lid, in a muffle furnace for 24 hours. In order to remove undesired side products, the raw product was then heated under reflux in acetic acid for 3 hours to get the *s*-heptazine based melem (2,5,8-triamino-*s*-heptazine).

In the next step, the amino groups of melem were converted into hydrazine groups. To that purpose, the suspension of melem in hydrazine monohydrate was heated to 413 K for 24 hours in a glass lined stainless steel autoclave. The reaction mixture was purified by repetitive dissolution in hydrochloric acid, filtration and precipitation by addition of sodium hydroxide solution. The thus obtained product, 2,5,8-trihydrazino-*s*-heptazine was suspended in hydrochloric acid and dropped into a 278 K cold solution of $NaNO_2$ in hydrochloric acid. After stirring for 3 hours, the solid was filtered off, washed with water and ethanol to yield the final product TAH.

To characterize the purity of the obtained TAH precursor, we performed ^{13}C-NMR, ATR-FTIR and Raman spectroscopy (see Fig. S2), as well as elemental analysis, and compared to the characterization by Miller.[3,4] While both ^{13}C-NMR spectra show only two carbon signals, as expected for a pure precursor, our elemental analysis contains much less residual hydrogen (0.13 wt% as compared to 0.88 wt% in ref.[3]).

The ATR-FTIR spectrum of TAH in Fig. S2a shows the characteristic peak at 817 cm^{-1}, representative for triazine and heptazine ring breathing modes, a bunch of vibrational C−N and C=N modes in the $1200 - 1700$ cm^{-1} region and the characteristic azide modes at $2144 - 2229$ cm^{-1}, while N−H stretching mode in the range between 3300 and 3500 cm^{-1} are missing. Most of these peaks are also found in the Raman spectrum of the TAH precursor in Fig. S2b.

When reacting the powder at the indicated temperatures in vacuum or in argon (upper spectra in Fig. S2a), one observes the disappearance of the azide peaks, while the heptazine

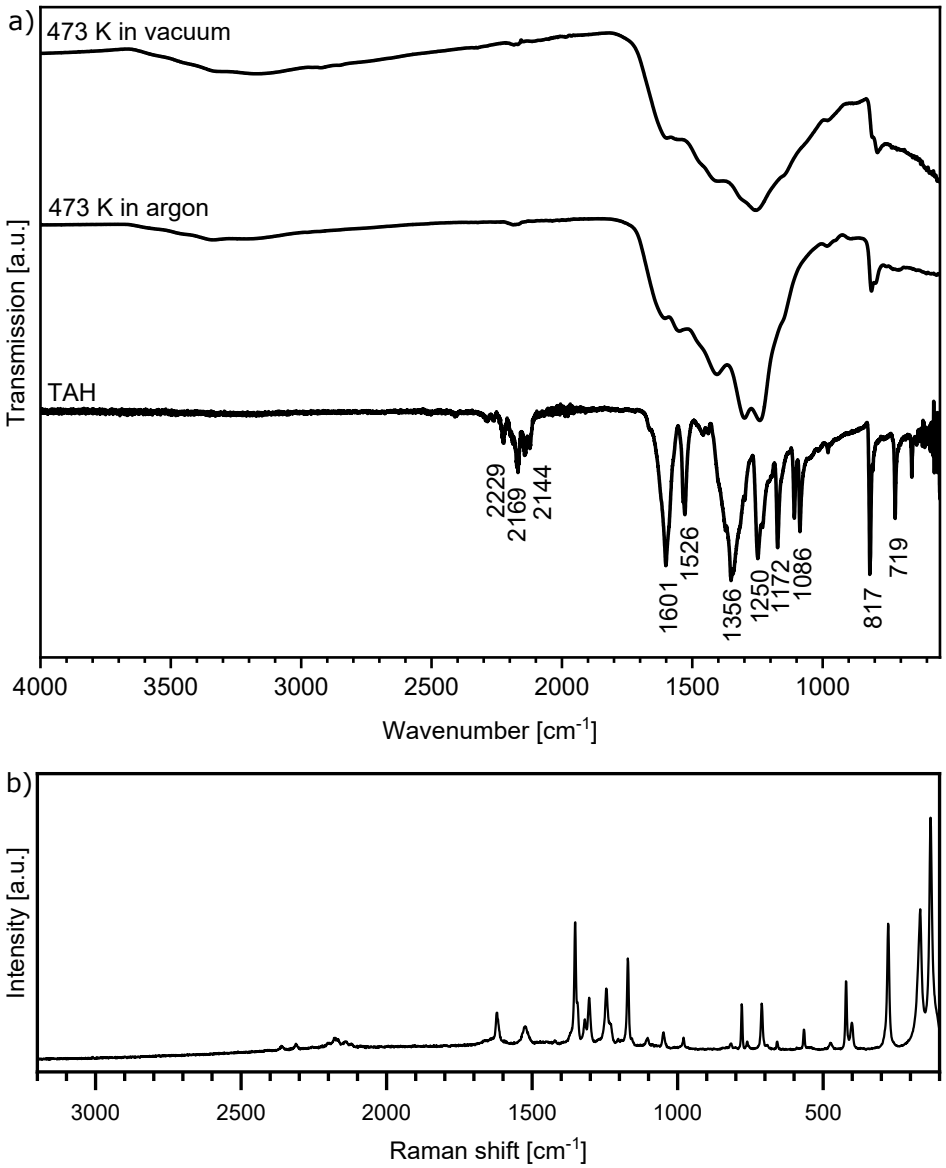

Figure S2: Characterization of the TAH precursor powder and its annealing products by vibrational spectroscopy: (a) ATR-FTIR spectra of TAH (bottom spectrum) and reaction products after heating to 473 K under argon (center) or in vacuum conditions (top spectrum). The TAH molecule can be identified by the s-heptazine, triazine and azide vibrations (see text and detailed list below). The azide contribution at $2144 - 2229$ cm^{-1} disappears for the reacted carbon nitride, while N−H species form. (b) Raman spectrum of TAH.

ring breathing mode at 817 cm^{-1} persists, although as a broader feature, indicating that the conjugated ring structure remains intact. In the azide peak region, a small peak at 2190 cm^{-1} remains that Miller et al. assign to the possible formation of imine side products (=C=NH, nitrile −C≡N, or diimide −N=C=N−.[4]

^{13}C-NMR (101 MHz, DMSO-d6) δ(ppm) = 158.8 (s, N=C−N), 171.5 (s, C−N_3).

Elemental analysis (wt%): Calc. C (24.33), N (75.67); Found C (24.15), N (73.64), H (0.13).

FTIR (ATR, 25 °C, cm^{-1}): 2406 (w), 2284 (w), 2229 (w), 2169 (m), 2144 (w), 2118 (w), 1601 (s), 1526 (m), 1356 (s), 1250 (s), 1172 (s), 1106 (s), 1086 (s), 977 (w), 817 (s), 719 (s), 657 (m).

Raman (785 nm, 25 °C, cm^{-1}): 2361 (w), 2310 (w), 2176 (w), 2141 (w), 2121 (w), 1621 (w), 1522 (w), 1353 (s), 1318 (w), 1304 (m), 1246 (m), 1170 (m), 1102 (w), 1050 (w), 978 (w), 815 (w), 776 (m), 757 (w), 711 (m), 660 (w), 566 (w), 476 (w), 422 (m), 401 (w), 280 (s), 168 (s), 130 (s).

S3. TAH evaporation process

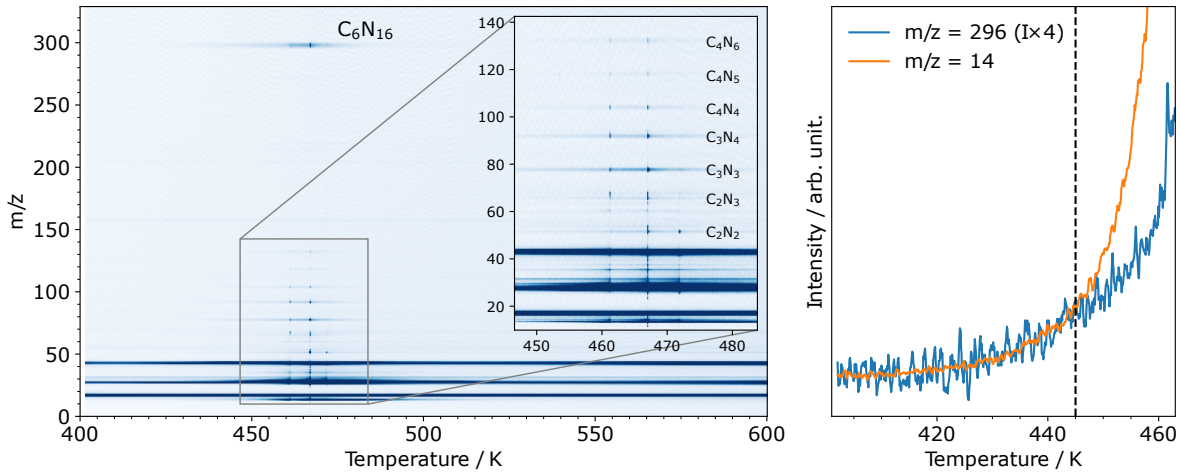

Figure S3: Thermal desorption of TAH powder from a crucible mounted in front of a quadrupole mass spectrometer. The mass spectra were measured from $m/z = 1$ to 600, by heating in high vacuum (p_{bg}<5×10^{-8} mbar) with a temperature ramp of 0.05 K/s.
(left) The overview scan that displays mass traces up to $m/z = 300$ clearly indicates a distinct peak of intact TAH (C_6N_{16}, $m/z = 296$), detected around 470 K, as well as several fragment signals in the range between $m/z = 52$ and $m/z = 132$, most likely originating from fragmentation in the QMS. We assign the fragment $m/z = 78$ to *s*-triazine (C_3N_3), which has a comparatively strong intensity thanks to its conjugated π-system. Further signals are present throughout the entire temperature range and arise from residual gases in the vacuum chamber, i.e. H_2O ($m/z = 18$), CO ($m/z = 28$) and CO_2 ($m/z = 44$). Distinct spikes in the fragment signals around the TAH desorption maximum hint at possible molecule ejection caused by autocatalytic microexplosions at slightly hotter spots inside the crucible-located powder. No polymerization products with $m/z > 300$ are detected.
(right) The signal $m/z = 14$ relates to nitrogen that stems from two processes: The decomposition of TAH in the crucible and the fragmentation of evaporated TAH in the QMS. We discriminate the two by overlaying the TAH signal ($m/z = 296$) onto the initial $m/z = 14$ rise. TAH decomposition in the powder and hence polymerization thus sets in at the temperature where the nitrogen curve starts to deviate from the TAH curve (indicated by a vertical dashed line). We therefore deduce the ideal evaporation temperature range to be just below 445 K.

S4. Reference measurements on HOPG

As illustrated in the thermal desorption spectra in Fig. 3a, the interaction of TAH with an HOPG support is substantially weaker than within the powder: TAH is not bound sufficiently strongly to activate the thermal decomposition before desorption. TAH on HOPG can, however, be activated by X-ray illumination. While TAH decomposes almost immediately on Au(111), making it impossible to trace the azide functionality in the N 1s XPS spectra, the activation on HOPG is less immediate. This difference in reactivity points to the involvement of secondary electrons in X-ray activation. It allows to prove intact azide adsorption on the HOPG support and its subsequent decomposition (Fig. S4) and to image the network that forms upon polymerization and subsequent annealing (Fig. S5).

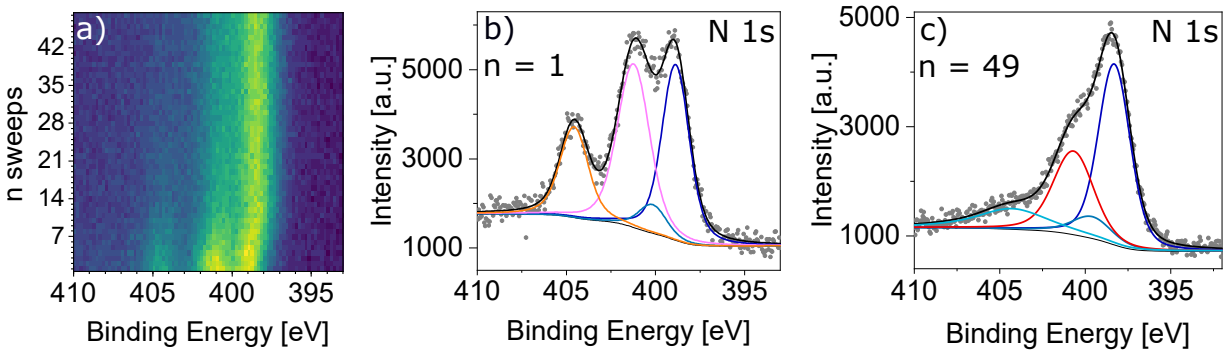

Figure S4: Series of N 1s XPS sweeps of a sub-ML TAH on HOPG (49 sweeps, time/sweep=3:49 min; n=1 after 8 min X-ray illumination, n=49 after 190 min). (a) The 2D plot of the sweeps indicates the azide loss, the transformation into amino or azo side groups and a concomitant shift in the heptazine nitrogen peaks that might be related to reordering on the support. (b) and (c) show detailed spectra for sweep n=1 and n=49 with peak fits by Voigt functions on a Shirley background. Binding energies, intensities and assignments are indicated in Table S1. While the first sweep can be described consistently as an azide layer with two azide and two heptazine nitrogen species (intensity ratio 3:6:1:6), the last sweep, n=49, consists in majority of a reacted heptazine layer with amino or azo side groups, while some intact azide groups are still present.

Table S1: N 1s XPS binding energies and relative peak intensities for the XPS data shown in Fig. S4b and c, with the color code that maps the respective fitted peaks. The obtained binding energies are altogether slightly shifted by about 0.6 eV with respect to those obtained on Au(111) (see Section S5), probably due to enhanced core hole shielding on the metal support. The π-excitation peak is relevant only for polymerized heptazine units. The ratio N (side) atoms per heptazine unit is calculated as ratio of the relative intensities (indicated by the colored bullets) and taking into account that the heptazine ring contains 7 N atoms. The indication of a range reflects exclusion, resp. inclusion of the π-excitation into the sum of heptazine relative peak intensities.

Peak	E_B [eV]		rel. intensity	
	n = 1	n = 49	n = 1	n = 49
● N (heptazine ring)	398.9	398.3	≡6	5.9
● N (heptazine core)	400.2	399.6	≡1	1.0
● N (π-excitation)	-	404.3	-	1.9
● N (azide - outer N's)	401.2	-	6.5	0
● N (azide - central N)	404.6	-	3.3	0
● N (side)	-	400.7	–	3.5
N (side) atoms (●) per heptazine unit (●●/●)	–	–	–	2.8 – 3.5

The XPS data allows us to estimate the average type of linking that results from the X-ray activation on HOPG. By comparing the obtained value of $\geq$ 2.8 N (side) atoms per heptazine unit with the values expected for different linking motifs in Table S2, we conclude that the obtained network contains more linking nitrogen atoms per heptazine unit than expected for a perfect 2D network formed by tertiary or secondary amine nodes. Note that the N (side) atom ratio is only indicative, since calculated from single sweeps.

Our values point rather to linear networks predominantly formed by azo groups or secondary amines, with a considerable presence of terminal amine groups that cannot be quantified separately. This is consistent with our observations in the STM images in Fig. S5: The loosely connected network, observed after short annealing to 676 K to remove residual azide groups and increase the surface order, is highly mobile and gets displaced by the scanning tip as seen in subsequent images.

Table S2: Number of N (side) atoms per heptazine unit for different types of linkers

Type of side group	Number N (side) per ring	Carbon nitride stoichiometry
Tertiary amine	1	C_3N_4
Secondary amine	1.5	$C_3N_{4.5}$
Primary (terminal) amine or azo group	3	C_3N_5

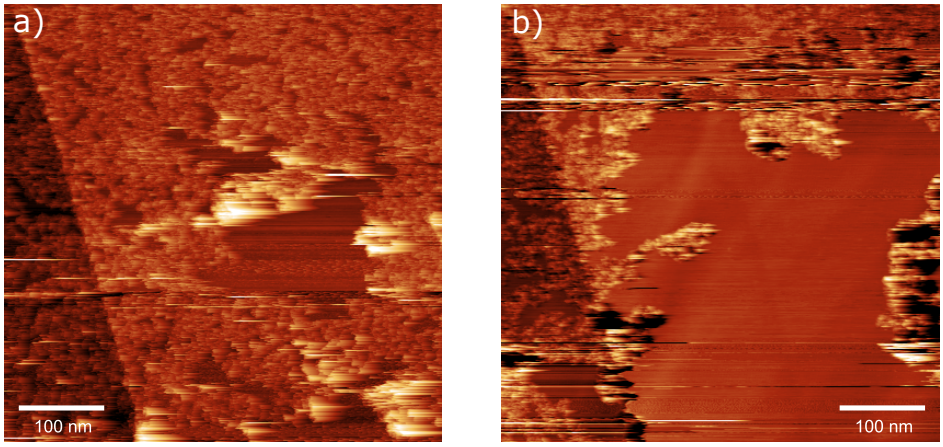

Figure S5: Two subsequent STM images of the heptazine network obtained by X-ray induced electron activation on HOPG and subsequent annealing to 676 K. The scanning tip continuously displaces the loosely connected molecule carpet, opening up large areas of the bare support especially where streaky, bright (strongly interacting) patches have been observed previously. *STM imaging parameters*: (a) $U_b = 3$ V, $I_t = 300$ pA, (b) $U_b = 2$ V, $I_t = 300$ pA.

S5. XPS analysis of the heptazine network on Au(111)

Table S3: XPS binding energies and relative peak intensities for the XPS data shown in the main text: a) after photochemical reaction of TAH with subsequent annealing (Fig. 2), b) after thermal reaction (Fig. 4). The color code maps the respective fitted peaks in the figures: Two nitrogen peaks fit the heptazine, one for the six ring atoms and one for the central tertiary amine atom, as well as a third broad peak that represents the π-excitation shake-up satellite related to the conjugated ring system. Linking or terminal amine or azo side groups appear all at similar binding energies and are represented by a single N (side) peak. This peak assignment and the relative binding energy values are in line with the compilation of experimental carbon nitride powder XPS spectra and their simulation by Zhang et al.,[5] although our observed binding energy values are lower by up to 1 eV, which might be related to the interaction with the support. The ratio N (side) atoms per heptazine unit is calculated as ratio of the relative intensities (indicated by the colored bullets) and taking into account that the heptazine ring contains 7 N atoms. The indication of a range reflects exclusion, resp. inclusion of the π-excitation into the sum of heptazine relative peak intensities. Contaminant peaks stemming from the deposition process are marked in grey: Adventitious carbon, also found for powder samples, as well as an unknown carbon species with very low, carbide-like binding energy, and an unknown nitrogen species with rather high binding energy that does not belong to amorphous carbon nitride.[6]

Peak	E_B [eV]	a) photo-+thermal reaction rel. intensity	b) thermal reaction rel. intensity
● N (heptazine ring)	397.9	≡6	≡6
● N (heptazine core)	399.2	≡1	≡1
● N (π-excitation)	403.4	1.6	1.0
● N (side)	400.4	2.5	2.3
● N (unknown)	402.3	1.1	–
N (side) atoms (●) per heptazine unit (●●/●)	–	2.0 – 2.5	2.0 – 2.3
● C (heptazine)	287.2	≡6	≡6
● C (adventitious carbon)	284.6	0.9	4.0
● C (unknown)	282.4	2.2	1.1

As the XPS analysis demonstrates, both preparation approaches lead to similar values of 2.0 – 2.3 and 2.0 – 2.5 N (side) atoms per heptazine unit, depending on whether or not the π-excitation is included. Comparing with the numbers expected for different linking motifs in Table S2, we can exclude that our networks are exclusively azo-linked. The irreversible

covalent bond formation upon polymerization favours rather amorphous and defect-rich networks with a high amount of terminal amines. Without their separate quantification, a clear attribution of the linking motifs remains elusive. The network is, however, more interconnected than on HOPG ($\geq$ 2.8 N (side) atoms per heptazine unit and high mobility in STM).

References

(1) Sattler, A. Investigations into s-Heptazine-Based Carbon Nitride Precursors. Ph.D. thesis, Ludwig-Maximilians-Universität (LMU), Munich, 2010.

(2) Saplinova, T.; Bakumov, V.; Gmeiner, T.; Wagler, J.; Schwarz, M.; Kroke, E. 2,5,8-Trihydrazino-s-heptazine: A precursor for heptazine-based iminophosphoranes. *Zeitschrift fur Anorganische und Allgemeine Chemie* **2009**, *635*, 2480–2487.

(3) Miller, D. R.; Swenson, D. C.; Gillan, E. G. Synthesis and structure of 2, 5, 8-triazido-s-heptazine: An energetic and luminescent precursor to nitrogen-rich carbon nitrides. *Journal of the American Chemical Society* **2004**, *126*, 5372–5373.

(4) Miller, D. R.; Holst, J. R.; Gillan, E. G. Nitrogen-rich carbon nitride network materials via the thermal decomposition of 2, 5, 8-triazido-s-heptazine. *Inorganic chemistry* **2007**, *46*, 2767–2774.

(5) Zhang, J. R.; Ma, Y.; Wang, S. Y.; Ding, J.; Gao, B.; Kan, E.; Hua, W. Accurate K-edge X-ray photoelectron and absorption spectra of g-C_3N_4 nanosheets by first-principles simulations and reinterpretations. *Physical Chemistry Chemical Physics* **2019**, *21*, 22819–22830.

(6) Titantah, J.; Lamoen, D. Carbon and nitrogen 1s energy levels in amorphous carbon nitride systems: XPS interpretation using first-principles. *Diamond and related materials* **2007**, *16*, 581–588.

5.2 Interface Effects in the Stability of 2D Silica, Silicide, and Silicene on Pt(111) and Rh(111)

Title: Interface Effects in the Stability of 2D Silica, Silicide, and Silicene on Pt(111) and Rh(111)

Authors: Matthias Krinninger, Florian Kraushofer, Nils B. Refvik, Monika Blum and Barbara A. J. Lechner

Journal: ACS Applied Materials & Interfaces **2024**, *16*, 27481–27489.

Status: Published May 15, 2024

DOI: 10.1021/acsami.4c05137

Contributions

Florian Kraushofer and I conducted all experiments and data analysis contained in this publication. Writing of the first draft and data visualization was done by me with subsequent iterations by Florian Kraushofer and Barbara A. J. Lechner. Nils Refvik helped in preliminary STM measurements of 2D silica on Rh(111) as part of his three-month visit. Monika Blum supported the XPS experiments as the beamline scientist at the ALS. Barbara A. J. Lechner provided funding acquisition, supervision and was involved in discussions.

Content

In this publication, we study 2D silica films on Pt(111) and Rh(111) as potential non-reducible model supports. We have achieved fully closed, amorphous films on

Pt(111) for the first time by following an established procedure, which consists of silicon deposition in an oxygen atmosphere and subsequent annealing, with the difference of depositing an excess amount of Si. We identify the interfacial buffer layer, consisting of a silicide or silicate, as the stabilizing factor for the complete film. Additionally, these films exhibit strong resistance to relatively high CO pressures of 0.8 mbar. Furthermore, we demonstrate an additional synthesis pathway by reaction from a surface silicide precursor. However, exposure to high temperatures in both oxidative and reductive conditions leads to the formation of holes in the 2D silica. Consequently, fully closed films are insufficiently stable for model catalysis studies at near-ambient pressures combined with elevated temperatures, while films with holes display high stability.

On Rh(111), we observe mixed morphologies for the same film preparation. Besides the main amorphous and "zigzag" structures, also ordered, crystalline structures, as well as holes, can be found. However, unlike Pt(111) and other underlying metal substrates, 2D silica on Rh(111) can be fully reduced by annealing at 665 K in UHV, yielding a surface silicide with a $(\sqrt{19} \times \sqrt{19})R23.4^{\circ}$ periodicity. For the reaction mechanism, we suggest an oxygen transfer from the silica film to Rh and subsequent thermal desorption of this oxygen, as the much higher heat of formation of SiO_2 compared to rhodium oxide would make the formation of this species thermodynamically less favorable. Although film recovery is hindered by significant Si loss to the Rh bulk or the gas phase as SiO, the initial reduction process is chemically fully reversible by reoxidation in an oxygen atmosphere.

ACS APPLIED MATERIALS & INTERFACES

www.acsami.org

Research Article

Interface Effects in the Stability of 2D Silica, Silicide, and Silicene on Pt(111) and Rh(111)

Matthias Krinninger, Florian Kraushofer, Nils B. Refvik, Monika Blum, and Barbara A. J. Lechner*

Cite This: *ACS Appl. Mater. Interfaces* 2024, 16, 27481−27489

Read Online

ACCESS | Metrics & More | Article Recommendations | Supporting Information

ABSTRACT: Ultrathin two-dimensional silica films have been suggested as highly defined conductive models for fundamental studies on silica-supported catalyst particles. Key requirements in this context are closed silica films that isolate the gas phase from the underlying metal substrate and stability under reaction conditions. Here, we present silica bilayer films grown on Pt(111) and Rh(111) and characterize them by scanning tunneling microscopy and X-ray photoelectron spectroscopy. We provide the first report of silica bilayer films on Rh(111) and have further successfully prepared fully closed films on Pt(111). Interestingly, surface and interface silicide phases play a decisive role in both cases: On platinum, closed films can be stabilized only when silicon is deposited in excess, which results in an interfacial silicide or silicate layer. We show that these silica films can also be grown directly from a surface silicide phase. In the case of rhodium, the silica phase is less stable and can be reduced to a silicide in reductive environments. Though similar in appearance to the "silicene" phases that have been controversially discussed on Ag(111), we conclude that an interpretation of the phase as a surface silicide is more consistent with our data. Finally, we show that the silica film on platinum is stable in 0.8 mbar CO but unstable at elevated temperatures. We thus conclude that these systems are only suitable as model catalyst supports to a limited extent.

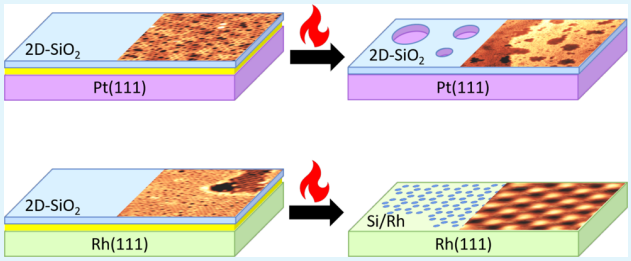

KEYWORDS: *silica thin films, silicide, model catalyst support, in situ, STM, XPS*

INTRODUCTION

Silica is a prototypical catalyst support material due to its high stability and low cost. To gain an atomic-scale understanding of catalytic processes, surface science experiments have traditionally been applied on simplified model catalysts.[1] Often, these studies—aiming to explore specific properties of supported catalyst particles in, e.g., ethylene hydrogenation[2,3] or CO oxidation[4] reactions—use relatively thick silicon dioxide (SiO_2) films of several nanometers.[5] However, the choice of experimental techniques is then limited by the extremely low conductivity of silica, and in particular, thick films are unsuitable for surface microscopy due to their inherent roughness. Hence, ultrathin two-dimensional (2D) silica films have been suggested as highly defined, conductive, and atomically flat models for fundamental studies on silica-supported catalysts.[6,7] To avoid side reactions, closed films that fully cover the underlying metal substrate are of key importance.

The structure of these films has been extensively studied over the last two decades, starting on Mo(112)[8] as an underlying substrate, with the first scanning tunneling microscopy (STM) images of its atomically resolved structure reported in 2005.[9] Here, a single-layer, 2D network could be grown that consists of highly ordered [SiO_4] tetrahedra as building blocks of which one oxygen atom is bound to a Mo atom of the surface. Later, a bilayer structure was found on Ru(0001) and termed "2D silica".[10,11] Because the Ru−O bond is weaker than the Mo−O one, none of the oxygen atoms of the building blocks are bound to the surface. Instead, they form two planes of corner-sharing tetrahedra with one oxygen bridging these two layers, while the bonding forces between the film and the underlying metal are only van der Waals interactions. These bilayers can be further categorized into crystalline, where the building blocks form exclusively six-membered rings and amorphous/vitreous films, with varying ring sizes of four to nine. Crystalline and amorphous films could be obtained selectively by tuning the cooling rate after the oxidative annealing step during the synthesis.[12] Over the years, 2D silica has also been reported on a variety of other substrates, including Pd(100),[13] Pd(111),[14,15] a Ni_xPd_{1-x}(111) alloy film,[16] Ru and Co nanoparticles,[17] Cu-supported graphene,[18,19] and Pt(111).[20]

Received: March 30, 2024
Revised: April 29, 2024
Accepted: May 7, 2024
Published: May 15, 2024

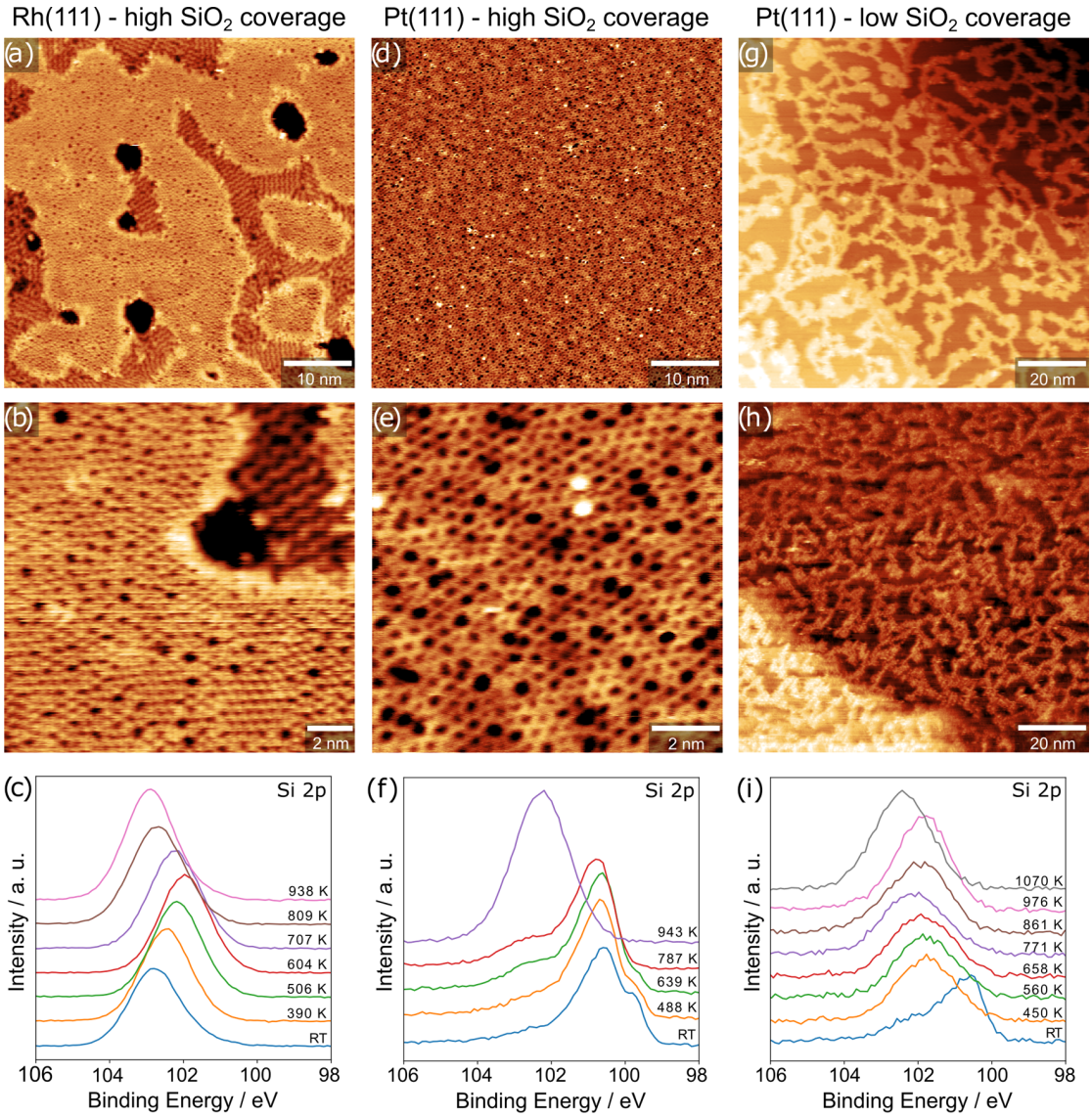

Figure 1. STM images of 2D silica and corresponding XPS Si 2p spectra acquired during film synthesis in 5.0×10^{-6} mbar O_2 for (a–c) a full monolayer on Rh(111), (d–f) a full monolayer on Pt(111) and (g–i) a submonolayer film on Pt(111), annealed at different temperatures. STM images were acquired in UHV at room temperature, with the following tunneling parameters: (a) I_t = 0.12 nA, V_b = 0.77 V, (b) I_t = 0.10 nA, V_b = 0.77 V, (d) I_t = 0.34 nA, V_b = 0.36 V, (e) I_t = 0.34 nA, V_b = 0.36 V, (g) I_t = 0.42 nA, V_b = 0.33 V, and (h) I_t = 0.65 nA, V_b = 4.51 V. XPS parameters: excitation energy of 300 eV.

The silica films exhibit high thermal stability, as shown on Mo(112) and Ru(0001).[21,22] On these substrates, "O-poor" and "O-rich" films could be prepared by annealing in UHV or in an oxygen atmosphere. The difference between these two films lies in the chemisorption of O at the surface under the film. While it is possible to convert "O-poor" films into "O-rich" films through oxygen annealing in the case of Mo(112), the UHV-annealing-based pathway in the opposite direction is blocked due to the high binding energy of oxygen to the Mo(112) surface.[21] In contrast, the transformation from one phase to the other is fully reversible on Ru(0001). This is reflected in X-ray photoelectron spectroscopy (XPS), where both the Si 2p and the O 1s peaks shift to higher binding energies by up to 0.8 eV after UHV annealing, depending on the temperature.[22]

Under oxygen-poor conditions, these silica phases are in competition with surface silicides, which have also been observed on most of the relevant metals. On Pt(111), surface segregation of Si impurities was reported to result in a $(\sqrt{19} \times \sqrt{19})R23.4°$ structure under high-temperature annealing.[23] A more systematic study by Nashner et al. used vapor-deposited SiH_4 to show that a variety of different surface silicide structures can be formed depending on the Si/Pt ratio at the surface.[24] In some cases, these silicon-rich phases have also been interpreted as a "silicene" with a structure akin to graphene: Feng et al. observed novel structures of Si on Ag(111) in STM and attributed them to different silicene phases.[25] Their model consists of hexagonally arranged, buckled six-rings that form a (4 × 4) reconstruction with respect to the underlying Ag(111). However, Švec et al. later proposed a model for the $(\sqrt{19} \times \sqrt{19})R23.4°$ silicide on Pt(111) and convincingly argued that the "silicene" phase on Ag(111) has the same appearance in STM and can likely be explained in the same way.[26] The model by Švec et al. consists

https://doi.org/10.1021/acsami.4c05137
ACS Appl. Mater. Interfaces 2024, 16, 27481–27489

of Si atoms incorporated into the Pt lattice, forming two $PtSi_3$ tetramers, each with a central Pt atom per unit cell. One tetramer sits on top of a Pt atom in the second layer, while the other one sits above a hollow site, resulting in the hexagonally arranged protrusions and depressions observed in STM images.

In the case of Pt(111), no fully closed 2D silica film has been reported to date. The oxygen affinity of the metal was found to be the decisive criterion for the film structure, where substrates with high heats of dissociative oxygen adsorption favor crystalline monolayer films, while a lower heat of adsorption favors vitreous bilayers; only a minor influence was attributed to the lattice match.[20] Hence, we chose Rh as an additional substrate since its heat of dissociative oxygen adsorption (−182 kJ mol^{-1}) lies between the values for Ru (−220 kJ mol^{-1}) and Pt (−133 kJ mol^{-1}).[27] Additionally, the 2.69 Å lattice constant of Rh(111)[28] results in a better (factor-of-two) lattice match with the calculated periodicity of a free-standing, crystalline SiO_2 bilayer structure (5.30 Å)[13,29] than is obtained for Ru(0001) (2.71 Å)[30] or Pt(111) (2.77 Å).[31] Altman et al.[32] recently stated that the lattice mismatch and oxygen affinity of Rh(111) do not follow the same trend as other investigated metal substrates, thus making it highly interesting to study in order to disentangle these two influencing factors.

Here, we use STM, XPS, and low energy electron diffraction (LEED) to investigate the growth of 2D silica on Pt(111) and Rh(111), characterize the different resulting structures on these metals, and study the stability of the films under reducing conditions in CO at near-ambient pressure (NAP) as well as at high temperatures in ultrahigh vacuum (UHV). Furthermore, we discuss the possible influence of an intermixing of Si with the metal substrate at the 2D silica/Pt(111) interface on the film structure.

RESULTS

First, we look at the preparation of 2D silica on Rh(111). We prepared the film by deposition of 6 Å Si (2 ML Si) in an oxygen atmosphere of 1.5×10^{-6} mbar O_2, holding the Rh(111) crystal at 165 K. Subsequently, we annealed the sample at 1200 K in 5.0×10^{-6} mbar O_2 for 5 min. Figure 1a shows an STM image of the resulting silica film with a nearly complete coverage of the sample with 2D silica of different morphologies coexisting and the presence of holes. Note that we do not find any significant bias-dependent contrast changes. Higher magnification of the same sample (Figure 1b) reveals that the majority of the surface is covered with a vitreous film that also shows crystalline domains (hexagonal pattern) and coexists with a distinct "zigzag" structure (appearing as lower-lying) that also has been reported for Ru(0001) and Pt(111).[33,34] We also observed this slightly oxygen-enriched zigzag polymorph ($SiO_{2.17}$ compared to SiO_2 for bilayer silica) in smaller quantities on Pt(111) (see Figure S1, Supporting Information) but only for annealing times $t \geq 30$ min in 5.0×10^{-6} mbar oxygen. We attribute the more facile formation on Rh to its higher oxygen affinity compared to Pt. Monitoring the growth of silica on Rh(111) via XPS indicates a complex growth mechanism, with the underlying Rh(111) being more or less oxidized depending on the temperature. After deposition, the Si 2p signal has a peak at a binding energy of 102.8 eV (Figure 1c), likely due to oxidation during the initial evaporation process or at the Rh(111) surface, which is known to adsorb oxygen at room temperature.[35−37] Monitoring the signal in situ during annealing first shows a shift to lower binding energies up to 604 K before shifting back to higher binding energies at even higher temperatures. The O 1s spectra (Figure S2a, Supporting Information) show the same shifting behavior at the corresponding temperatures (Table S1, Supporting Information) and exhibit an additional shoulder at lower binding energies that evolves proportional to the energy shift, i.e., the lower the binding energy of the O 1s and Si 2p peaks, the more intense the shoulder. This is in good agreement with a previous study of 2D silica on Ru(0001), in which this low binding energy shoulder was assigned to interfacial oxygen adsorbed at the Ru(0001) surface, which correlates with lower binding energies of both the Si 2p and the O 1s signals.[22] Correspondingly, we interpret our results as showing the different amounts of interfacial oxygen absorbed on Rh(111) during the film formation. For the final film annealed to a temperature of 938 K, the Si 2p signal is at 102.9 eV with a full width at half-maximum (FWHM) of ∼1.65 eV, which is in good agreement with reported binding energy values for Pt(111)[20] (102.8 eV) and Ru(0001)[10,22] (102.5 eV).

When changing the substrate from Rh(111) to Pt(111) while keeping the synthesis procedure for the 2D silica the same, the film appears much more homogeneous in the STM (see Figure 1d,e), exhibiting only the vitreous bilayer as reported by Yu et al.[20] An amorphous network of different pore sizes spans the surface and shows a slight corrugation, as well as very few defects appearing as bright blobs, which we interpret as third layer species. However, in contrast to the previous reports, we could achieve a film that is free of holes across wide terraces, which we attribute to the deposition of silicon in excess and short oxygen annealing time. For longer annealing times in the same atmosphere, the resulting film is structurally similar, but some holes appear (see Figure S3b,c, Supporting Information).

Further insight into the growth and subsequent destabilization of the film is provided by XPS data acquired during annealing (see Figures 1f and S2b). In the Si 2p spectrum after deposition, the main signal appears at 100.6 eV, together with a relatively strong shoulder at 99.8 eV and a small peak at around 102.4 eV. These species are not well-defined after deposition at room temperature but likely correspond to silica species that are only weakly oxidized on the preoxidized Pt surface and/or due to interaction with gas-phase oxygen. Upon heating to 787 K, the main signal shifts by about 0.2 eV to higher binding energy, the low binding energy shoulder decreases in intensity, and the high binding energy species increases. At 943 K, all Si species previously at 100.6 eV and below were converted to the one at 102.4 eV with a FWHM of ∼1.8 eV, which we interpret as the entire film being fully oxidized.

To gain a deeper understanding of the growth mechanism of 2D silica on Pt(111), we also deposited 1/3 of the amount used in the previous syntheses and chose a lower annealing temperature of 850 K. The resulting silica (Figure 1g) shows no large islands but rather a dendritic network across several terraces, suggesting an even spreading already at lower temperatures. In this case, additional annealing of 90 min at 850 K, 35 min at 1000 K, and 5 min at 1200 K in the synthesis atmosphere does not change the topography (Figure 1h). In the initial XPS spectrum after deposition (blue line in Figure 1i), the signal is similar in binding energy (main peak ∼100.6 eV) to the one observed for the full surface covering 2D silica. However, at this lower coverage, the signal shifts already at 450 K to a higher binding energy of ∼101.8 eV and appears as a single peak. Finally, at 1070 K, the peak appears at a binding

https://doi.org/10.1021/acsami.4c05137
ACS Appl. Mater. Interfaces 2024, 16, 27481−27489

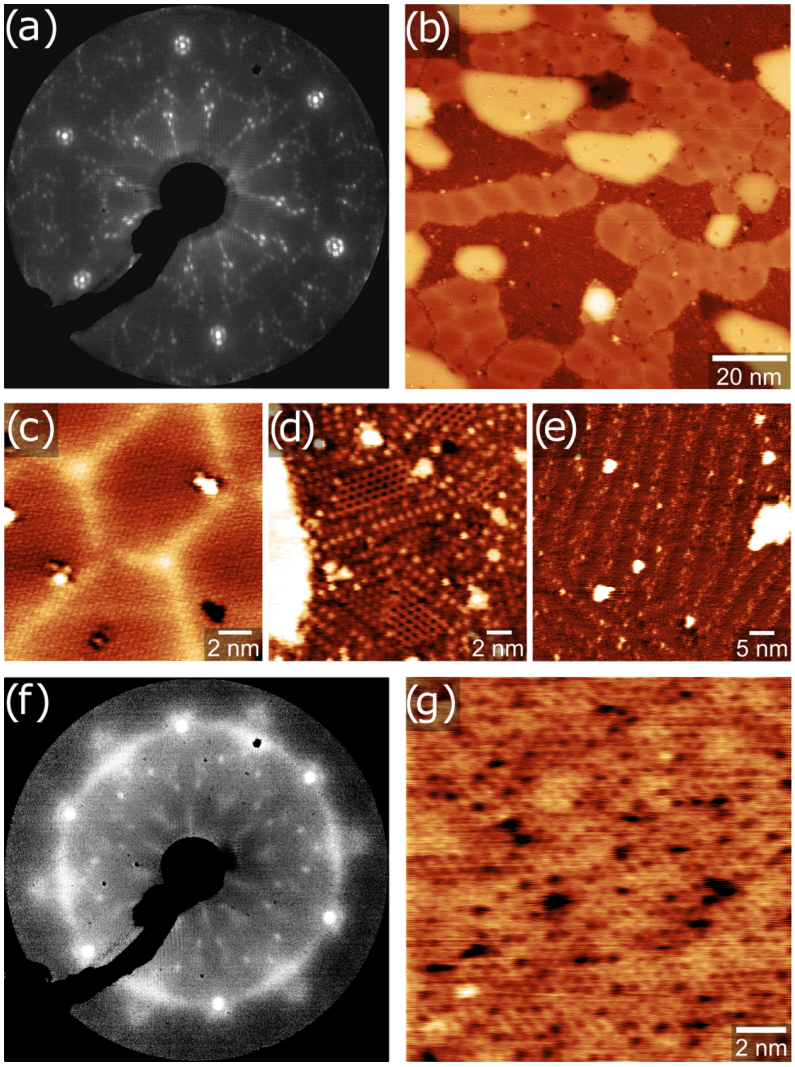

Figure 2. (a) LEED and (b–e) STM images of a Pt surface silicide and (f, g) respective data for the resulting silica film after oxidation. STM images were acquired in UHV at room temperature, with the following tunneling parameters: (b) I_t = 0.51 nA, V_b = 0.88 V, 100 × 100 nm^2, (c) I_t = 0.47 nA, V_b = 0.79 V, 15 × 15 nm^2, (d) I_t = 0.47 nA, V_b = 0.79 V, 20 × 20 nm^2, (e) I_t = 1.33 nA, V_b = 0.84 V, 50 × 50 nm^2, and (g) I_t = 0.39 nA, V_b = 0.35 V, 15 × 15 nm^2. LEED energies: (a) 110 eV and (f) 120 eV.

energy of 102.4 eV with a FWHM of again ∼1.8 eV. Thus, the final chemical state after prolonged annealing is the same as for higher coverage silica films. It is interesting to note, however, that before this final data point (obtained by prolonged high-temperature annealing up to 976 K), the main Si 2p component observed for the submonolayer film is found at significantly higher binding energy (∼101.8 eV) than the highest Si 2p peak of the closed film (100.6 eV) and instead appears closer to the shoulder at 102.4 eV. Considering that the shift between 976 K (pink line in Figure 1i) and 1070 K (gray line in Figure 1i) is likely caused by the desorption of interfacial oxygen,[22] this might indicate that full oxidation is achieved at much lower temperatures for the low Si coverage (see also O 1s spectra in Figure S2c, Supporting Information). As discussed below, we interpret this coexistence of multiple Si 2p components throughout the annealing process as evidence for a platinum silicide or silicate phase that is present below the silica bilayer when silicon is deposited in excess.

Since the measurements were performed in different setups, the STM images do not directly correspond to the XPS spectra in Figure 1, and annealing times during film synthesis differed somewhat due to the signal monitoring in XPS. To address this discrepancy, we also performed Auger electron spectroscopy (AES) of the fully closed 2D silica directly after the STM measurements (Figure S3a, Supporting Information). With a kinetic energy of ∼82 eV, the main Si peak of the closed film shown in Figure 1d,e (orange line in Figure S3a) is located between literature values for elemental silicon (92 eV) and bulk silicon dioxide (76 eV).[38] As mentioned above, further annealing steps at 1200 K (green line) and 1300 K (red line) in 5.0 × 10^{-6} mbar, as well as 1000 K in UHV (purple line), caused holes to appear in the film (Figure S3b,c), while the AES signal shifts to lower kinetic energies, in agreement with the XPS results.

To elucidate the nature of a potential interfacial silicide and to investigate whether 2D silica can be formed via direct oxidation of such a phase, we deposited the same Si amount as used to obtain the fully closed 2D silica on bare Pt(111) and annealed in UHV (instead of in an oxygen atmosphere) at 800 K for 10 min. In the STM, we can observe a variety of different

https://doi.org/10.1021/acsami.4c05137
ACS Appl. Mater. Interfaces 2024, 16, 27481−27489

coexisting surface structures (Figure 2b–e) that are also reflected in the complexity of the resulting LEED pattern (Figure 2a). The latter one appears very similar to the LEED images for a Si/Pt ratio of 0.43 and 0.30 reported by Nashner et al., which were formed when transitioning from a $(\sqrt{7} \times \sqrt{7})R19.1°$ to the $(\sqrt{19} \times \sqrt{19})R23.4°$ surface silicide.[24] With additional annealing in 5.0×10^{-6} mbar oxygen at 1200 K for 5 min, we again obtained a 2D silica film with the same appearance in STM (Figure 2g) as for the synthesis starting from bare Pt(111). However, a clear difference is seen in LEED: When 2D silica is grown by immediately annealing in oxygen after deposition (as in Figure 1d,e), the LEED pattern (Figure S4, Supporting Information) shows only the spots corresponding to the hexagonal Pt(111) substrate and a diffuse ring, indicating different ring sizes and orientations in the 2D silica. In contrast, when the silica film is grown from the silicide phase, LEED shows numerous additional spots, indicating an ordered superstructure (Figure 2f). Since the silica layer observed in STM (Figure 2g) shows no particular ordering, these superstructure spots must reflect a subsurface phase, which indicates that the silicide is still present underneath the SiO_2 bilayer. As the same amount of silicon was deposited in both cases, we can assume that an interfacial silicide is also present underneath the films seen in Figure 1d,e but was not ordered sufficiently to be visible in LEED.

In order to see if the 2D silica on Pt(111) is suitable as a support material for model catalysis studies under NAP conditions, we conducted STM measurements in a CO atmosphere at room temperature. An in situ NAP-STM image under 0.8 mbar CO is shown in Figure 3a. The film was

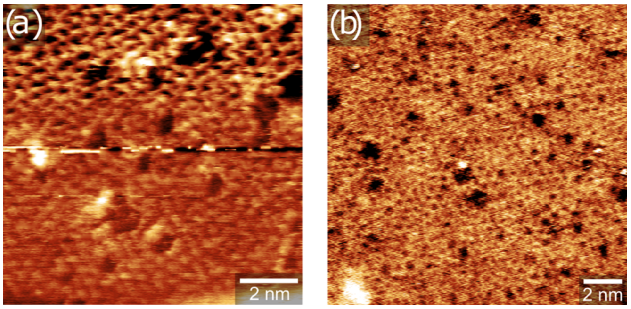

Figure 3. Room temperature STM images of 2D silica on Pt(111) (a) in 0.8 mbar CO and (b) under UHV after pumping back down. Tunneling parameters: (a) I_t = 0.86 nA, V_b = 0.50 V, 10 × 10 nm^2 and (b) I_t = 0.34 nA, V_b = 0.32 V, 15 × 15 nm^2.

prepared in the same manner as the one shown in Figure 1d,e. While the contrast is somewhat blurred in the CO atmosphere compared to UHV (Figure 1e) possibly due to interaction of the STM tip with the gas phase, the vitreous SiO_2 network is still clearly visible. Figure 3b shows an image of the same sample that had been exposed to the CO atmosphere for 2.5 h and pumped back down to UHV. Again, no major changes are apparent with respect to the as-prepared film.

Further to being stable in gas atmospheres, an inert model catalyst support should also be stable at elevated temperatures. As mentioned, a shift in binding energy of the Si 2p signal of up to 0.8 eV occurred when converting "O-rich" into "O-poor" 2D silica on Ru(0001) at annealing temperatures of up to 1150 K.[22] Similarly, we observed only a very small shift of 0.1 eV upon annealing the full coverage film on Pt(111) at 960 K (Figure S5, Supporting Information). However, a drastically different behavior is observed on Rh(111). Upon annealing at 946 K, the Si 2p signal appeared as a sharp doublet at 99.5 and 100.1 eV with a significant decrease in total signal intensity (Figure 4d). This binding energy corresponds well to different

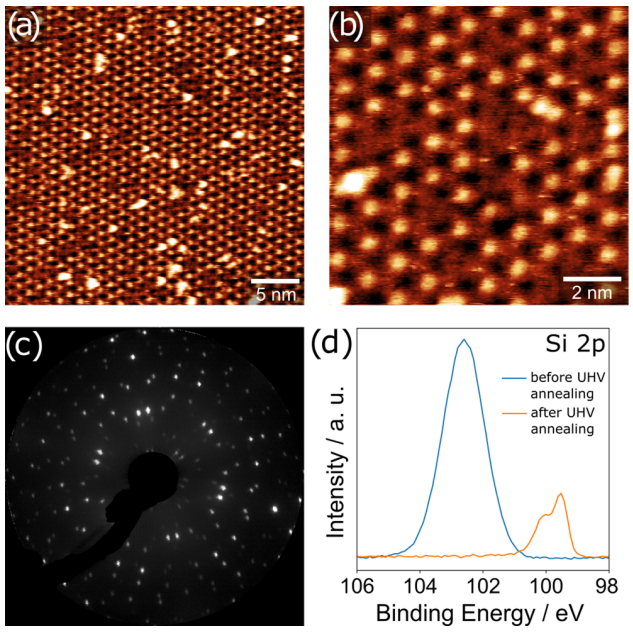

Figure 4. STM images, LEED, and XPS spectra of reduced silica on Rh(111). (a) STM image of the Rh surface silicide resulting from the reduction of 2D silica on Rh(111) via UHV annealing at 1200 K for 30 min. (b) Higher magnification STM image of the same surface. (c) LEED image (103 eV) of the surface silicide exhibiting a $(\sqrt{19} \times \sqrt{19})R23.4°$ superstructure with respect to Rh(111). (d) Si 2p region of 2D silica (blue, before UHV annealing) and the surface silicide (orange, after UHV annealing at 946 K). Tunneling parameters: (a) I_t = 0.22 nA, V_b = 2.12 V, 30 × 30 nm^2 and (b) I_t = 0.12 nA, V_b = 1.27 V, 10 × 10 nm^2. XPS parameters: excitation energy of 300 eV.

bulk Rh silicides in the literature (99.5–99.7 eV),[39,43] as well as surface PtSi.[40] Additionally, the O 1s signal is completely lost (Figure S6, Supporting Information). STM images acquired after annealing an SiO_2 film like the one shown in Figure 1a,b in UHV at 1200 K for 30 min are shown in Figure 4a,b. There are no traces of any of the 2D silica phases left, and instead, we observe an ordered hexagonal structure of protrusions with a lattice constant of ∼11 Å. The corresponding LEED image (Figure 4c) shows the same $(\sqrt{19} \times \sqrt{19})R23.4°$ reconstruction as reported for surface-segregated Si on Pt(111).[23] Overall, both STM and LEED images, as well as the binding energy of the Si 2p peak, are consistent with surface silicides reported on Pt(111)[23,26] and could be explained with the model proposed by Švec et al.[26]

To test if the reduction of 2D silica on Rh(111) is reversible, we heated the surface silicide again in an oxygen atmosphere at 5×10^{-6} mbar. In the resulting XPS spectra (Figure 5a,b), an immediate change occurs after O_2 exposure already at RT. Comparing the Si 2p spectrum before exposure (blue line in Figure 5a) with the one after exposure (orange line), the silicide signal decreases and an additional small signal appears at a binding energy of ∼102.2 eV. Simultaneously, an O 1s signal appears at 531.4 eV. It seems likely that these signals are caused by oxygen coordinating or binding to the Si atoms on the surface. Subsequently, we monitored the oxidation of the

https://doi.org/10.1021/acsami.4c05137
ACS Appl. Mater. Interfaces 2024, 16, 27481–27489

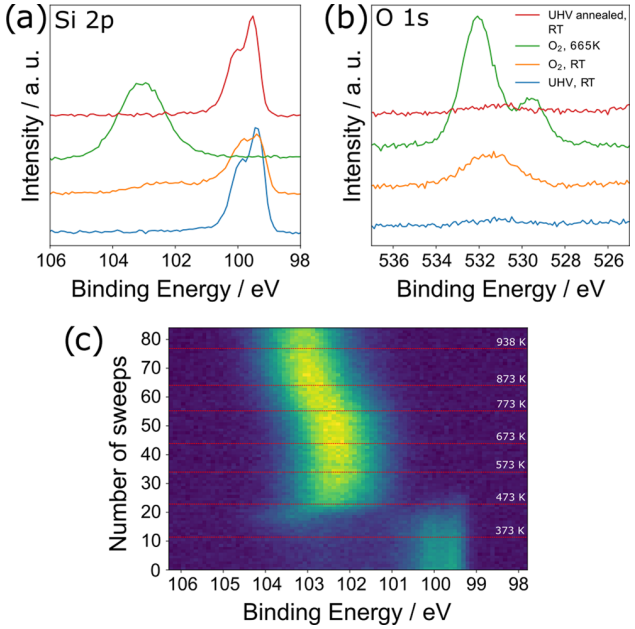

Figure 5. XPS spectra of the oxidation of the Rh surface silicide. (a, b) Si 2p (excitation energy 300 eV) and O 1s (excitation energy 650 eV) spectra of the surface silicide directly after 2D silica reduction (blue), partial oxidation after dosing 5×10^{-6} mbar oxygen (orange), fully reoxidized silica after heating to 938 K in oxygen (green), and surface silicide after renewed reduction at 938 K in UHV and cooling to RT (red). (c) Time series Si 2p spectrum of the oxidation of the Rh surface silicide, beginning at RT in 5×10^{-6} mbar oxygen. Sweep N = 0 corresponds to the orange line, and N = 84 to the green line in (a, b); each sweep takes 46 s. 100 K temperature steps and the maximum temperature reached are indicated by red lines.

surface silicide by continuously measuring the Si 2p signal while heating (Figure 5c). Starting at sweep 9, which corresponds to a temperature of ~345 K, the silicide signal progressively decreases while the signal at higher binding energy increases. At about sweep 30 (534 K), the silicide signal is completely gone, and the intensity of the high binding energy signal is fully developed. Further heating causes only a small shift to higher binding energy due to the partial desorption of oxygen from Rh below the SiO_2 film, consistent with the spectra in Figure 1c. The green lines in Figure 5a,b show high-resolution spectra of Si 2p and O 1s, respectively, at the final temperature of 665 K. The Si 2p signal again appears at the binding energy of the fully oxidized Si at 102.9 eV. The O 1s signal appears to be split into two peaks, the one at higher binding energy corresponding to Si−O and the one at lower binding energy corresponding to Rh−O.[22] However, the much higher signal intensity observed before initial reduction (blue curve in Figure 4d) is clearly not recovered by the reoxidation.

Finally, we tested how fast the reduction of the film occurs by closing the oxygen valve at 665 K while monitoring the Si 2p signal (Figure S7, Supporting Information). Within ~5 min (7 sweeps, 46 s each), the silica is again completely transformed to a silicide. The Si 2p and O 1s high-resolution spectra after cooling down are shown in Figure 5a,b (red curves).

DISCUSSION

Our STM results demonstrate the successful formation of a fully closed 2D silica film on Pt(111). We attribute this achievement to the brief oxygen annealing period of only 5 min following silicon deposition, coupled with the use of silicon in excess. There are multiple indications that this excess Si is still present below our silica film: First, when comparing XPS data of high and low Si loading (Figure 1f,i), the submonolayer film shows only one component in the Si 2p region while multiple peaks are found for the closed films. Notably, when depositing Si in excess, full oxidation is only achieved after prolonged annealing at high temperatures, which in the STM always leads to the formation of holes in the film. We have also shown that a silica film can be grown directly from a surface silicide, and LEED (Figure 2f) shows that an ordered phase persists below the film under these conditions. This is likely the ordered silicide (Si_xPt), although XPS suggests at least partial oxidation to an interfacial silicate (Si_xO_yPt). Interestingly, no superstructure spots are found in LEED of directly synthesized films (Figure S4). It is possible that when annealing is performed in oxygen directly, oxidic precursor states of the silica film prevent the surface silicide from ordering to the same degree as when UHV annealing is performed (Figure 2a−e).

We propose that this interface layer functions as a crucial "buffer layer", which is the decisive factor in stabilizing the 2D silica, preventing the formation of any undesirable holes in the film. The resulting 2D silica structure is stable in a CO atmosphere of up to 0.8 mbar. However, the silicide/silicate buffer layer is unstable when subjected to high temperatures (>1000 K) in UHV or oxygen, which we attribute to its reductive or oxidative degradation, respectively. It seems plausible that during reductive degradation, the surplus silicon initially forms a surface silicide up to a certain threshold but ultimately undergoes diffusion into the Pt bulk, given silicon's notable mobility in this temperature range.[23,41,42] On the contrary, if the interface layer undergoes further oxidation, there is the possibility of additional silicon being incorporated into the 2D silica. This incorporation may result in subtle surface corrugations due to minor buckling, potentially culminating in the out-of-plane growth of silica, as indicated by the increased roughness observed when attempting to image the surface.

Switching the underlying substrate to Rh(111), it is evident that 2D silica on Rh(111) aligns with the crystallinity trend concerning the heat of dissociative oxygen adsorption, positioned between Ru(0001)—where both crystalline films and zigzag structures are viable—and Pt(111), where 2D silica exclusively adopts an amorphous structure. In this regard, Rh(111) behaves close to Ru(0001), as at least some crystalline areas can be observed in Figure 1a,b, and better ordering could likely be achieved by tuning the annealing temperature and cooling ramp. However, unlike on Ru or Pt, the thermal reaction from 2D silica to a surface alloy/silicide is extremely facile on Rh, which destabilizes the silica film despite the better lattice match.

Unlike earlier studies on 2D silica on Ru(0001), we were not able to find a preparation that yields a fully closed silica film on Rh(111). In this respect, Rh is more similar to previous studies on Pt(111) but with the difference that the formation of a stabilizing buffer layer is precluded. This limitation seems to arise from the prompt oxidation of the deposited Si on the Rh(111) surface, as deduced from the XPS data (Figure 1c). Also unlike Ru and Pt, full reduction of the 2D silica is possible on Rh(111) by relatively mild UHV annealing, resulting in the formation of a $(\sqrt{19} \times \sqrt{19})R23.4°$ surface silicide like the one reported on Pt(111).[23,26] In a similar vein, Labich et al.

https://doi.org/10.1021/acsami.4c05137
ACS Appl. Mater. Interfaces 2024, 16, 27481−27489

reported the reaction of Rh clusters deposited on a 90 Å thick SiO_2 film on Mo-foil, forming the rhodium silicide Rh_3Si upon heating to 873 K in UHV, emerging at a binding energy of 100.3 eV in XPS.[43] Because of the much higher heat of formation of SiO_2 compared to the metal silicide, the proposed reaction mechanism occurs via oxygen transfer to Rh, followed by thermal desorption of oxygen, rather than via the formation of the thermodynamically less favorable metal oxide. Therefore, we ascribe rhodium's potential to cleave Si−O bonds, coupled with oxygen's complete desorption from the surface as evidenced in XPS (Figures 4d and S6), as the key factors driving the formation of the pure $(\sqrt{19} \times \sqrt{19})R23.4°$ surface silicide.

This reduction and the subsequent reoxidation of the surface silicide on Rh(111) are chemically reversible, but the large signal loss resulting from the initial reduction is irreversible. This is likely due to the diffusion of Si into the bulk, which is known to be fast in this temperature regime as the two elements are miscible.[44,45] Volatile SiO species that can then desorb from the surface may also form during film degradation, as shown for native silica.[46−48] Note that we also tried to measure STM of the resulting reoxidized silica which turned out to be challenging, indicating that the structure is rather growing three-dimensionally instead of forming flat islands of lower coverage.

Finally, it is interesting to reiterate at this point that the $(\sqrt{19} \times \sqrt{19})R23.4°$ silicide on Rh(111) seems virtually identical to the one on Pt(111), and that similar STM images have previously been interpreted as silicene phases on Ag(111).[25] Fundamentally, such a decoupled phase seems chemically unlikely on Pt and even more so on Rh, where silicide formation is facile. As noted already in the Introduction section, an extensive and convincing argument against a silicene phase on Pt(111) has already been presented by Švec et al.[26] More recently, a study by Küchle et al. has presented evidence that even on Ag(111), where the topmost layer does seem to consist of a 2D arrangement of silicon atoms, this arrangement is supported on an Ag/Si layer acting as a buffer layer.[49] While the chemistry of the Pt silicide stabilizing a closed silica film is clearly quite different, this nicely highlights the importance that mixed interfacial layers may have on the stability of thin films at surfaces.

CONCLUSIONS

We have shown that fully closed 2D silica films can be obtained on Pt(111) when they are stabilized by an interfacial silicide or silicate buffer layer. The films can also be directly synthesized from a surface silicide precursor and show high stability against relatively high pressures of CO. However, the stabilization remains challenging for both oxidative and reductive conditions at elevated temperatures. While the closed film is thus not stable enough to serve as a support in model catalysis investigations at near-ambient pressures and elevated temperatures, the film with holes exhibits high stability, in line with the reports for Ru(0001) and Pt(111).

On Rh(111), we have obtained films with mixed morphologies, specifically vitreous, crystalline, and "zigzag" structures, as reported previously on other substrates. In stark contrast to previously investigated metal substrates, however, 2D silica on Rh(111) can be fully reduced by UHV annealing, forming a surface silicide with a $(\sqrt{19} \times \sqrt{19})R23.4°$ periodicity. While recovery of the films is hampered by the fact that a large portion of the Si is lost, either to the Rh bulk or to the gas phase as SiO, the initial reduction is chemically fully reversible.

EXPERIMENTAL SECTION

Pt(111) single crystal samples (from SPL for STM and from Mateck for XPS measurements) were prepared by several cycles of sputtering (Ar^+, 5×10^{-5} mbar, 1.0 keV, 15 min) and annealing (1200 K, 1 min, followed by 800 K, 15 min, both in $p(O_2) = 1 \times 10^{-7}$ mbar). Rh(111) single crystal samples (from SPL) were prepared by several cycles of sputtering (Ar^+, 3×10^{-5} mbar, 1.0 keV, 15 min) and annealing (1200 K, 15 min in $p(O_2) = 5 \times 10^{-7}$ mbar with the last cycle in UHV). The samples were heated using an e-beam heater. The temperature was measured with a type K thermocouple attached to the backside of the crystal.

For the STM and LEED experiments, Si deposition was carried out with an EBE-1 evaporator by SPECS with a Si rod from Goodfellow (diameter: 2.0 mm, purity: 99.999%, crystalline), monitored with a quartz crystal microbalance by OmniVac. In the deposition procedure, we monitored the signal of the microbalance in an oxygen atmosphere until a stable deposition rate was reached. Then, the microbalance was removed, and the sample was placed in the same position to deposit the desired amount of silicon. Note that we used the density of elemental silicon for the rate monitoring, which could result in a systematic error, considering that the deposit is at least partially oxidized Si. STM measurements were performed with an SPM Aarhus 150 NAP-STM by SPECS in constant current mode with an electrochemically etched tungsten tip. Bias voltages (V_b) refer to the sample voltage with respect to the tip. Image correction was carried out with the SPM software Gwyddion using the plane correction and row alignment tools.[50] LEED images were acquired with an ErLEED 150 by SPECS. All AES measurements were performed with a DESA 150 by Staib Instruments with a primary electron energy of 5 keV.

All XPS measurements were conducted at beamline 9.3.2 of the Advanced Light Source at the Lawrence Berkeley National Laboratory. Here, the same Si rod was used for deposition with an EBE-4 evaporator by SPECS. All O 1s spectra were measured with a beam energy of 650 eV and were referenced to the binding energy of the Pt 4f or Rh 3d peak, respectively. The Si 2p spectra were obtained with a beam energy of 300 eV and referenced to the binding energy of the Pt 4f or Rh 4p peak, giving us a similar surface sensitivity for both O 1s and Si 2p core levels. The energy resolution was ∼0.2 eV throughout the available energy range. The spot size was ∼1 mm^2 on the sample, i.e., much larger than the area measured in STM. Probing different areas of the sample with AES, LEED, and XPS yielded perfectly reproducible results, indicating that the sample is homogeneously covered. For heating, a pyrolytic boron nitride heater was used; the temperature was monitored with a type K thermocouple at the front-side of the single crystal.

ASSOCIATED CONTENT

Supporting Information

The Supporting Information is available free of charge at https://pubs.acs.org/doi/10.1021/acsami.4c05137.

Additional figures: STM images showing the $SiO_{2.17}$ zigzag phase; O 1s spectra acquired during SiO_2 film synthesis; AES spectra of the SiO_2 film on Pt(111) as prepared and after different annealing steps with corresponding STM images; LEED image of the SiO_2 film on Pt(111); Si 2p XPS spectra of the SiO_2 film on Pt(111) before and after annealing in UHV; O 1s XPS spectra of the SiO_2 film on Rh(111) before and after annealing in UHV; Si 2p XPS spectra of the SiO_2 film reduction on Rh(111); and table listing binding energies of Si 2p and O 1s during SiO_2 film synthesis at different temperatures (PDF)

https://doi.org/10.1021/acsami.4c05137
ACS Appl. Mater. Interfaces 2024, 16, 27481−27489

AUTHOR INFORMATION

Corresponding Author

Barbara A. J. Lechner − *Functional Nanomaterials Group and Catalysis Research Center, Department of Chemistry, TUM School of Natural Sciences, Technical University of Munich, 85748 Garching, Germany; Institute for Advanced Study, Technical University of Munich, 85748 Garching, Germany;* orcid.org/0000-0001-9974-1738; Email: bajlechner@tum.de

Authors

Matthias Krinninger − *Functional Nanomaterials Group and Catalysis Research Center, Department of Chemistry, TUM School of Natural Sciences, Technical University of Munich, 85748 Garching, Germany;* orcid.org/0000-0002-8357-9323

Florian Kraushofer − *Functional Nanomaterials Group and Catalysis Research Center, Department of Chemistry, TUM School of Natural Sciences, Technical University of Munich, 85748 Garching, Germany;* orcid.org/0000-0003-1314-9149

Nils B. Refvik − *Department of Physics, University of Alberta, Edmonton, Alberta T6G 2E1, Canada*

Monika Blum − *Chemical Sciences Division, Lawrence Berkeley National Laboratory, Berkeley, California 94720, United States; Advanced Light Source, Lawrence Berkeley National Laboratory, Berkeley, California 94720, United States;* orcid.org/0000-0002-2918-9092

Complete contact information is available at: https://pubs.acs.org/10.1021/acsami.4c05137

Author Contributions

M.K. and F.K. conducted all experiments and analyzed the data. N.B.R. aided in the STM and AES measurements. M.B. supported the XPS experiments at the Advanced Light Source. B.A.J.L., M.K., and F.K. planned the experiments and wrote the first version of the manuscript. All authors have contributed to the manuscript and given approval to the final version.

Notes

The authors declare no competing financial interest.

ACKNOWLEDGMENTS

This work was funded by the Deutsche Forschungsgemeinschaft (DFG, German Research Foundation) under Germany's Excellence Strategy EXC 2089/1-390776260 and through the project CRC1441 (project number 426888090, subproject A2), as well as by the European Research Council (ERC) under the European Union's Horizon 2020 research and innovation program (grant agreement no. 850764). This work used resources of the Advanced Light Source, a user facility supported by the Office of Science of the U.S. DOE under Contract DE-AC02- 05CH11231. N.B.R. gratefully acknowledges funding from the Alberta/Technical University of Munich International Graduate School for Hybrid Functional Materials (ATUMS). B.A.J.L. gratefully acknowledges financial support from the Young Academy of the Bavarian Academy of Sciences and Humanities.

ABBREVIATIONS

STM, scanning tunneling microscopy; XPS, X-ray photoelectron spectroscopy; LEED, low energy electron diffraction; UHV, ultrahigh vacuum; NAP, near-ambient pressure; FWHM, full width at half-maximum

REFERENCES

(1) Ertl, G. Reactions at Surfaces: From Atoms to Complexity (Nobel Lecture). *Angew. Chem., Int. Ed.* **2008**, *47* (19), 3524−3535.

(2) Crampton, A. S.; Rötzer, M. D.; Schweinberger, F. F.; Yoon, B.; Landman, U.; Heiz, U. Controlling Ethylene Hydrogenation Reactivity on Pt13Clusters by Varying the Stoichiometry of the Amorphous Silica Support. *Angew. Chem., Int. Ed.* **2016**, *55* (31), 8953−8957.

(3) Crampton, A. S.; Rotzer, M. D.; Landman, U.; Heiz, U. Can Support Acidity Predict Sub-Nanometer Catalyst Activity Trends? *ACS Catal.* **2017**, *7* (10), 6738−6744.

(4) Mcclure, S. M.; Lundwall, M.; Yang, F.; Zhou, Z.; Goodman, D. W. CO Oxidation on Rh/SiO2/Mo(112) Model Catalysts at Elevated Pressures. *J. Phys. Chem. C* **2009**, *113* (113), 9688−9697.

(5) Crampton, A. S.; Ridge, C. J.; Rötzer, M. D.; Zwaschka, G.; Braun, T.; D'Elia, V.; Basset, J. M.; Schweinberger, F. F.; Günther, S.; Heiz, U. Atomic Structure Control of Silica Thin Films on Pt(111). *J. Phys. Chem. C* **2015**, *119* (24), 13665−13669.

(6) Zhong, J. Q.; Freund, H. J. Two-Dimensional Ultrathin Silica Films. *Chem. Rev.* **2022**, *122* (13), 11172−11246.

(7) Altman, E. I. Two-Dimensional Silica from Model System to Applications. *Chem. Rev.* **2022**, *122* (13), 11169−11171.

(8) Schroeder, T.; Adelt, M.; Richter, B.; Naschitzki, M.; Bäumer, M.; Freund, H.-J. Epitaxial Growth Of SiO2 On Mo(112). *Surf. Rev. Lett.* **2000**, *07* (01n02), 7−14.

(9) Weissenrieder, J.; Kaya, S.; Lu, J. L.; Gao, H. J.; Shaikhutdinov, S.; Freund, H. J.; Sierka, M.; Todorova, T. K.; Sauer, J. Atomic Structure of a Thin Silica Film on a Mo(112) Substrate: A Two-Dimensional Network of SiO_4 Tetrahedra. *Phys. Rev. Lett.* **2005**, *95* (7), 076103-1−076103-4.

(10) Löffler, D.; Uhlrich, J. J.; Baron, M.; Yang, B.; Yu, X.; Lichtenstein, L.; Heinke, L.; Büchner, C.; Heyde, M.; Shaikhutdinov, S.; Freund, H. J.; Włodarczyk, R.; Sierka, M.; Sauer, J. Growth and Structure of Crystalline Silica Sheet on Ru(0001). *Phys. Rev. Lett.* **2010**, *105* (14), 2−5.

(11) Lichtenstein, L.; Heyde, M.; Freund, H. J. Atomic Arrangement in Two-Dimensional Silica: From Crystalline to Vitreous Structures. *J. Phys. Chem. C* **2012**, *116* (38), 20426−20432.

(12) Yang, B.; Kaden, W. E.; Yu, X.; Boscoboinik, J. A.; Martynova, Y.; Lichtenstein, L.; Heyde, M.; Sterrer, M.; Włodarczyk, R.; Sierka, M.; Sauer, J.; Shaikhutdinov, S.; Freund, H. J. Thin Silica Films on Ru(0001): Monolayer, Bilayer and Three-Dimensional Networks of [SiO 4] Tetrahedra. *Phys. Chem. Chem. Phys.* **2012**, *14* (32), 11344−11351.

(13) Altman, E. I.; Götzen, J.; Samudrala, N.; Schwarz, U. D. Growth and Characterization of Crystalline Silica Films on Pd(100). *J. Phys. Chem. C* **2013**, *117* (49), 26144−26155.

(14) Mark, L. O.; Chen, W.; Eads, C. N.; Lu, D.; Boscoboinik, J. A.; Stacchiola, D.; Medlin, J. W.; Tenney, S. A. Confinement Effects on Furfuryl Alcohol Reactions over Porous Bilayer Silica-Modified Pd(111). *J. Phys. Chem. C* **2020**, *124* (46), 25437−25446.

(15) Jhang, J. H.; Zhou, C.; Dagdeviren, O. E.; Hutchings, G. S.; Schwarz, U. D.; Altman, E. I. Growth of Two Dimensional Silica and Aluminosilicate Bilayers on Pd(111): From Incommensurate to Commensurate Crystalline. *Phys. Chem. Chem. Phys.* **2017**, *19* (21), 14001−14011.

(16) Hutchings, G. S.; Jhang, J. H.; Zhou, C.; Hynek, D.; Schwarz, U. D.; Altman, E. I. Epitaxial NixPd1-x (111) Alloy Substrates with Continuously Tunable Lattice Constants for 2D Materials Growth. *ACS Appl. Mater. Interfaces* **2017**, *9* (12), 11266−11271.

(17) Ben Romdhane, F.; Björkman, T.; Rodríguez-Manzo, J. A.; Cretu, O.; Krasheninnikov, A. V.; Banhart, F. In Situ Growth of Cellular Two-Dimensional Silicon Oxide on Metal Substrates. *ACS Nano* **2013**, *7* (6), 5175−5180.

(18) Huang, P. Y.; Kurasch, S.; Srivastava, A.; Skakalova, V.; Kotakoski, J.; Krasheninnikov, A. V.; Hovden, R.; Mao, Q.; Meyer, J.

C.; Smet, J.; Muller, D. A.; Kaiser, U. Imaging the Atoms in a Two-Dimensional Silica Glass on Graphene. *Microsc. Microanal.* **2012**, *18* (S2), 1496−1497.
(19) Huang, P. Y.; Kurasch, S.; Alden, J. S.; Shekhawat, A.; Alemi, A. A.; McEuen, P. L.; Sethna, J. P.; Kaiser, U.; Muller, D. A. Imaging Atomic Rearrangements in Two-Dimensional Silica Glass: Watching Silica's Dance. *Science* **2013**, *342* (6155), 224−227.
(20) Yu, X.; Yang, B.; Anibal Boscoboinik, J.; Shaikhutdinov, S.; Freund, H. J. Support Effects on the Atomic Structure of Ultrathin Silica Films on Metals. *Appl. Phys. Lett.* **2012**, *100* (15), 151608.
(21) Sierka, M.; Todorova, T. K.; Kaya, S.; Stacchiola, D.; Weissenrieder, J.; Lu, J.; Gao, H.; Shaikhutdinov, S.; Freund, H. J.; Sauer, J. Interplay between Theory and Experiment in the Quest for Silica with Reduced Dimensionality Grown on a Mo(112) Surface. *Chem. Phys. Lett.* **2006**, *424* (1−3), 115−119.
(22) Włodarczyk, R.; Sierka, M.; Sauer, J.; Löffler, D.; Uhlrich, J. J.; Yu, X.; Yang, B.; Groot, I. M. N.; Shaikhutdinov, S.; Freund, H. J. Tuning the Electronic Structure of Ultrathin Crystalline Silica Films on Ru(0001). *Phys. Rev. B: Condens. Matter Mater. Phys.* **2012**, *85* (8), 085403.
(23) Diebold, U.; Zhang, L.; Anderson, J. F.; Mrozek, P. Surface Segregation of Silicon in Platinum(111). *J. Vac. Sci. Technol., A* **1996**, *14* (3), 1679−1683.
(24) Nashner, M. S.; Bondos, J. C.; Hosteller, M. J.; Gewirth, A. A.; Nuzzo, R. G. Chemisorption Properties and Structural Evolution of Pt-Si Intermetallic Thin Films Prepared by the Activated Adsorption of SiH4 on Pt(111). *J. Phys. Chem. B* **1998**, *102* (32), 6202−6211.
(25) Feng, B.; Ding, Z.; Meng, S.; Yao, Y.; He, X.; Cheng, P.; Chen, L.; Wu, K. Evidence of Silicene in Honeycomb Structures of Silicon on Ag(111). *Nano Lett.* **2012**, *12* (7), 3507−3511.
(26) Švec, M.; Hapala, P.; OndráAek, M.; Merino, P.; Blanco-Rey, M.; Mutombo, P.; VondráAek, M.; Polyak, Y.; Cháb, V.; Martín Gago, J. A.; Jelínek, P. Silicene versus Two-Dimensional Ordered Silicide: Atomic and Electronic Structure of Si- (19 × 19)R23.4°/Pt(111). *Phys. Rev. B: Condens. Matter Mater. Phys.* **2014**, *89* (20), 201412.
(27) Rao, C. N. R.; Vishnu Kamath, P.; Yashonath, S. Molecularly Adsorbed Oxygen on Metals: Electron Spectroscopic Studies. *Chem. Phys. Lett.* **1982**, *88* (1), 13−16.
(28) Gustafson, J.; Mikkelsen, A.; Borg, M.; Lundgren, E.; Köhler, L.; Kresse, G.; Schmid, M.; Varga, P.; Yuhara, J.; Torrelles, X.; Quirós, C.; Andersen, J. N. Self-Limited Growth of a Thin Oxide Layer on Rh(111). *Phys. Rev. Lett.* **2004**, *92* (12), 126102.
(29) Büchner, C.; Heyde, M. Two-Dimensional Silica Opens New Perspectives. *Prog. Surf. Sci.* **2017**, *92* (4), 341−374.
(30) Marchini, S.; Günther, S.; Wintterlin, J. Scanning Tunneling Microscopy of Graphene on Ru(0001). *Phys. Rev. B: Condens. Matter Mater. Phys.* **2007**, *76* (7), 075429.
(31) Ritter, M.; Ranke, W.; Weiss, W. Growth and Structure of Ultrathin FeO Films on Pt(111) Studied by STM and LEED. *Phys. Rev. B: Condens. Matter Mater. Phys.* **1998**, *57* (12), 7240−7251.
(32) Altman, E. I.; Dementyev, P. Atomic Layer Deposition Brings Applications of Two - Dimensional Silica to the Fore. *Catal. Lett.* **2024**, *154*, 1359−1374.
(33) Kuhness, D.; Yang, H. J.; Klemm, H. W.; Prieto, M.; Peschel, G.; Fuhrich, A.; Menzel, D.; Schmidt, T.; Yu, X.; Shaikhutdinov, S.; Lewandowski, A.; Heyde, M.; Kelemen, A.; Włodarczyk, R.; Usvyat, D.; Schütz, M.; Sauer, J.; Freund, H. J. A Two-Dimensional "Zigzag" Silica Polymorph on a Metal Support. *J. Am. Chem. Soc.* **2018**, *140* (19), 6164−6168.
(34) Lewandowski, A. L.; Tosoni, S.; Gura, L.; Yang, Z.; Fuhrich, A.; Prieto, M. J.; Schmidt, T.; Usvyat, D.; Schneider, W. D.; Heyde, M.; Pacchioni, G.; Freund, H. J. Growth and Atomic-Scale Characterization of Ultrathin Silica and Germania Films: The Crucial Role of the Metal Support. *Chem. - Eur. J.* **2021**, *27* (6), 1870−1885.
(35) Thiel, P. A.; Yates, J. T.; Weinberg, W. H. The Interaction of Oxygen with the Rh(111) Surface A. *Surf. Sci.* **1979**, *82* (1), 22−44.
(36) Ganduglia-Pirovano, M. V.; Scheffler, M. Structural and Electronic Properties of Chemisorbed Oxygen on Rh(111). *Phys. Rev. B: Condens. Matter Mater. Phys.* **1999**, *59* (23), 15533−15543.
(37) Xu, H.; Ng, K. Y. S. STM Study of Oxygen on Rh(111). *Surf. Sci.* **1997**, *375* (2−3), 161−170.
(38) Davis, L. E.; MacDonald, N. C.; Palmberg, P. W.; Riach, G. E.; Weber, R. E. *Handbook Of Auger Electron Spectroscopy*, 2nd ed.; Physical Electronics Division Perkin Elmer Corporation: 6509 Flying Cloud Drive Eden Prairie. Minnesota 55343, 1976; pp 49−53.
(39) Didyk, V. V.; Zakharov, A. I.; Krivitskii, V. P.; Narmonev, A. G.; Senkevich, A. I.; Yupko, L. M. X-ray photoelectronic spectra of ruthenium, rhodium and palladium silicides. *Izv. Akad. Nauk SSSR, Ser. Fiz.* **1982**, 802−806.
(40) Čechal, J.; Šikola, T. A Study of the Formation and Oxidation of PtSi by SR-PES. *Surf. Sci.* **2006**, *600* (20), 4717−4722.
(41) Bonzel, H. P.; Franken, A. M.; Pirug, G. The Segregation and Oxidation of Silicon on Pt(111), OR: The Question of the "Platinum Oxide. *Surf. Sci.* **1981**, *104* (2−3), 625−642.
(42) Niehus, H.; Comsa, G. Bulk Dissolved Si as a Cause of the "Oxide" Formation on Pt(111) Surfaces. *Surf. Sci.* **1981**, *102* (1), L14−L20.
(43) Labich, S.; Kohl, A.; Taglauer, E.; Knözinger, H. Silicide Formation by High-Temperature Reaction of Rh with Model SiO2 Films. *J. Chem. Phys.* **1998**, *109* (6), 2052−2055.
(44) Semancik, S.; Haller, G. L.; Yates, J. T., Jr Impurity Effectss in the Interaction of Oxygen with Rh(111). *Appl. Surf. Sci.* **1982**, *10* (4), 546−558.
(45) Hemmi, A.; Bernard, C.; Cun, H.; Roth, S.; Klöckner, M.; Kälin, T.; Weinl, M.; Weinl, M.; Gsell, S.; Gsell, S.; Schreck, M.; Schreck, M.; Osterwalder, J.; Osterwalder, J.; Greber, T. High Quality Single Atomic Layer Deposition of Hexagonal Boron Nitride on Single Crystalline Rh(111) Four-Inch Wafers. *Rev. Sci. Instrum.* **2014**, *85* (3), 035101.
(46) Watanabe, H.; Fujita, S.; Maruno, S.; Fujita, K.; Ichikawa, M. Selective Thermal Decomposition of Ultrathin Silicon Oxide Layers Induced by Electron-Stimulated Oxygen Desorption. *Appl. Phys. Lett.* **1997**, *71* (8), 1038−1040.
(47) Watanabe, H.; Fujita, K.; Ichikawa, M. Thermal Decomposition of Ultrathin Oxide Layers on Si(111) Surfaces Mediated by Surface Si Transport. *Appl. Phys. Lett.* **1997**, *70* (9), 1095−1097.
(48) Sun, Y. K.; Bonser, D. J.; Engel, T. Thermal Decomposition Process of Ultrathin Oxide Layers on Si(100). *J. Vac. Sci. Technol., A* **1992**, *10* (4), 2314−2321.
(49) Küchle, J. T.; Baklanov, A.; Seitsonen, A. P.; Ryan, P. T. P.; Feulner, P.; Pendem, P.; Lee, T. L.; Muntwiler, M.; Schwarz, M.; Haag, F.; Barth, J. V.; Auwärter, W.; Duncan, D. A.; Allegretti, F. Silicene's Pervasive Surface Alloy on Ag(111): A Scaffold for Two-Dimensional Growth. *2D Mater.* **2022**, *9* (4), 045021.
(50) Nečas, D.; Klapetek, P. Gwyddion: An Open-Source Software for SPM Data Analysis. *Open Phys.* **2012**, *10* (1), 181−188.

https://doi.org/10.1021/acsami.4c05137
ACS Appl. Mater. Interfaces 2024, 16, 27481−27489

Supporting Information for

Interface Effects in the Stability of 2D Silica, Silicide, and Silicene on Pt(111) and Rh(111)

Matthias Krinninger,[†] *Florian Kraushofer,*[†] *Nils B. Refvik,*[‡] *Monika Blum,*[¶] *and Barbara A.J. Lechner**[†,§]

† Functional Nanomaterials Group and Catalysis Research Center, Department of Chemistry, TUM School of Natural Sciences, Technical University of Munich, 85748 Garching, Germany

‡ Department of Physics, University of Alberta, Edmonton, Alberta, T6G 2E1, Canada

¶ Chemical Sciences Division and Advanced Light Source, Lawrence Berkeley National Laboratory, Berkeley, CA 94720, United States

§ Institute for Advanced Study, Technical University of Munich, 85748 Garching, Germany

* bajlechner@tum.de

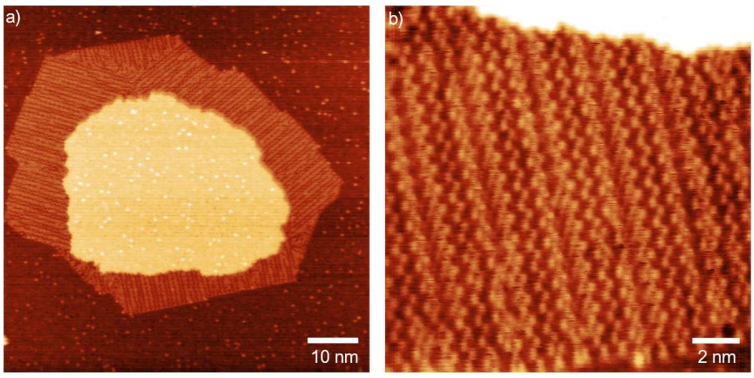

Figure S1. (a) STM image of the $SiO_{2.17}$ "zig-zag" phase[1] on Pt(111), coexisting with the amorphous 2D silica. (b) Zoomed-in STM image of the zig-zag phase in (a). Tunneling parameters: (a) I_t = 0.30 nA, V_b = 0.91 V, 70 × 70 nm^2 and (b) I_t = −0.18 nA, V_b = −0.91 V, 15 × 15 nm^2

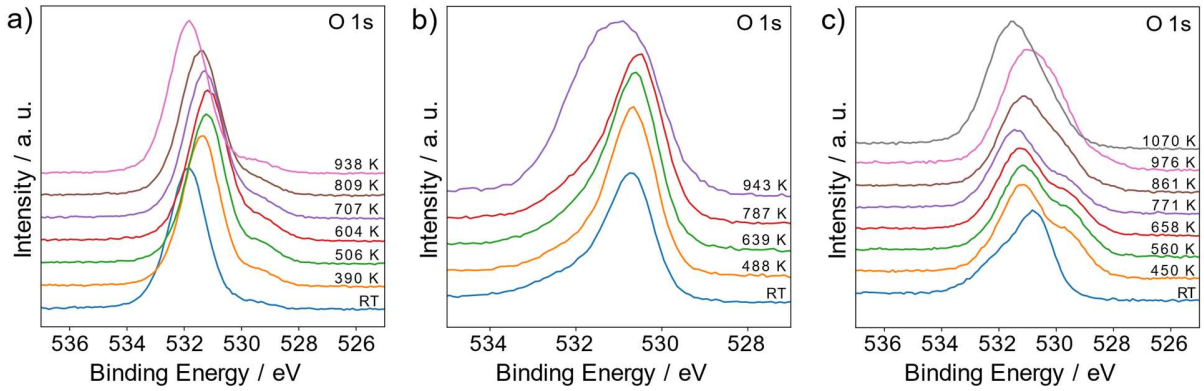

Figure S2. O 1s XPS spectra acquired during film synthesis in 5.0×10^{-6} mbar O_2 for (a) a full monolayer on Rh(111), (b) a full monolayer on Pt(111) and (c) a sub-monolayer film on Pt(111), using an excitation energy of 650 eV.

Table S1. Evolution of binding energies of the Si 2p (excitation energy 300 eV) and O 1s (excitation energy 650 eV) XPS signals and their difference Δ during the 2D SiO_2 film synthesis on Rh(111).

T / K	**BE (Si 2p) / eV**	**BE (O 1s) / eV**	**Δ / eV**
RT	102.8	531.9	429.1
390	102.4	531.4	429.0
506	102.2	531.2	429.0
604	102.0	531.1	429.1
707	102.2	531.3	429.1
809	102.7	531.4	428.7
938	102.9	531.8	428.9

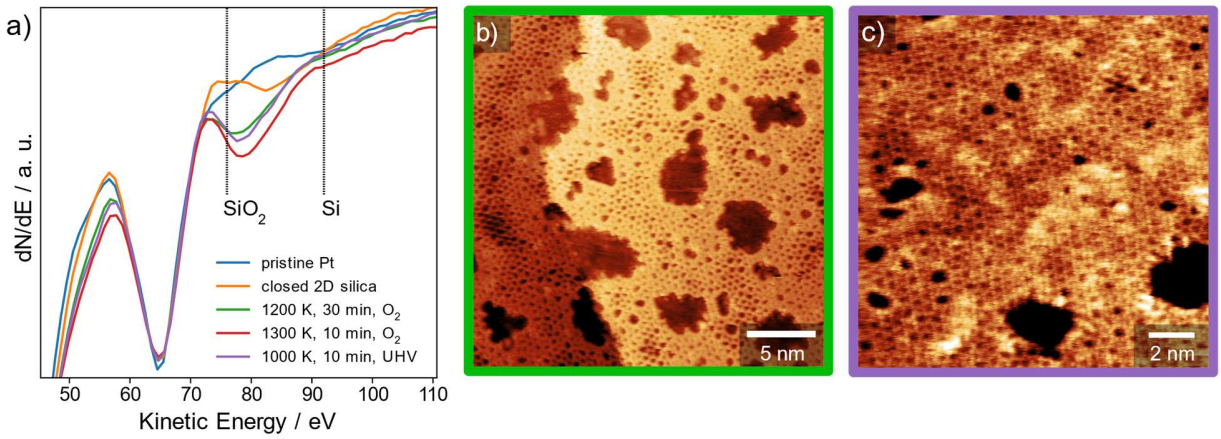

Figure S3. (a) AES spectra (excitation energy 5 keV) of pristine Pt(111) (blue line), fully closed 2D silica on Pt(111) (orange line), the same film after subsequent annealing at 1200 K in 5.0×10^{-6} mbar O_2 for 30 minutes (green line), additional annealing at 1300 K in 5.0×10^{-6} mbar O_2 for 10 minutes (red line), and additional annealing at 1000 K in UHV for 10 minutes (purple line). All spectra are normalized to the Pt signal at 65 eV. As a guide to the eye, the literature values[2] of the kinetic energies of SiO_2 and elemental Si are marked by dashed lines. (b) STM image of the initially closed 2D silica after the first annealing step (corresponding to the green line in (a)), (c) STM image after the last additional annealing step (corresponding to the purple line in (a)).

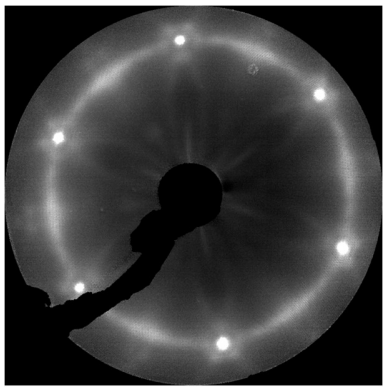

Figure S4. LEED image (103 eV) of fully closed 2D silica on Pt(111), corresponding to the STM images in Figure 1d,e in the main text.

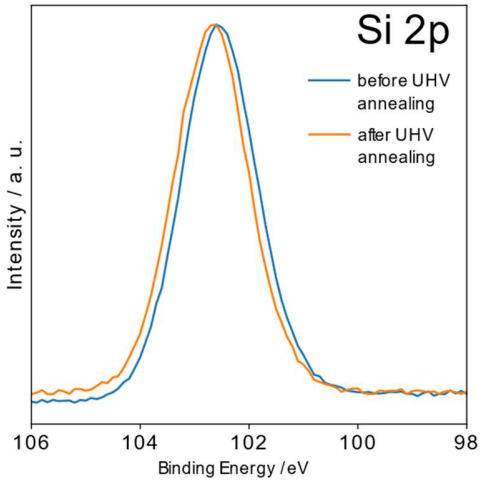

Figure S5. Si 2p XPS spectra of a monolayer 2D silica on Pt(111) before (blue) and after (orange) annealing at 960 K in UHV, measured with an excitation energy of 300 eV.

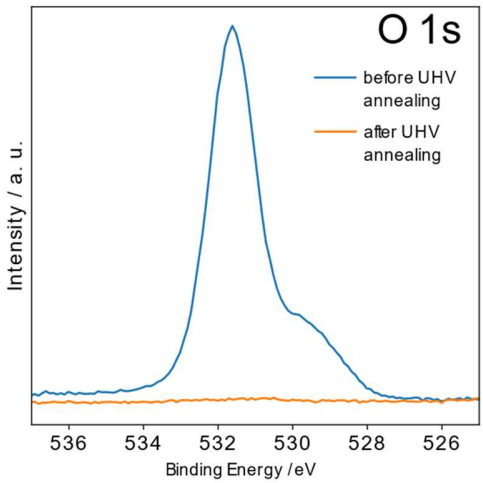

Figure S6. O1s XPS spectra of 2D silica on Rh(111) before (blue) and after (orange) annealing at 946 K in UHV, measured with an excitation energy of 650 eV.

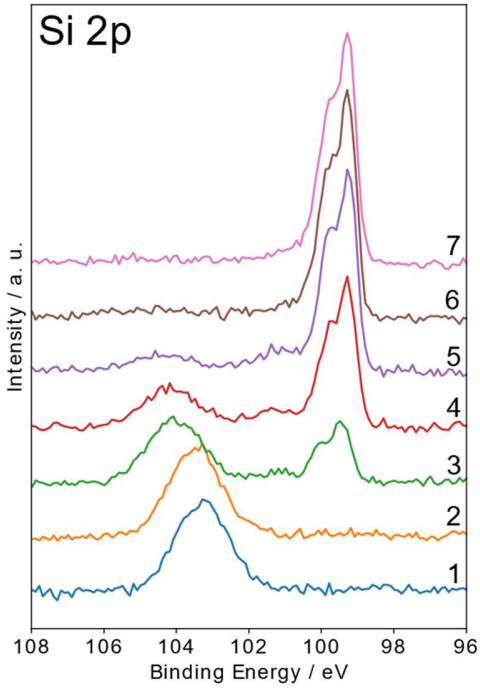

Figure S7. Si 2p XPS spectra (excitation energy 300 eV) of the reduction of the reoxidized surface silicide on Rh(111) at 665 K. Sweep 1 was recorded while the leak valve that had stabilized a pressure of 5×10^{-6} mbar O_2 was closed. Full reduction occurs within 6 subsequent sweeps from the time of closing the valve. The time for one sweep is 46 s.

REFERENCES

(1) Kuhness, D.; Yang, H. J.; Klemm, H. W.; Prieto, M.; Peschel, G.; Fuhrich, A.; Menzel, D.; Schmidt, T.; Yu, X.; Shaikhutdinov, S.; Lewandowski, A.; Heyde, M.; Kelemen, A.; Włodarczyk, R.; Usvyat, D.; Schütz, M.; Sauer, J.; Freund, H. J. A Two-Dimensional "Zigzag" Silica Polymorph on a Metal Support. *J. Am. Chem. Soc.* **2018**, *140* (19), 6164–6168.

(2) Davis, L. E.; MacDonald, N. C.; Palmberg, P. W.; Riach, G. E.; Weber, R. E. *Handbook Of Auger Electron Spectroscopy* **1976**, Second Edi.; Physical Electronics Division Perkin Elmer Corporation.

5.3 The influence of bulk stoichiometry on near-ambient pressure reactivity of bare and Pt-loaded rutile TiO_2(110)

Title: The influence of bulk stoichiometry on near-ambient pressure reactivity of bare and Pt-loaded rutile TiO_2(110)

Authors: Florian Kraushofer*, Matthias Krinninger*, Sebastian Kaiser, Johanna Reich, Agnieszka Jarosz, Matthias Füchsl, Gaurav Anand, Friedrich Esch and Barbara A. J. Lechner (*These authors contributed equally)

Journal: Nanoscale **2024**, *16*, 17825–17837.

Status: Published August 29, 2024

DOI: 10.1039/D4NR01702A

Contributions

Florian Kraushofer and I conducted the majority of experiments and data analysis contained in this publication. Writing of the first draft and data visualization was done by Florian Kraushofer with subsequent iterations by me and Barbara A. J. Lechner. The TPD measurements in Figure 4 (a) and the corresponding STM (Figure S9, supporting information) and XPS measurements (Figure S10, supporting information) were conducted by Sebastian Kaiser and Johanna Reich. Gaurav Anand helped in the LEIS (Figure 4 (b) and the corresponding (NAP-)XPS measurements (Figure S12 and S13). Agnieszka Jarosz (Bachelor's thesis) and Matthias Füchsl (research internship) were both involved with NAP-STM investigations. Friedrich Esch provided supervision. Barbara A. J. Lechner acquired funding, provided supervision and took part in discussions and writing.

Content

In the following publication, we first investigated the surface reactivity of the reducible, bare TiO_2 support in near-ambient pressure atmospheres of O_2, CO_2, H_2 and CO at 600 K by comparison of a near-stoichiometric, lightly reduced (LR-TiO_2) and a highly reduced (HR-TiO_2) sample. In contrast to HR-TiO_2, where surface oxidation or reduction occurs for all mentioned gases, LR-TiO_2 can only be slightly oxidized in an O_2 atmosphere and is inert otherwise. The foundation for these studies is a consistent and reproducible sample preparation over many sputtering and annealing cycles to create a homogeneously distributed stoichiometry over the entire single crystal, which we achieved by automating this process.

Furthermore, Pt nanoparticles with sizes of 5–10 nm were already encapsulated on HR-TiO_2 after sintering in UHV due to SMSI. On LR-TiO_2, we see no evidence for encapsulation upon UHV sintering. Here, only exposure to H_2 at 0.1 mbar and heating at 600 K induces encapsulation. Additionally, in the same gas atmosphere, the already encapsulated Pt nanoparticles on HR-TiO_2 get embedded deeper into the titania surface.

Nanoscale

PAPER

View Article Online
View Journal | View Issue

Cite this: *Nanoscale*, 2024, **16**, 17825

The influence of bulk stoichiometry on near-ambient pressure reactivity of bare and Pt-loaded rutile TiO_2(110)†

Florian Kraushofer, ‡[a] Matthias Krinninger, ‡[a] Sebastian Kaiser, [a,b] Johanna Reich, [a] Agnieszka Jarosz,[a] Matthias Füchsl,[a] Gaurav Anand, [a] Friedrich Esch [b] and Barbara A. J. Lechner *[a,c]

The interaction of catalyst particles with reducible support materials can drastically change their reactivity. On rutile TiO_2, processes like particle encapsulation (caused by the "strong metal–support interaction", SMSI) have long been known to depend on the initial reduction state of the oxide. Despite this knowledge, sample stoichiometry has rarely been controlled in a reproducible manner in the surface science literature. Here, we use scanning tunnelling microscopy (STM) to explore systematically how near-ambient pressures (0.1–1.0 mbar) of O_2, H_2, CO and CO_2 affect blank and Pt-loaded rutile TiO_2(110) surfaces of different bulk stoichiometry at 600 K. To this end, we present preparation recipes that result in a sample stoichiometry always converging back to the same value, which allows us to use the same samples with constant reduction state over hundreds of preparation cycles. Comparing a highly reduced and a near-stoichiometric TiO_2 sample, we find that surface reactivity to all four gasses differs even without Pt loading. Most surprisingly, we find that the highly reduced TiO_2(110) is oxidized by CO_2, but this reaction is completely inhibited on the near-stoichiometric sample. Pt nanoparticles, in turn, become encapsulated after vacuum annealing on the reduced, but not on the near-stoichiometric sample. Encapsulation on the near-stoichiometric sample is achieved only after exposing it to 0.1 mbar H_2 at 600 K. Interestingly, we also see a further modification of the already encapsulated particles on the reduced sample under the same conditions, such that they become embedded deeper in the TiO_2(110) surface.

Received 18th April 2024,
Accepted 19th August 2024

DOI: 10.1039/d4nr01702a

rsc.li/nanoscale

Introduction

Rutile TiO_2 is a prototypical support material in heterogeneous catalysis and has been a staple model system in surface science studies for many years.[1–3] Such model studies aim to understand the atomic-scale structures and mechanisms involved in catalysis by strictly controlling sample preparation and reaction conditions. Bulk or thin film crystalline supports are first precisely characterized in ultra-high vacuum (UHV) before building up complexity to include supported metal particles and reactant molecules. However, this approach is inherently difficult to reconcile with the elevated pressures typically associated with applied heterogeneous catalysis, as many of the methods require UHV to function. This divide has been referred to as the "pressure gap", as mechanisms and even surface structures may differ strongly between these two types of environment.[4] In recent years, this issue has been somewhat alleviated as technical advances have allowed classical UHV-based surface-science methods, such as X-ray photoelectron spectroscopy (XPS) and scanning tunnelling microscopy (STM), to also be applied in the "near-ambient pressure" (NAP) regime, *i.e.* up to some mbar.[5–12]

In the case of TiO_2, its interaction with supported metal particles is particularly complex under reducing conditions. A strongly reduced capacity to interact with molecules from the gas phase, and thus significantly lower activity for most reactions, was reported by Tauster for metal catalysts on reducible oxides, and termed the "strong metal–support interaction" (SMSI).[13,14] After some initial debate whether this effect was primarily electronic (through changed particle charge) or geo-

[a]*Functional Nanomaterials Group & Catalysis Research Center, Department of Chemistry, TUM School of Natural Sciences, Technical University of Munich, Lichtenbergstr. 4, 85748 Garching, Germany. E-mail: bajlechner@tum.de*
[b]*Chair of Physical Chemistry & Catalysis Research Center, Department of Chemistry, TUM School of Natural Sciences, Technical University of Munich, Lichtenbergstr. 4, 85748 Garching, Germany*
[c]*Institute for Advanced Study, Technical University of Munich, Lichtenbergstr. 2a, 85748 Garching, Germany*

†Electronic supplementary information (ESI) available: Supplementary figures showing additional STM, LEED, and XPS data; description of diffusion simulations. See DOI: https://doi.org/10.1039/d4nr01702a

‡These authors contributed equally.

metric (through blocking adsorption sites) in nature, it is now the accepted explanation that the particles become encapsulated by a thin suboxide (TiO_x) layer.[15–21] One of the most convincing demonstrations was provided in an STM study by Dulub *et al.*, who obtained atomic resolution of such an overlayer on large Pt particles after UHV annealing, exhibiting a "zigzag" structure.[16] Similar films can be obtained by depositing titanium on Pt(111) and annealing in oxygen, confirming the assignment as TiO_x rather than a Pt–Ti surface alloy.[22,23] In analogy to Dulub *et al.*,[16] Bowker *et al.* showed that both a "zigzag" and a "pinwheel" overlayer structure can coexist on encapsulated Pd on strongly reduced rutile TiO_2(110).[18,19] Recently, it was shown that a different type of encapsulation by stoichiometric TiO_2 occurs in oxidizing environments,[21,24–26] and that particles can even be de-encapsulated in certain $H_2 : O_2$ mixtures.[25] Such reaction mixtures may arguably be the more relevant conditions for many catalysts, but have only recently become widely accessible to model system investigation due to the advances in the NAP-XPS and NAP-STM methods mentioned above.

While SMSI-induced encapsulation and de-encapsulation dynamics clearly depend on the gas environment and temperature, it has further been reported that the sample history, and in particular the bulk stoichiometry of TiO_2 samples, plays a decisive role.[13,27] While UHV-prepared TiO_2(110) surfaces exhibit oxygen vacancies (V_O) as the primary defect, Ti interstitials (Ti_{int}) are known to be the relevant defects in bulk rutile,[28] and can reach concentrations of up to $x \approx 4 \times 10^{-4}$ in TiO_{2-x}, which corresponds to one Ti_{int} per 1250 unit cells.[29] Bulk stoichiometry can be roughly estimated by the sample colour, which turns from transparent yellow-white when stoichiometric *via* translucent blue when somewhat reduced to oblique black when strongly reduced.[1] Reducing a sample further leads to the formation of linear defects of Ti_2O_3 stoichiometry on the (110) facet, which accumulate to form a (1×2) surface reconstruction at higher coverage.[30–32] Reducing the sample even further induces the formation of crystal shear planes in the bulk.[28,29,33]

Interestingly, it has been shown that the encapsulation of particles depends on the electronic structure of the support. Rutile TiO_2 typically acts as an n-type semiconductor due to self-doping with Ti_{int} defects. Fu *et al.* studied the encapsulation of Pd nanoparticles and found that encapsulation occurs on strongly reduced, but not on near-stoichiometric samples.[20] However, encapsulation could also be achieved on Nb-doped samples even when they were only lightly reduced,[20] which indicates that the relevant difference between the samples lies in their electronic structure, rather than just the availability of excess Ti.

The effect of sample stoichiometry on the interaction with clusters or nanoparticles was already considered in some previous publications.[34,35] However, in these works, "low reduced" or "oxidized" samples were obtained either by following a reducing preparation of sputtering and annealing in ultra-high vacuum (UHV), but simply performing fewer preparation cycles than usual,[34] or by reoxidizing only the surface of a reduced sample at low temperature.[35] Neither approach yields a reproducible reduction state, as continued preparation cycles will keep reducing the bulk. The latter approach of low-temperature surface reoxidation has the added disadvantage of introducing a significant stoichiometry profile near the surface, which is both hard to control and to quantify.

Model catalyst studies generally aim to explore catalyst-support interactions in a variety of environments and at different metal loadings. Between experiments, sputtering and annealing cycles are required to remove the added metal particles, and to otherwise clean the samples. To control for the effect of sample stoichiometry, it is important that over tens or even hundreds of these preparation cycles, the samples always converge back to a reproducible bulk stoichiometry. It is easy to see that this is impossible to achieve for a TiO_2 sample without oxygen annealing, as each sputtering step will reduce the near-surface region. In contrast, a typical approach used to "reoxidize" the TiO_2 surface is through UHV annealing. This works for the surface region because Ti_{int} can be accommodated in the bulk,[28] but the resulting bulk concentration of Ti_{int} scales approximately linearly with the number of preparation cycles, and so samples will become more bulk reduced over time. If samples are instead exposed to a mildly oxidizing annealing step after each time they were sputtered, Ti_{int} can diffuse back to the surface and react with oxygen from the gas phase to form new TiO_2 layers.[36] Although this is an activated process,[36–38] it is obvious that the rate of reoxidation partly depends on the bulk Ti_{int} concentration. It follows trivially that alternating between sputtering and oxygen annealing will always lead to convergence at some fixed bulk reduction state, although if the reoxidation is too mild, the converged limit may still be a heavily reduced state.

Here, we report preparation recipes yielding rutile TiO_2(110) crystals with reproducible stoichiometry and explore how sample stoichiometry affects their reactivity. Following previous work, we refer to the two differently prepared samples as lightly reduced and heavily reduced (LR-TiO_2 and HR-TiO_2, respectively).[34] We then use NAP-STM to study the reactivity of blank and Pt-loaded LR-/HR-TiO_2(110) surfaces to near-ambient pressures (0.1–1.0 mbar) of O_2, H_2, CO, and CO_2 at 600 K. We deposit smaller amounts of platinum than in previous studies to avoid interconnected films[18] or partially buried "iceberg" structures,[16] and to better observe particle dynamics. The interpretation of our microscopy results is supported by low energy electron diffraction (LEED), temperature programmed desorption (TPD), (NAP) X-ray photoelectron spectroscopy [(NAP-)XPS], low energy ion scattering (LEIS) and Auger electron spectroscopy (AES). Even without a cocatalyst, we find strong surface interactions of HR-TiO_2 with all four gasses, including significant surface oxidation by CO_2. Platinum nanoparticles on this surface exhibit an SMSI-induced TiO_x overlayer after UHV preparation,[15,16,18] and are remarkably dynamic in a NAP H_2 atmosphere at 600 K. In contrast to HR-TiO_2, the near-stoichiometric LR-TiO_2 sample shows no interaction with CO_2, H_2 or CO, confirming our premise that strict control of the sample stoichiometry is

required. Pt particles on LR-TiO_2 initially remain unencapsulated under UHV annealing, but encapsulate when the surface is reduced in a NAP H_2 atmosphere at 600 K.

Methods

Sample preparation and equilibration

TiO_2(110) single crystal samples were obtained from SurfaceNet GmbH and subjected to cleaning cycles of sputtering (1 keV Ar^+ ions) and annealing. Cleanliness was regularly checked by AES (in the UHV system used for NAP-STM) or XPS (in the UHV systems used for TPD and LEIS measurements). Two of the four samples initially showed traces of potassium impurities, which could be depleted by repeated cleaning cycles. In later experiments, no elements aside from O, Ti, Pt and Ar (implanted during sputtering, also sometimes visible in STM) were ever detected.

We applied two different preparation recipes to obtain samples with distinct, well-controlled stoichiometries. Typical STM images of the as-prepared TiO_2(110) surfaces are shown in Fig. 1, and additional larger-area images are shown in Fig. S1.† In both cases, preparation was carried out with fully automated pressure and temperature control, which let us achieve perfectly reproducible conditions. Fig. 1(c) shows the oxygen pressures and temperatures used to prepare the two samples discussed here (blue squares and black circles), as well as preparation conditions from ref. 34–36. For ref. 35 and 36, the experimental conditions for surface reoxidation are also indicated.

The more strongly reduced sample (HR-TiO_2) was first prepared in a classical manner by cycles of sputtering and annealing in UHV at 1100 K. Note that by "heavily reduced", we mean samples with maximal Ti_{int} concentration before the onset of structural changes of surface or bulk, rather than (1 × 2)-reconstructed surfaces. Once the sample turned completely black and first surface defects indicating the onset of the (1 × 2) reconstruction[30–32] appeared [bright features marked by white arrows in Fig. 1(b)], we stabilized the stoichiometry by introducing an additional oxygen annealing step. For all subsequent experiments, the preparation consisted of sputtering for 15 minutes, then annealing in 3×10^{-6} to 5×10^{-6} mbar O_2 for 10 minutes at 900 to 950 K, and finally annealing in UHV at 1100 K for 20 minutes [black circles (1) and (2) in Fig. 1(c)]. Since the reduced surface defects visible in STM give a reliable indication of at least the near-surface stoichiometry,[39] for this sample, we occasionally varied the temperature and pressure of the oxygen annealing step to more quickly arrive back at the desired state. This was particularly helpful after the strongly oxidizing experiments, as will be discussed below. The bright defects were present in small amounts on the HR-TiO_2 sample during all experiments described below. They always bridge two Ti rows and are the smallest moiety of the Ti_2O_3-stoichiometric reconstruction formed on strongly reduced samples, which becomes (1 × 2)-periodic at high coverage.[30–32] The same type of defect also appears as a metastable phase during sample reoxidation, where it forms "crosslinked" (1 × 2) structures before being transformed into new (1 × 1) layers [orange hexagons in Fig. 1(c)].[32,36,40]

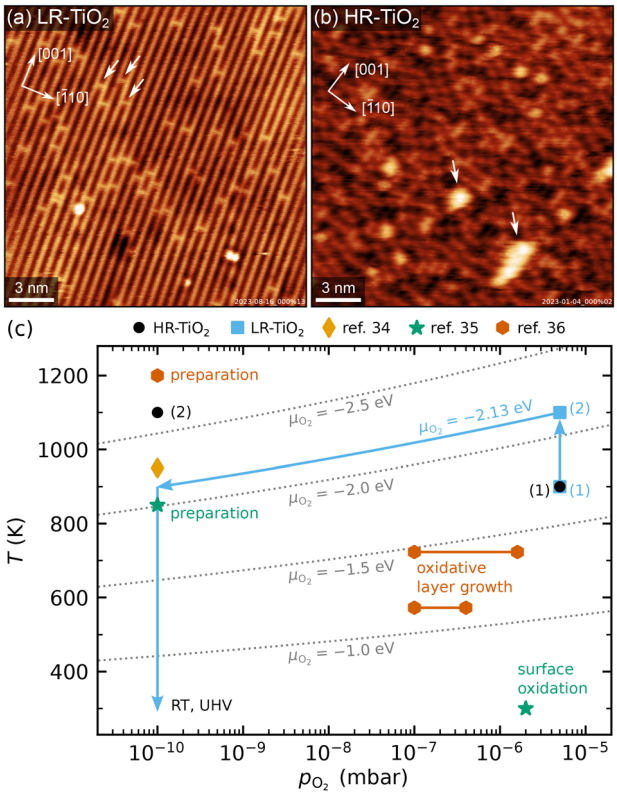

Fig. 1 (a and b) Representative STM images of as-prepared rutile TiO_2(110) surfaces, showing (a) the LR-TiO_2 sample (U_{sample} = 1.2 V, I_{tunnel} = 0.2 nA) and (b) the HR-TiO_2 sample (U_{sample} = 1.2 V, I_{tunnel} = 0.2 nA). White arrows in (a) mark oxygen vacancies, while white arrows in (b) mark (1 × 2)-like line defects. The crystal directions are given in the top left corners, respectively. (c) Pressure-temperature diagram showing the preparation conditions for LR-TiO_2 (blue squares) and HR-TiO_2 (black circles), as well as preparation and experimental conditions from ref. 34–36. Dotted grey lines mark constant oxygen chemical potential μ_{O_2}.

For the only lightly reduced sample (LR-TiO_2), the stoichiometry can in turn be estimated by the number of surface oxygen vacancies V_O [bright spots bridging two Ti rows, marked by white arrows in Fig. 1(a)]. However, they are harder to quantify quickly and routinely, because other defects can have a similar appearance in STM, and acquiring images with sufficiently high quality can be time-consuming. Therefore, we instead consistently used the same preparation recipe and let the stoichiometry equilibrate over a large number of cycles. Each cycle consisted of sputtering for 10 minutes, then annealing in 5×10^{-6} mbar O_2 for 20 minutes at 900 K, and for 10 minutes at 1100 K [blue squares (1) and (2) in Fig. 1(c)]. The low-temperature annealing step has the purpose of reoxidizing the sample, but we found that a high-temperature annealing step is also required to obtain nicely flat (110) surfaces. At 1100 K, the oxygen pressure is likely insufficient to induce significant reoxidation, but should still suppress thermal reduction.

The crystal remained light blue and translucent throughout all experiments shown here, even over a total of hundreds of preparation cycles. Sample conductivity remained high enough for STM and AES throughout, but after some initial preparation cycles (possibly depleting a low concentration of natural dopants), we observed charging effects in LEED at room temperature (RT) below an incident electron energy of 200 eV.

One additional point to consider in the preparation of LR-TiO_2 is that when samples are cooled down in oxygen, Ti_{int} react with O_2 to form undesired TiO_x defects. This behaviour has previously been studied as a function of oxygen pressure and temperature.[36–38] The conditions investigated in ref. 36 are indicated by the orange hexagons labelled as "oxidative layer growth" in Fig. 1(c). These TiO_x species typically form more quickly than they can be incorporated into new (1 × 1) terraces, so this pressure and temperature region should be avoided when cooling down the samples. At even lower temperatures, oxygen reacts with V_O, healing the vacancy and yielding an additional on-top oxygen [O_{ot}, green star in Fig. 1(c)].[35] However, pumping out the oxygen while the sample is still at 1100 K may instead introduce additional V_O defects through thermal reduction. Either species is undesirable if the goal is for the surface to reflect the bulk stoichiometry. We solved this issue by automatically ramping our oxygen pressure to keep the oxygen chemical potential μ_{O_2} constant during the cooling ramp. The final annealing step at 1100 K and 5×10^{-6} mbar of a pure oxygen atmosphere corresponds to $\mu_{O_2} = -2.13$ eV.[41] Keeping this value constant during a linear temperature ramp yields an approximately linear ramp of $\log(p_{O_2})$, reaching the base pressure of 1×10^{-10} mbar at 900 K, as indicated by the blue arrows in Fig. 1(c). Where automatic sample preparation is unavailable, a similar result could likely be obtained by cooling the sample to 900 K in oxygen, then pumping to UHV before continuing the cooling ramp.

Experimental methods

Experiments were performed in three independent UHV setups, using two separate pairs of LR-TiO_2 and HR-TiO_2 samples.

Most data were acquired in a system consisting of two chambers with a base pressure of $<1 \times 10^{-10}$ mbar. One of the chambers houses an SPM Aarhus 150 NAP instrument (SPECS), where all NAP-STM data were acquired. STM was performed in constant-current mode, using electrochemically etched tungsten tips. The other chamber contains instruments for LEED (ErLEED 150, SPECS) and AES (DESA 150, Staib Instruments), a sputter gun (IQE 11, SPECS) and an electron-beam heater, as well as an electron-beam evaporator (EBE-1, SPECS) for depositing Pt (Goodfellow, 99.95%) and a quartz-crystal microbalance (OmniVac) to calibrate the deposition rate. Samples were mounted on stainless steel plates, and their temperature was measured by a K-type thermocouple pressed to the back of the sample by a spring. Since we also heat the samples from the backside, this may result in a slight overestimation of the actual surface temperature, although the effect should be small as the temperature is equilibrated over many minutes. All gasses used in NAP-STM and NAP-XPS experiments were acquired from Westfalen AG (H_2, O_2: grade 5.0, CO_2: grade 4.5, CO: grade 3.7). H_2 and CO were additionally cleaned using a liquid nitrogen cold trap.

LEIS and NAP-XPS measurements were performed on the same samples, which were initially prepared in the NAP-STM setup and then transferred in-house *via* a vacuum suitcase ($p < 5 \times 10^{-9}$ mbar) to the NAP-XPS setup (base pressure $<5 \times 10^{-10}$ mbar). Samples were heated from the back using a laser heater (OsTech DioSource, 976 nm). XPS data were acquired with a PHOIBOS 150 NAP hemispherical analyser (SPECS) and a monochromated X-ray source (XR 50 MF with μFOCUS 600, SPECS). The same analyser and a scannable ion source (IQE 12, SPECS) were used for LEIS.

TPD and corresponding STM and XPS measurements were performed in a separate UHV setup consisting of two chambers with a base pressure of $<1 \times 10^{-10}$ mbar. In one chamber, $C^{18}O$ (Eurisotop, 96.1%) TPD was measured with a quadrupole mass spectrometer (QMA 200 Prisma Plus, Pfeiffer Vacuum) contained in a "sniffer" device[42] described in detail elsewhere.[43] An Omicron EA125 hemispherical analyser and a SPECS XR 50 X-ray source were use for XPS. Pt (Goodfellow, 99.95%) was deposited from a FOCUS EFM-3 electron-beam evaporator. Samples were heated using a pyrolytic boron nitride heater located directly below the sample, while the temperature was measured with a type K thermocouple pressed onto the rim of the tophat-shaped samples. In the other chamber, STM was measured with a Scienta-Omicron VT-AFM instrument in constant-current mode using electrochemically etched tungsten tips, to ensure the sample stoichiometry and surface structure of the two samples is comparable in both setups.

Both the NAP-STM and TPD vacuum systems, where sample preparation was performed, are equipped with automated sputtering, temperature and pressure control systems, which allows running a large number of preparation cycles, typically during the night between experiments. This also enabled linking pressure and temperature setpoints to regulate to a specific oxygen chemical potential μ_{O_2}, which we applied to avoid non-equilibrium oxidation or reduction during the cooling ramps.

STM images were corrected by row alignment along the slow-scan direction and subsequent plane subtraction. Mean apparent nanoparticle heights were determined by evaluating the mean height of their top facet with respect to the supporting TiO_2 terrace, averaging over 30–80 particles in each experiment.

Results

Reactivity of blank TiO_2 surfaces

Fig. 2 summarises the results of exposing the LR-TiO_2 and the HR-TiO_2 samples to various gasses at 600 K and 0.1–1.0 mbar. We show representative stable and well-resolved STM images

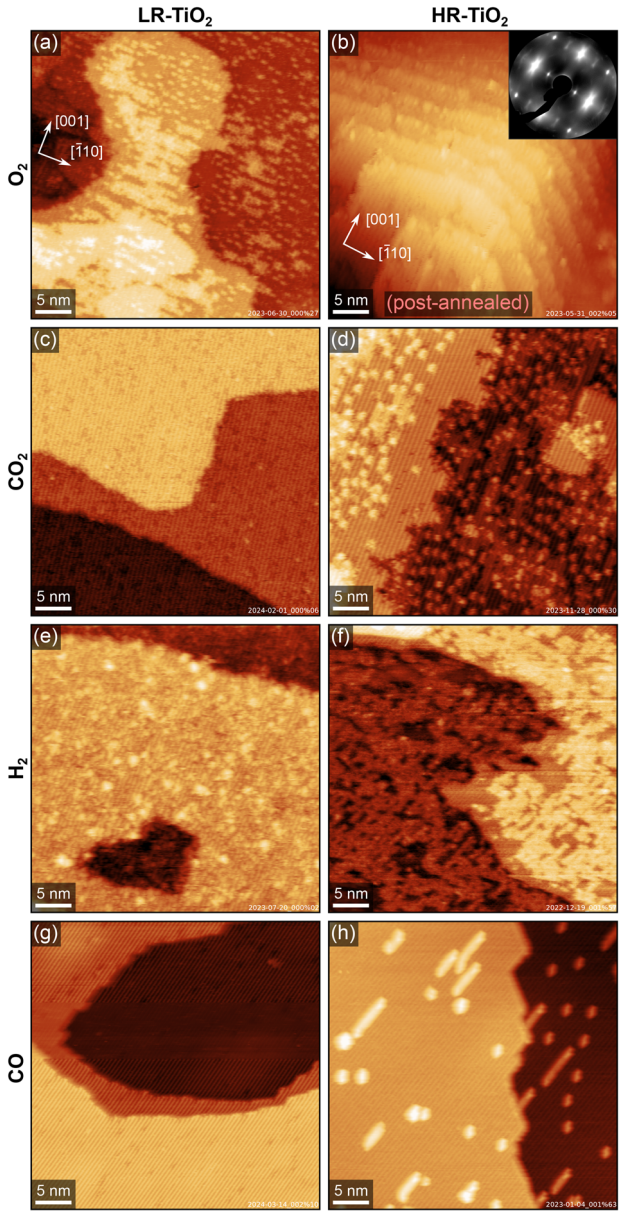

Fig. 2 Representative STM images of LR-TiO_2 (left) and HR-TiO_2 (right) exposed to NAP atmospheres of various gasses at 600 K. The crystal directions of the two crystals are given in the top left corners of (a and b), respectively. (a) LR-TiO_2 after exposure to 0.1 mbar O_2 at 600 K for 15 minutes, image acquired at RT in UHV. (b) HR-TiO_2 after exposure to 0.1 mbar O_2 at 600 K for 15 minutes, image acquired at RT in UHV after post-annealing at 1100 K for 10 minutes in UHV. The inset shows a LEED image taken before post-annealing. (c) LR-TiO_2 after exposure to 1 mbar CO_2 at 600 K for 30 minutes, image acquired at RT in UHV. (d) HR-TiO_2 after exposure to 1 mbar CO_2 at 600 K for 30 minutes, image acquired at RT in UHV. (e) LR-TiO_2 after exposure to 1 mbar H_2 at 600 K for 90 minutes, image acquired at RT in UHV. (f) HR-TiO_2 in 1 mbar H_2 at 600 K, image acquired in gas atmosphere after 100 minutes. (g) LR-TiO_2 in 0.1 mbar CO at 600 K, image acquired in gas atmosphere after 40 minutes. (h) HR-TiO_2 in 1 mbar CO at 600 K, image acquired in gas atmosphere after 40 minutes. Scanning parameters U_{sample} and I_{tunnel} were (a) 2.0 V, 0.2 nA, (b) 1.2 V, 0.01 nA, (c) 1.7 V, 0.2 nA, (d) 1.6 V, 0.6 nA, (e) 1.3 V, 0.1 nA, (f) 1.3 V, 0.2 nA, (g) 1.4 V, 0.3 nA, (h) 1.0 V, 0.5 nA.

for each condition, selecting measurements either under NAP conditions or after the reaction, depending on *in situ* imaging stability under the respective conditions. We observed no significant changes during pumping and cooling, *i.e.* while *in situ* image quality is lower, images acquired near the end of exposure correspond well to the higher-quality images acquired in UHV.

The effect of 0.1 mbar of oxygen is similar to what was observed previously at lower pressures ($\lesssim 2 \times 10^{-6}$ mbar),[31,32,36,40] and can be most clearly observed on the LR-TiO_2 sample [Fig. 2(a), a higher-magnification STM image is shown in Fig. S2(a)†]. Ti_{int} from the bulk reacts with oxygen from the gas phase, forming bright point defects which are reported to be a precursor species to the line defects associated with the (1 × 2) reconstruction.[36] When these defects accumulate, they can form patches of a "crosslinked" (1 × 2) phase,[40] or a more amorphous, metastable "rosette" phase at lower temperature.[31,32] It has been proposed that these crosslinks shift the stoichiometry of the (1 × 2) reconstruction from Ti_2O_3 closer to TiO_2 by incorporating bridging oxygen atoms.[32,40] Once small patches of such intermediate phases have formed, these are then transformed into new (1 × 1)-periodic terraces, presumably with bulk-like TiO_2 stoichiometry and termination.[32,40] The bright patches seen in Fig. 2(a) and Fig. S2(a)† appear similar to the smaller, more amorphous structures reported to form at ≈500 K in low oxygen pressure,[31,32] rather than the larger, (1 × 2)-periodic structures reported at 670–830 K.[36,40]

Post-annealing the same sample at 800 K in UHV for 10 minutes entirely removes the isolated point defects, as shown in Fig. S2(b and c).† However, we still observe some bright linear features extended along [1̄10], *i.e.* perpendicular to the titanium rows, as well as poorly ordered patches with slightly lower apparent height than the added (1 × 1) terraces [Fig. S2(c)†], again similar in appearance to the "rosette" phase.[31,32] We tentatively propose that the linear features are structurally related to this phase, with intermediate stoichiometry TiO_x ($1.5 < x < 2$), and are only prevented from taking a more stable shape by diffusion barriers.

On the HR-TiO_2 sample, we were unable to obtain meaningful STM images during or even directly after exposure to 0.1 mbar O_2 at 600 K, likely due to high surface roughness and poor ordering. The STM image shown in Fig. 2(b) was obtained after post-annealing the sample at 1100 K in UHV for 10 minutes. While the surface termination is mostly (1 × 1) after this treatment, STM still shows strongly increased surface roughness and a correspondingly high step density. Note that while the step density may vary on different areas of the same sample, step bunching as seen in Fig. 2(b) was never observed on as-prepared samples in this work. Conversely, the high step density after O_2 treatment is not limited to this single image, but is representative of other spots on the same sample; we were unable to find any larger flat terraces. We note again that this is already after post-annealing at 1100 K, which usually results in rather flat surfaces (see *e.g.* Fig. S1†). A LEED image taken before the post-annealing step is shown in the inset to

Fig. 2(b) [larger size in Fig. S3(a)†]. Many of the LEED spots exhibit highly diffuse profiles, as well as streaking along the unit cell diagonals, providing further evidence for a highly disorganized surface. A LEED image taken after the post-annealing step, corresponding to the STM image shown in Fig. 2(b), is shown in Fig. S3(b).† While the sharpness of the spots is somewhat improved, streaking along the unit cell diagonals is still pronounced. This can be understood as a signature of the periodically spaced steps also seen in STM.

Flat surfaces could be recovered through the standard preparation cycles, but it is worth noting that we often observed screw dislocations and half-steps indicative of bulk shear planes[28,29,33] on HR-TiO_2 following NAP O_2 experiments. Although these defects were eventually healed over many re-preparation cycles, this suggests that at 0.1 mbar, the re-oxidation proceeds too quickly for perfectly crystalline growth.

STM images of both TiO_2 samples after exposing them to 1 mbar CO_2 for 30 minutes at 600 K are shown in Fig. 2(c and d). On the HR-TiO_2 sample [Fig. 2(d), higher-magnification image in Fig. S4(b)†], the resulting surface appears qualitatively similar to that obtained after O_2 exposure on LR-TiO_2 [Fig. 2(a)], and the ones reported in the literature for oxidation in low O_2 pressure.[31,32,36,40] A large number of bright point defects (likely TiO_x precursor species) coexists with linear (1 × 2)-like defects, small interlinked (1 × 2)-like patches, and small terraces of a (1 × 1)-periodic surface. An STM image acquired in the gas atmosphere only 10 minutes after reaching 600 K is shown in Fig. S4(a).† Here, no additional (1 × 1) terraces and only few linear (1 × 2)-like defects are observed, and the precursor TiO_x point defects dominate. Overall, this strongly suggests that CO_2 acts as a weak oxidizing agent even on the bare rutile TiO_{2-x} surface. As we observed no accumulation of carbon in STM or AES, the most likely mechanism is that CO_2 reacts to CO, leaving oxygen to form new TiO_2 with Ti_{int} from the bulk. Post-annealing in UHV at 800 K [STM image in Fig. S4(c)†] mostly removes the point defects in favour of (1 × 1) terraces and (1 × 2) line defects.

Interestingly, no reaction at all is seen with CO_2 on LR-TiO_2. Fig. 2(c) shows an STM image obtained after 30 minutes in 1 mbar CO_2 at 600 K. We observe only defects that are also present on the pristine surface [Fig. 1(a)], and crucially, not a single one of the pronounced bright TiO_x precursor species. Since these are ubiquitous both on LR-TiO_2 reacting with O_2 [Fig. 2(a)] and on HR-TiO_2 reacting with CO_2 [Fig. 2(d) and Fig. S4(a, b)†], we conclude that no reaction takes place between CO_2 and LR-TiO_2 under the conditions investigated here.

Turning from oxidizing to reducing gasses, Fig. 2(e and f) shows STM images of the two substrates exposed to 1 mbar H_2 at 600 K. The image of LR-TiO_2 [Fig. 2(e)] was acquired in UHV at RT, after 90 minutes at the reaction conditions. Images acquired during H_2 exposure were qualitatively equivalent, but more poorly resolved. The surface appears more defective than directly after UHV preparation or after reaction with CO_2 or CO. Various small defects may correspond to V_O and/or surface OH, though unambiguous assignment is difficult. There are also some slightly larger features with greater apparent height, which resemble the ones assigned as TiO_x precursor species under oxidizing conditions [Fig. 2(a and d)]. However, on this surface, we never observed any (1 × 2)-like row structures or patches after reaction with H_2.

Again, the effect of NAP gas exposure is much more pronounced on the HR-TiO_2 sample. The STM image shown in Fig. 2(f) was acquired during 1 mbar H_2 exposure at 600 K. The step edges appear considerably more frayed than typical for an as-prepared surface, and a network of bright features covers most of the surface. These bright patches are again formed from rows like the ones seen in the (1 × 2) surface reconstruction. This is easiest to demonstrate by post-annealing the surface in UHV, as shown in Fig. S5.† After post-annealing to 773 K [Fig. S5(a)†], we obtain a well-ordered crosslinked (1 × 2) phase covering almost the entire surface. Interestingly, there are also some additional small (<5 nm) islands with (1 × 1) termination. Annealing to higher temperatures [973 and 1100 K, shown in Fig. S5(b and c),† respectively] removes most of the reduced phase, though the surface still exhibits significantly more (1 × 2)-like row defects than before H_2 exposure, even after 20 minutes of annealing at 1100 K.

We have also studied the reaction of HR-TiO_2 with H_2 as a function of temperature. STM images acquired in 1 mbar H_2 while sequentially increasing the temperature are shown in Fig. S6.† No significant increase in the number of defects is observed up to 473 K. At 523 K, bright features start to form on the terraces in a manner very similar to that observed in O_2 on LR-TiO_2. Initially we see primarily point features, which later accumulate into (1 × 2)-like rows. Increasing the temperature to 573 K increases the rate of this process, with more and more rows forming until the surface is largely covered.

Finally, we investigated the reaction of TiO_2(110) with CO. Fig. 2(g and h) shows STM images of LR-TiO_2 and HR-TiO_2, respectively, both acquired in CO at 600 K, ≈40 minutes after reaching that temperature. On LR-TiO_2, the surface appears unchanged from the pristine state after preparation in UHV. On HR-TiO_2, we observe a slightly higher concentration of reduced (1 × 2)-like row defects and their usual point precursors than on the as-prepared surface. Interestingly however, unlike with H_2, the reaction with CO seemed to quickly produce a small number of defects as seen in Fig. 2(h), but this growth then saturated and stopped. While we could show additional defect growth with longer exposure times in H_2 [shown in Fig. S6†], the area seen in Fig. 2(h) remained completely unchanged over 10 minutes of imaging in CO, and even for long exposures, no full coverage of a (1 × 2) phase as observed in hydrogen [Fig. 2(f)] could be obtained. Note that the images shown here were acquired in 0.1 mbar for the LR-TiO_2, but in 1 mbar for the HR-TiO_2. We also tested the influence of pressure on HR-TiO_2, and found no qualitative difference between 0.1 and 1 mbar exposure.

Reactivity of Pt nanoparticles on TiO_2

To investigate how the sample stoichiometry affects supported metal nanoparticles, we first deposited 7 monolayers (ML,

defined as one atom per TiO_2 unit cell, or 5.2×10^{18} m^{-2}) of platinum on HR-TiO_2. Initially, we tried sintering the particles by roughly following the recipe reported by Dulub *et al.*, annealing first at 500 K for 30 minutes, then at 1000 K for 5 minutes, and finally at 800 K for 30 minutes (200 °C, 700 °C and 500 °C, respectively were used by Dulub *et al.*).[16] The Pt particles we obtained in this manner are more closely spaced and their lateral extension is much smaller than that reported previously, possibly due to the smaller amount of deposited material [7 ML *vs.* 25 ML (ref. 16)]. An STM image taken after the initial annealing treatment described above is shown in Fig. 3(a). Fig. 3(b) shows STM of the same sample after an additional 30 minutes of annealing in UHV at 1200 K. The particles are typically 5–10 nm wide, with a mean apparent height of 1.3 nm [see blue height profile in Fig. 3(g)]. We tried various different annealing treatments, as well as keeping the sample at 400 K during Pt deposition, but never obtained significantly larger particles than those shown in Fig. 3. Interestingly, we also observe that many particles are slightly tilted around the [001] axis with respect to the underlying TiO_2(110) surface. When evaluating apparent particle heights, particles were therefore assigned the median value of their surface plane.

A superstructure indicative of encapsulation is resolved in STM already after the initial treatment in Fig. 3(a). Interestingly, the motif more closely resembles the "pinwheel" structure reported by Bowker *et al.* on Pd[18,19] than the "zigzag" structure reported by Dulub *et al.* on Pt(111).[16] Dulub *et al.* also reported an "iceberg" configuration of their particles with some Pt apparently embedded in the surface;[16] in contrast, the overall area coverage and apparent height of our particles after UHV annealing are in good agreement with the nominal amount of deposited Pt, suggesting the nanoparticles are mostly located on top of the TiO_2 surface.

After acquiring the data shown in Fig. 3(b), we exposed these particles to 0.1 mbar H_2 at ≈600 K. A NAP-STM image acquired in hydrogen, ≈84 minutes after the temperature reached 600 K, is shown in Fig. 3(c). Note that the image appears somewhat distorted due to thermal drift of the STM scanner. Several changes can be observed on the surface. First, bright point defects and rows as seen on reduced TiO_2(110)-(1 × 2) surfaces form on the substrate, similar to what was also observed on the bare surface [Fig. 2(f) and Fig. S6†]. Second, the substrate undergoes significant surface roughening, seen as an increased step density in between the Pt nanoparticles. Third, the apparent height of the Pt nanoparticles decreases with respect to their UHV-prepared state [compare the blue and pink height profiles in Fig. 3(g)], and some of them appear almost coplanar with the TiO_2 substrate.

These changes are investigated more closely by the STM images in Fig. 3(d–f), which were acquired after cooling to room temperature and pumping to UHV. The mean apparent height of the encapsulated Pt particles in Fig. 3(d) is ≈0.5 nm [see green height profile in Fig. 3(g)], compared to ≈1.3 nm before hydrogen treatment (blue height profile), while the lateral extension of the particles remains largely unchanged. Note however that the mean apparent height in Fig. 3(d)

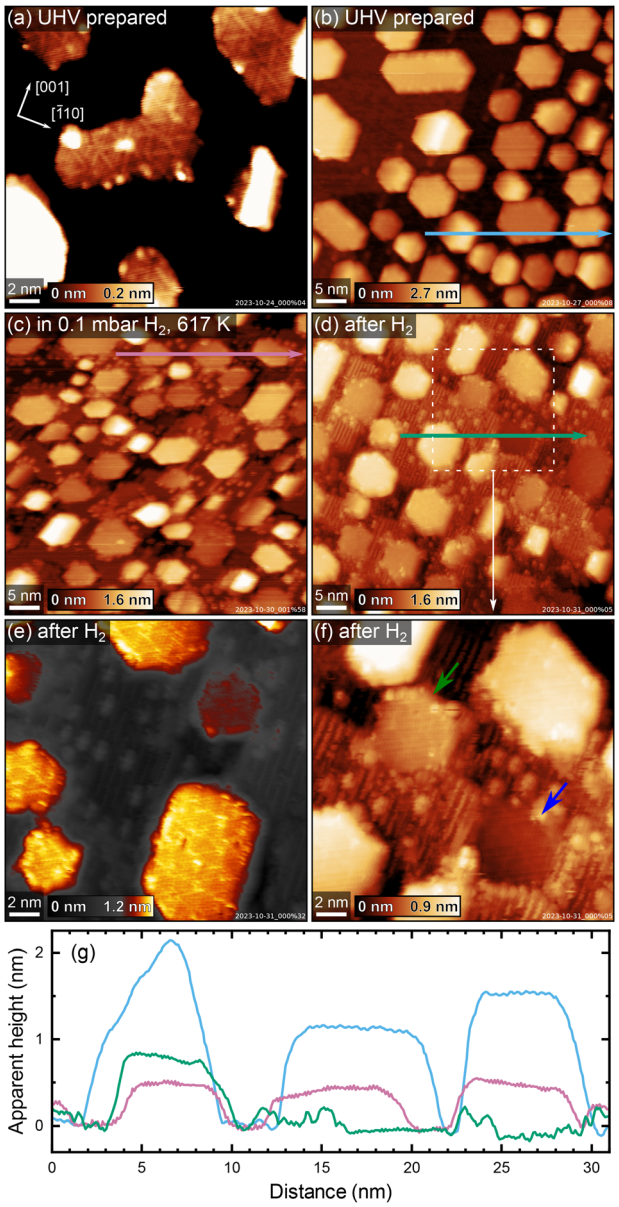

Fig. 3 STM images showing the evolution of Pt nanoparticles on HR-TiO_2 in H_2. (a and b) As-sintered nanoparticles in UHV, (a) annealed 30 minutes at 500 K, 5 minutes at 1000 K and 30 minutes at 800 K, and (b) annealed another 30 minutes at 1200 K. (c) The same sample in 0.1 mbar H_2 at 617 K, ≈84 minutes after a temperature of ≈600 K had been reached. (d–f) Images acquired after cooling to room temperature and returning the sample to UHV. Note the strongly amplified colour scale in (e). (f) Magnified view of the area marked with a dashed white square in (d). (g) Apparent height profiles measured along the horizontal arrows drawn in (b) (blue), (c) (pink), and (d) (green). Scanning parameters U_{sample} and I_{tunnel} were (a) 1.8 V, 0.1 nA, (b) 1.9 V, 0.4 nA, (c) 2.0 V, 0.7 nA, (d and f) 1.7 V, 0.2 nA, and (e) 2.5 V, 0.1 nA.

comes with some systematic uncertainty, as it is difficult to clearly assign particles to a TiO_2 terrace due to the increased number of step edges. Nevertheless, we can unambiguously say that the particles appear to be buried significantly in the surface after H_2 treatment. This is especially clear when con-

sidering some particles in particular, which appear fully coplanar with a TiO_2 terrace. Fig. 3(f) shows a magnified, contrast-adjusted view of the area marked by a dashed white square in Fig. 3(d). Here, the particle indicated by a green arrow appears roughly in-plane with the upper TiO_2 terrace, while the particle indicated by a blue arrow clearly lies on the lower side of the step edge, in-plane with the lower TiO_2 terrace (also seen in the green height profile in Fig. 3). Meanwhile, the superstructure observed before H_2 treatment [Fig. 3(a)] appears unchanged, as seen in Fig. 3(e).

After the experiments shown in Fig. 3, we could again obtain a flatter and nearly defect-free surface by post-annealing in UHV at 1200 K for 30 minutes (STM image shown in Fig. S7†). Here, the mean apparent height of the Pt particles also somewhat increases again, from ≈0.5 nm to ≈0.7 nm.

We then performed the same series of experiments on LR-TiO_2. We obtained a very similar size and shape distribution of particles as on HR-TiO_2 after deposition of 7 ML Pt and sintering at 1000 K in UHV [Fig. S8(a)†]. While some nanoparticle surfaces seem to exhibit a poorly ordered internal structure [Fig. S8(d)†], we never clearly resolved an overlayer as seen on HR-TiO_2, even after annealing at 1200 K in UHV. Unlike on HR-TiO_2, the particles also appear largely unaffected upon exposure to 0.1 mbar H_2 at 600 K [Fig. S8(b and e)†].

To confirm the absence of a TiO_x overlayer on UHV-annealed Pt nanoparticles on LR-TiO_2, we performed $C^{18}O$ TPD measurements. Since these experiments took place in a different UHV setup, STM images of the as-prepared Pt particles on both supports were recorded in the TPD setup (Fig. S9†), which confirm that the surfaces closely resemble those obtained in the NAP-STM chamber on both HR-TiO_2 [Fig. 3(b)] and LR-TiO_2 [Fig. S8(a and d)†]. Fig. S10† shows XPS of the Pt 4f region, taken after Pt deposition and after subsequent sintering of the particles. While the peak shapes and areas for as-deposited Pt are almost identical, we observe a slightly higher binding energy (by ≈0.2 eV) of the Pt 4f peak on HR-TiO_2 than on LR-TiO_2 after sintering in UHV. This observation is consistent with a previously reported shift to higher binding energies upon particle encapsulation.[15]

$C^{18}O$ TPD experiments of UHV-prepared Pt particles on both samples are shown in Fig. 4(a). Even at first glance, it is clear that the CO uptake on the two samples is markedly different, despite the very similar particle size and shape distributions seen in STM [Fig. S9(a and b)†]. Particles annealed at 1000 K on HR-TiO_2 adsorb only a very small amount of CO compared to those on LR-TiO_2 [compare the black and dark blue lines in Fig. 4(a), respectively]. Furthermore, while the main desorption features on Pt/LR-TiO_2 appear at similar temperatures as on an extended Pt(111) surface, CO desorbs at a lower temperature on HR-TiO_2. This is still the case even after further annealing the Pt nanoparticles on LR-TiO_2 in UHV at 1100 K for 75 minutes. While the CO TPD trace [light blue line in Fig. 4(a)] is somewhat decreased compared to the one initially obtained on the same sample, it is still drastically higher than that on HR-TiO_2, and the desorption temperatures of the peaks remain unchanged. Correlating TPD with STM,

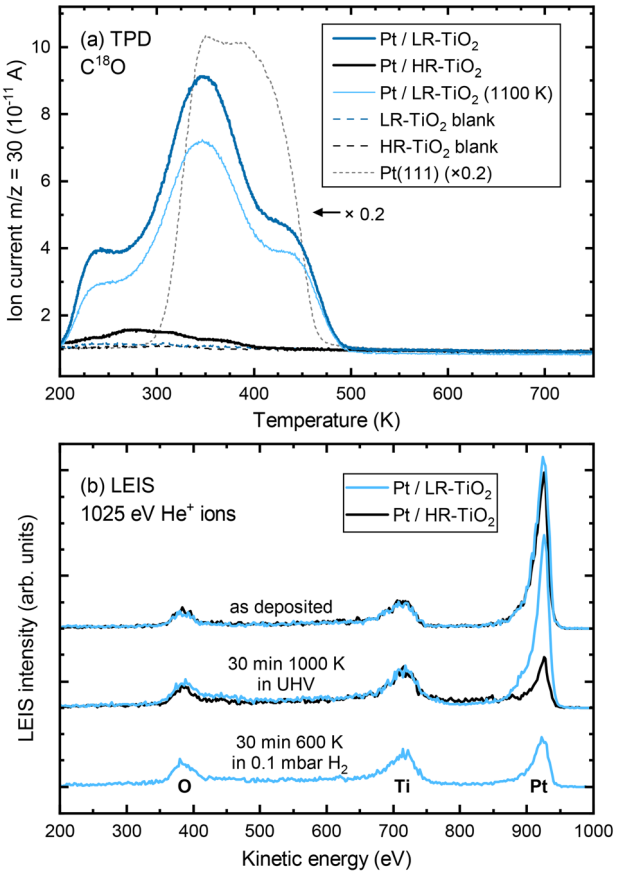

Fig. 4 (a) $C^{18}O$ TPD (1 K s^{-1}) of Pt nanoparticles on HR-TiO_2 (black) and LR-TiO_2 (blue). The dark blue and black curves were acquired after sintering Pt nanoparticles at 1000 K for 15 minutes on LR-TiO_2 and HR-TiO_2, respectively. The light blue curve was acquired after annealing the Pt/LR-TiO_2 sample for an additional 75 minutes at 1100 K. Corresponding STM and XPS data are shown in Fig. S9 and S10, respectively. Black and blue dashed lines show blank measurements of the same samples before depositing Pt. A TPD curve from a Pt(111) single crystal is shown for comparison (scaled ×0.2, dashed grey line). (b) LEIS of Pt nanoparticles on HR-TiO_2 (black) and LR-TiO_2 (blue) directly after Pt deposition (top), after sintering at 1000 K in UHV (centre), and after exposing Pt/LR-TiO_2 to 0.1 mbar H_2 for 30 minutes at 600 K (bottom).

we can attribute the decrease in CO adsorption capacity between 1000 K and 1100 K annealing to further sintering of the particles [compare Fig. S9(b and c)†].

To further investigate this apparent difference in encapsulation behaviour, we also performed LEIS, as shown in Fig. 4(b). The as-deposited spectra show primarily platinum on both samples, though some oxygen and titanium signal remains. This indicates that for a deposition of 7 ML Pt, no closed Pt film is achieved, in good agreement with prior work.[15] Next, the samples were annealed in UHV at 1000 K for 30 minutes. STM images taken after this annealing step are shown in Fig. S11.† At this point, LEIS shows a significant difference between the two samples [Fig. 4(b), centre]: while the peak ratios on LR-TiO_2 are essentially unchanged, the Pt signal on HR-TiO_2 is decreased significantly. This is in good agreement

with the effect seen in TPD [Fig. 4(a)], also indicating encapsulation on the HR-TiO_2, but not the LR-TiO_2 sample. Corresponding XPS data is shown in Fig. S12.† Again, we see a slightly higher binding energy (by ≈0.2 eV) of the Pt 4f peak on HR-TiO_2 than on LR-TiO_2 after sintering in UHV.

Finally, we exposed the LR-TiO_2 sample to 0.1 mbar H_2 and heated it to 600 K while acquiring NAP-XPS (Fig. S13†). Interestingly, when the sample is kept at 600 K, the Pt 4f signal increases, while the O 1s and Ti 2p signals decrease. The original peak ratios are largely restored when the sample is returned to UHV and room temperature after 30 minutes of H_2 exposure, aside from a very slight increase in the Ti^{3+} component of the Ti 2p peak. We tentatively assign this to a spreading of the particles due to a change in metal–support interaction, resulting in a slightly higher area coverage of Pt particles in the H_2 atmosphere, possibly also visible in Fig. S8(b)† compared to Fig. S8(a and c).† LEIS data after this H_2 exposure [Fig. 4(b), bottom] indicates that under these conditions, the particles on LR-TiO_2 also become encapsulated, as the Pt signal is strongly decreased with respect to Ti and O, comparable to that on HR-TiO_2 after UHV annealing.

Discussion

Overall, the various differences in reactivity between the bare LR- and HR-TiO_2 surfaces as well as that of supported Pt nanoparticles on those surfaces confirm the importance of controlling the rutile TiO_2 sample stoichiometry. While the importance of support reduction state for *e.g.* the SMSI effect has been known for decades, unfortunately, much of the existing surface science literature relies on sputtering and "reoxidation" by UHV annealing. While this works fine for a limited number of cycles, it is inherently ill-defined, and leads to a creep in sample stoichiometry over time. It is easy to see that sample stoichiometry will converge for any recipe which includes a sufficiently oxidizing step to compensate the reduction from sputtering and high-temperature UHV annealing. Here, we have presented two recipes producing a consistent support stoichiometry, either highly reduced or near-stoichiometric. We have shown that these recipes provide equivalent results when two sets of TiO_2 samples have been prepared in two different UHV systems.

Interstitial diffusion

Since many of the experimental results rely on extracting Ti_{int} from the subsurface, it is interesting to consider how well the stoichiometry is equilibrated throughout the samples as a function of depth z (*i.e.* distance from the surface). Since the Ti_{int} are extremely dilute in the bulk ($x < 4 \times 10^{-4}$ in TiO_{2-x}),[29] their diffusion can be approximated by a one-dimensional random walk, where stepping along the symmetry-equivalent [100] and [010] directions each corresponds to a step by one layer towards or away from the (110) surface. The probability distribution resulting from such a random walk for any given Ti_{int} after $n \gg 1$ steps is simply a normal distribution centred at its original position, with a root mean square distance given by

$$\sqrt{\overline{\Delta z^2}} = \sigma = d\sqrt{n}$$

with step width d = 3.25 Å. The number of steps n after time t follows

$$n = t\nu_0 e^{-\frac{E_B}{k_B T}}$$

with a preexponential factor ν_0 typically on the order of 10^{13} s^{-1}. A surprising spread of values is reported in the literature for the activation barrier E_B of Ti_{int} bulk diffusion. While tracer diffusion and conductivity relaxation studies consistently report $E_B \approx 0.5$ eV perpendicular to the [001] direction [*i.e.* towards or away from the (110) surface],[44–46] contrasting values were found in STM-based studies. Smith *et al.* observed the growth of new TiO_2 layers in low pressures of oxygen, and found a linear dependence on oxygen pressure and an apparent activation energy of only 0.25 eV.[36] Since the process continued indefinitely without exhausting the subsurface Ti_{int}, the authors concluded that the activation energy in the bulk must be of the same magnitude.[36,47] In sharp contrast, Zhang *et al.* investigated the oxidation of single Ti_{int} atoms at the surface between 360 K and 400 K with STM and electron-stimulated desorption (ESD), and extrapolated an activation energy of $E_B \approx 1.0$ eV.[37] This was supported by DFT calculations, where a barrier of 1.2 eV was obtained for subsurface-to-surface diffusion, though interestingly the same work shows a lower barrier of 0.75 eV for diffusion to the subsurface from a deeper layer.[48]

Based on these considerations, we can use the standard deviations σ for Ti_{int} positions after a given number of steps as a measure of typical diffusion lengths when annealing. For example, assuming a diffusion barrier of 0.5 eV, σ is as large as 0.3 mm after only one minute of annealing at 900 K, and on the order of 0.1 mm after one minute even at 600 K. We can therefore expect rapid equilibration throughout the bulk for typical sample thicknesses of 0.5 to 3 mm, and high availability of Ti_{int} at the surface even at low bulk concentrations. Standard deviations σ as a function of the assumed bulk diffusion barrier are shown in Fig. S14(a)† for selected times and temperatures.

Separate from the experiments reported above, we have performed studies on 0.5 mm thick TiO_2(110) samples, which we bulk-reduced by sputtering with 1 keV Ar^+ ions while annealing at 1100 K for several hours until they exhibited a (1 × 2) LEED pattern. When exposing these samples to 0.1 mbar O_2 at 600 K, we have found that they can be fully reoxidized (as judged by a change in colour from opaque black to transparent yellow-white) over the course of several hours. Assuming only a bulk diffusion barrier of 0.5 eV, one would expect a much faster reoxidation, on a timescale of only minutes. It is reasonable to assume that under these conditions, the availability of oxygen from the gas phase is not rate-limiting. Likewise, previous DFT calculations suggest that the O_2 dissociation is barrierless once a Ti_{int} diffuses to the surface and interacts with

an O_2 molecule.[48] These species must then diffuse to form new rutile terraces before the next layer can form.[36] It seems plausible that this more complex, multi-step process has a higher effective barrier, which can explain the apparent discrepancy between reported bulk diffusion barriers[44–46] and the ≈1 eV surface oxidation barrier obtained from ESD.[37] Note that for bulk diffusion, we can rule out both the proposed 0.25 eV (ref. 37) and 1.0 eV (ref. 36) barriers, as they would result in much faster and much slower reoxidation, respectively.

We have performed simple simulations (described in more detail in the ESI†) to model Ti_{int} diffusion following the random-walk scheme outlined above. This allows us to qualitatively compare our experimental results to the different barriers reported in the literature, and to estimate how many preparation cycles are required to equilibrate a sample. Fig. 5 shows depth profiles of the Ti_{int} distribution in a 2 mm thick sample resulting from cycles of sputtering (reducing the surface) and oxygen annealing at 900 K for 20 minutes, assuming barriers of 0.6 eV for bulk diffusion, 1.0 eV for oxidation at the surface (neglecting pressure dependence), and a preexponential factor $\nu_0 = 10^{13}$ s^{-1}. We choose to show the slightly higher (0.6 eV) than commonly reported barrier here because it more clearly illustrates the evolution of bulk concentration profiles. The same plot for a barrier of 0.5 eV is shown in Fig. S14(b).† Solid lines show the evolution of a sample starting from a fully oxidized state, while dashed lines start from an arbitrarily but homogeneously reduced state. In both cases, the sample is well-equilibrated after about 30 cycles. The remaining stoichiometry gradient at the surface is due to the continual reoxidation, and is less pronounced for a smaller bulk diffusion barrier, as shown in Fig. S14(b).† If we include our final annealing step of 1100 K in the simulation, and assume that no further oxidation takes place at that point due to the strongly reduced oxygen chemical potential μ_{O_2}, then no stoichiometry gradient remains from the surface to the bulk, as shown in Fig. S14(c).† The bulk concentration always converges to a constant value in these simulations, which matches the experimental observation of a reproducible crystal stoichiometry (as judged by surface defects and the sample colour) over hundreds of cycles.

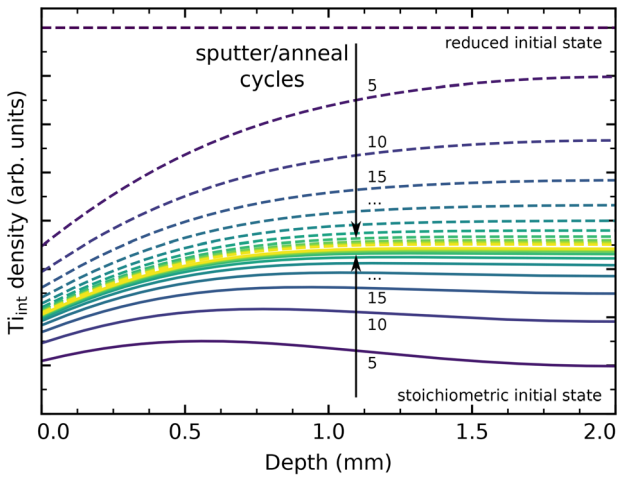

Fig. 5 Ti_{int} concentration profiles in a 2 mm thick rutile TiO_2(110) crystal from a simple diffusion simulation, shown after a given number of cycles of sputtering and annealing in O_2 for 20 minutes at 900 K. Here, the bulk diffusion barrier was set to 0.6 eV, with a surface reaction barrier of 1 eV determining the rate of reoxidation. Solid and dashed lines show equilibration when starting from a fully stoichiometric and from a homogeneously reduced initial state, respectively, both arriving at a stationary state shown in yellow.

Overall, our results are generally consistent with a ≈0.5 eV barrier for bulk Ti_{int} diffusion perpendicular to the (110) surface, as reported in tracer diffusion studies.[44–46] However, we conclude that a higher barrier for oxidative reaction of Ti_{int} at the surface should be assumed, as we otherwise would expect even faster reoxidation of heavily reduced samples than is actually observed. This is in good agreement with the work by Zhang *et al.*, who estimate a barrier of ≈1.0 eV for reaction with adsorbed oxygen below 400 K.[37]

Oxidizing conditions

Qualitatively, the rapid growth of TiO_x ad-species in O_2 and, ultimately, the formation of new TiO_2 terraces is easy to understand. While the rate of material growth was observed to scale linearly with p_{O_2} at lower pressure [$<10^{-5}$ mbar, orange lines in Fig. 1(c)],[36] the impingement rate of O_2 per TiO_2(110) surface unit cell is 5.2×10^4 s^{-1} at 600 K and 0.1 mbar. It therefore seems unlikely that the availability of O_2 at the surface is still rate-limiting. As discussed above, assuming a bulk diffusion barrier for Ti_{int} of 0.5 eV, bringing titanium to the surface is likewise extremely fast. The rate of material growth is then mainly determined by an effective surface reaction barrier, which must include not only the reaction of Ti_{int} with O_2 at the surface, but also the accumulation and structural rearrangement of new TiO_x precursor material into bulk-structured TiO_2 terraces. The previously reported value of ≈1.0 eV (ref. 37) should therefore be seen as a lower bound. The results on LR-TiO_2 indicate that at 600 K, on-surface diffusion of the precursor point defects is sluggish, and once formed, terraces remain small rather than accumulating into larger ones. Indeed, on HR-TiO_2, LEED and (after post-annealing) STM both indicate highly disordered growth and surface roughening. The observation of bulk defects (seen as screw dislocations and half-steps in STM, data not shown) after NAP oxygen exposure also fits into this picture. The much higher rate of growth on HR-TiO_2 is readily explained by the higher availability of Ti_{int} in that sample.

In contrast to O_2, we observe a clear qualitative difference between the LR-TiO_2 and HR-TiO_2 samples in CO_2. While the NAP exposure is clearly mildly oxidizing on HR-TiO_2, no material growth at all is observed on LR-TiO_2. Though one may reasonably expect a slower rate of oxidation based on the lower availability of Ti_{int}, comparison with the NAP O_2 experiment still suggests that TiO_x species should also form on LR-TiO_2, albeit at a lower rate. The fact that not a single defect was found in STM even after 30 minutes at 600 K suggests that the reaction of Ti_{int} either has a significantly higher activation

barrier on LR-TiO_2 than on HR-TiO_2, or is thermodynamically unfavourable.

Based on the fact that no carbon residue is found on the surface by AES and STM after oxidation with CO_2, we can assume that CO_2 reacts to CO, providing an oxygen to bind to Ti_{int} diffusing from the bulk. The full reaction can then be written as

$$Ti_{int}^{3+} + 2CO_2(g) + 3e^- \rightarrow TiO_2(s) + 2CO(g).$$

While the exact reaction process is likely to be complex, with multiple CO_2 molecules interacting with an active site, we can at least estimate the overall reaction enthalpy ΔH of such a process. The reaction of O_2 with Ti_{int} has been investigated by DFT in previous work, where the authors found an energy gain of 6.6 eV from forming an on-surface TiO_2 ad-species, compared to Ti_{int} in a subsurface layer and O_2 in the gas phase.[48] The cost of reducing CO_2 to CO, $CO_2(g) \rightarrow CO(g) + \frac{1}{2}O_2(g)$, is well-known ($\Delta H_0$ = 2.93 eV).[41] Comparing directly, we obtain an energy gain of ≈0.7 eV for oxidation of Ti_{int} to a TiO_2 ad-species, using two CO_2 molecules from the gas phase.

We speculate that the surprising inertness of the LR-TiO_2 surface is likely related to the different electronic structure in comparison to HR-TiO_2. Activating adsorbed CO_2 typically requires first transferring an electron to the molecule.[49] Initiating the reaction with Ti_{int} thus requires two charge transfer events to adsorbed molecules in close proximity. This is in contrast to the reaction with oxygen, which can proceed in a single step through reaction of Ti_{int} with an O_2 molecule.[48] Rutile TiO_{2-x} is an n-type semiconductor, with the Fermi level position (relative to the band structure) determined by the doping level, which in our samples corresponds simply to the Ti_{int} concentration. The stoichiometry of the crystal thus determines not only the number of available charge carriers, but also their energy relative to adsorbed species. It therefore seems plausible that on the LR-TiO_2 sample, the reaction with CO_2 may be completely inhibited, rather than just proceeding at a lower rate than with O_2.

Reducing conditions

In reducing atmospheres, we observe that both H_2 and CO further reduce HR-TiO_2, though the initial reaction with CO quickly stops. Intuitively, it makes sense that reducing the surface should form the (1 × 2) phase, which is generally assigned as Ti_2O_3 (though the crosslinked precursors may be less reduced).[32,40] However, the atomistic mechanism is less clear than for oxidation. It seems that new (1 × 2)-like features form as ad-species on each terrace, nucleating seemingly at random. This begs the question where the material for these defects is drawn from.

Bowker and Bennett have investigated the thermal reduction process of a (1 × 2)-terminated TiO_2(110) sample in UHV, and observed material loss in the form of retraction of (1 × 2) steps, without interconversion to (1 × 1).[47] In that case, it is easy to conclude that oxygen is lost to the gas phase, and excess Ti diffuses to the bulk as Ti_{int}. It is reasonable to assume that oxygen is similarly mainly removed from steps in the reaction with hydrogen, and indeed, the step edges often have a frayed appearance [see Fig. 2(f)]. Leftover Ti may then diffuse laterally to form the reduced surface phases as easily as moving to the bulk. However, forming Ti_2O_3 ad-features in this way clearly also requires oxygen, which must either be extracted from the step as well, or else from the underlying terrace.

On other reducible oxide surfaces like Fe_3O_4(001), accumulation of oxygen vacancies on a terrace typically results in the appearance of isolated, extended holes in the surface as excess Fe diffuses to the bulk.[50,51] While hard to rule out entirely, we have not observed this on TiO_2. An alternative mechanism may be that OH groups are formed at step edges, and that these diffuse on the surface either independently, or in combination with excess Ti from the same step edge as a $Ti(OH)_x$ species. Such a precursor species could then react to Ti_2O_3 (or possibly a hydroxylated form thereof) on the surface. However, as the formation of ad-species close to steps is observed just as much as on terraces, nucleation may equally involve some additional terrace defect.

Post-annealing of HR-TiO_2 in UHV leads to ordering of the reduced ad-features [Fig. S5(a)†] at low temperatures, and partly recovers a (1 × 1) surface at higher temperatures [Fig. S5 (b and c)†]. This is easily understood as the same process seen in the "reoxidation" of samples by UHV annealing after sputtering, where excess Ti is dissolved into the bulk as Ti_{int}. However, the concentration of (1 × 2) rows on the surface after post-annealing is still noticeably higher than before H_2 exposure, indicating significant overall reduction of the sample.

It is interesting to note that no extensive reduction takes place in CO on either sample. The fact that the reaction stops after only a few reduced ad-species have been formed suggests that CO reacts solely with some preexisting defect, thus self-limiting the process. The observation of continued reduction of HR-TiO_2 with hydrogen, but not with CO, suggests that the rate-limiting step is the extraction of lattice oxygen, rather than the adsorption and dissociation of H_2. The inert behaviour of LR-TiO_2 to CO exposure may indicate that the required defects are not available on that sample.

Nanoparticle encapsulation

Concerning Pt nanoparticles, we very clearly see encapsulation on HR-TiO_2 in STM (Fig. 3), TPD and LEIS (Fig. 4). In contrast, no overlayer was observed in STM on LR-TiO_2 (Fig. S8†), and the substantial difference in CO uptake capacity between the two samples seen in TPD convinces us that encapsulation in UHV is inhibited on the near-stoichiometric sample. This is in good agreement with literature: it has long been known that reducing TiO_2 is a prerequisite for the SMSI effect,[13,27] and lower CO uptake capacity was already reported in the original work on SMSI by Tauster.[13,14] However, exposing the sample to hydrogen under near-ambient pressure conditions at 600 K finally results in encapsulation also on LR-TiO_2 as indicated by LEIS [Fig. 4(b)], likely due to surface reduction.

Our findings are in good agreement with previous reports that encapsulation mainly depends on the doping level of the support, rather than the availability of excess Ti.[20] Based on the material growth of the bare samples in a NAP oxygen atmosphere, we can conclude that Ti_{int} can easily diffuse to the surface even at 600 K, including on samples that do not exhibit an SMSI effect. The different interaction of the samples with Pt must therefore be thermodynamically preferred, rather than dictated by kinetic limitations.

Exposing the Pt particles to 0.1 mbar H_2 at 600 K did not result in any significant changes to particle size distributions, or to the nature of an existing TiO_x overlayer. Unexpectedly however, on HR-TiO_2, we observe a significant decrease in apparent height of the particles. Based on the concomitant roughening of the support, we speculate that TiO_2 material from underneath the particles diffuses to form new terraces covering their side facets. This partial burying of the particles is an interesting effect which would hardly be seen by area-averaging techniques like XPS or TPD, where side facets of these relatively flat particles do not contribute strongly. However, it is likely not particularly significant to catalyst activity, as the particle overlayer remains the same. As to what constitutes the driving force for particles becoming embedded in the surface, two explanations are possible: first, that interaction with hydrogen increases the surface energy of side facets covered with the TiO_x suboxide overlayer beyond the interface energy of side facets embedded in stoichiometric TiO_2; or second, that an embedded configuration is already thermodynamically favoured when the particles are first overgrown, but cannot be accomplished due to kinetic limitations. In the second model, the intense surface roughening and restructuring by hydrogen also seen on the bare TiO_2(110) surface [Fig. 2(f)] would allow moving the large particles into a more favourable position. However, taking into account the slightly recovered mean apparent particle heights after UHV post-annealing (Fig. S7†), a modified thermodynamic equilibrium in H_2 atmosphere appears more plausible. It is interesting to note that significant material transport within the TiO_2 substrate can clearly take place even at 600 K to accommodate this.

Conclusions

In conclusion, we have found significant differences in surface reactivity of a near-stoichiometric (lightly reduced, LR-TiO_2) and a highly reduced (HR-TiO_2) TiO_2(110) sample. Near-ambient pressure atmospheres of O_2, CO_2, H_2 and CO at 600 K all induced surface oxidation or reduction on the bare HR-TiO_2 sample, while LR-TiO_2 was only mildly oxidized by O_2 and appears completely inert to the other three gasses. Similarly, Pt particles were encapsulated already after UHV sintering on HR-TiO_2, while encapsulation on LR-TiO_2 was inhibited in UHV, and only occurred when the sample was exposed to 0.1 mbar of H_2 at 600 K. Surprisingly, the already encapsulated particles on HR-TiO_2 were further modified in the hydrogen environment, where they were embedded deeper into the TiO_2 surface. Control of the sample stoichiometry over many preparation cycles has proven crucial in investigating these differences. The recipes we have presented for the preparation of TiO_2(110) samples with reproducible bulk stoichiometry will enable a much more controlled surface preparation and thus help prevent discrepancies and controversies in future experiments.

Author contributions

FK: conceptualization, investigation, data curation, formal analysis, visualization, writing – original draft; MK: conceptualization, investigation, data curation, formal analysis; SK: investigation, formal analysis, visualization; JR: investigation; AJ: investigation, formal analysis; MF: investigation; GA: investigation; FE: resources, supervision; BAJL: conceptualization, funding acquisition, resources, supervision, project administration; all authors: writing – review & editing.

Data availability

The data supporting this article have been included as part of the ESI.†

Conflicts of interest

There are no conflicts to declare.

Acknowledgements

This work was funded by the Deutsche Forschungsgemeinschaft (DFG, German Research Foundation) under Germany's Excellence Strategy EXC 2089/1-390776260 and through the project CRC1441 (project number 426888090, subproject A02), as well as by the European Research Council (ERC) under the European Union's Horizon 2020 research and innovation program (grant agreement no. 850764). F. K. acknowledges funding by the Austrian Science Fund (FWF) [J 4811-N]. B. A. J. L. gratefully acknowledges financial support from the Young Academy of the Bavarian Academy of Sciences and Humanities.

References

1 U. Diebold, *Surf. Sci. Rep.*, 2003, **48**, 53–229.
2 Z. Dohnálek, I. Lyubinetsky and R. Rousseau, *Prog. Surf. Sci.*, 2010, **85**, 161–205.
3 C. L. Pang, R. Lindsay and G. Thornton, *Chem. Rev.*, 2013, **113**, 3887–3948.
4 R. Schlögl, *Angew. Chem., Int. Ed.*, 2015, **54**, 3465–3520.

5 U. Gelius, E. Basilier, S. Svensson, T. Bergmark and K. Siegbahn, *J. Electron Spectrosc. Relat. Phenom.*, 1973, **2**, 405–434.
6 B. J. McIntyre, M. Salmeron and G. A. Somorjai, *Rev. Sci. Instrum.*, 1993, **64**, 687–691.
7 P. B. Rasmussen, B. L. M. Hendriksen, H. Zeijlemaker, H. G. Ficke and J. W. M. Frenken, *Rev. Sci. Instrum.*, 1998, **69**, 3879–3884.
8 E. Laegsgaard, L. Österlund, P. Thostrup, P. B. Rasmussen, I. Stensgaard and F. Besenbacher, *Rev. Sci. Instrum.*, 2001, **72**, 3537–3542.
9 D. F. Ogletree, H. Bluhm, G. Lebedev, C. S. Fadley, Z. Hussain and M. Salmeron, *Rev. Sci. Instrum.*, 2002, **73**, 3872–3877.
10 M. Rößler, P. Geng and J. Wintterlin, *Rev. Sci. Instrum.*, 2005, **76**, 023705.
11 M. Salmeron and R. Schlögl, *Surf. Sci. Rep.*, 2008, **63**, 169–199.
12 F. Tao, L. Nguyen and S. Zhang, *Rev. Sci. Instrum.*, 2013, **84**, 034101.
13 S. J. Tauster, S. C. Fung and R. L. Garten, *J. Am. Chem. Soc.*, 1978, **100**, 170–175.
14 S. J. Tauster, *Acc. Chem. Res.*, 1987, **20**, 389–394.
15 F. Pesty, H.-P. Steinrück and T. E. Madey, *Surf. Sci.*, 1995, **339**, 83–95.
16 O. Dulub, W. Hebenstreit and U. Diebold, *Phys. Rev. Lett.*, 2000, **84**, 3646–3649.
17 S. Labich, E. Taglauer and H. Knözinger, *Top. Catal.*, 2000, **14**, 153–161.
18 R. A. Bennett, C. L. Pang, N. Perkins, R. D. Smith, P. Morrall, R. I. Kvon and M. Bowker, *J. Phys. Chem. B*, 2002, **106**, 4688–4696.
19 M. Bowker, P. Stone, P. Morrall, R. Smith, R. Bennett, N. Perkins, R. Kvon, C. Pang, E. Fourre and M. Hall, *J. Catal.*, 2005, **234**, 172–181.
20 Q. Fu, T. Wagner, S. Olliges and H.-D. Carstanjen, *J. Phys. Chem. B*, 2005, **109**, 944–951.
21 A. Beck, X. Huang, L. Artiglia, M. Zabilskiy, X. Wang, P. Rzepka, D. Palagin, M.-G. Willinger and J. A. van Bokhoven, *Nat. Commun.*, 2020, **11**, 3220.
22 A. B. Boffa, H. C. Galloway, P. W. Jacobs, J. J. Benítez, J. D. Batteas, M. Salmeron, A. T. Bell and G. A. Somorjai, *Surf. Sci.*, 1995, **326**, 80–92.
23 F. Sedona, G. A. Rizzi, S. Agnoli, F. X. Llabrés i Xamena, A. Papageorgiou, D. Ostermann, M. Sambi, P. Finetti, K. Schierbaum and G. Granozzi, *J. Phys. Chem. B*, 2005, **109**, 24411–24426.
24 X. Liu, M.-H. Liu, Y.-C. Luo, C.-Y. Mou, S. D. Lin, H. Cheng, J.-M. Chen, J.-F. Lee and T.-S. Lin, *J. Am. Chem. Soc.*, 2012, **134**, 10251–10258.
25 H. Frey, A. Beck, X. Huang, J. A. V. Bokhoven and M. G. Willinger, *Science*, 2022, **376**, 982–987.
26 P. Petzoldt, M. Eder, S. Mackewicz, M. Blum, T. Kratky, S. Günther, M. Tschurl, U. Heiz and B. A. J. Lechner, *J. Phys. Chem. C*, 2022, **126**, 16127–16139.
27 A. Berkó, I. Ulrych and K. C. Prince, *J. Phys. Chem. B*, 1998, **102**, 3379–3386.
28 M. A. Henderson, *Surf. Sci.*, 1999, **419**, 174–187.
29 M. Aono and R. R. Hasiguti, *Phys. Rev. B: Condens. Matter Mater. Phys.*, 1993, **48**, 12406–12414.
30 O. Hiroshi, F. Ken-ichi and I. Yasuhiro, *Bull. Chem. Soc. Jpn.*, 1995, **68**, 2447–2458.
31 M. Li, W. Hebenstreit, L. Gross, U. Diebold, M. A. Henderson, D. R. Jennison, P. A. Schultz and M. P. Sears, *Surf. Sci.*, 1999, **437**, 173–190.
32 M. Li, W. Hebenstreit and U. Diebold, *Phys. Rev. B: Condens. Matter Mater. Phys.*, 2000, **61**, 4926–4933.
33 R. Bennett, S. Poulston, P. Stone and M. Bowker, *Phys. Rev. B: Condens. Matter Mater. Phys.*, 1999, **59**, 10341.
34 S. Bonanni, K. Aït-Mansour, W. Harbich and H. Brune, *J. Am. Chem. Soc.*, 2012, **134**, 3445–3450.
35 F. Rieboldt, L. B. Vilhelmsen, S. Koust, J. V. Lauritsen, S. Helveg, L. Lammich, F. Besenbacher, B. Hammer and S. Wendt, *J. Chem. Phys.*, 2014, **141**, 214702.
36 R. D. Smith, R. A. Bennett and M. Bowker, *Phys. Rev. B: Condens. Matter Mater. Phys.*, 2002, **66**, 035409.
37 Z. Zhang, J. Lee, J. T. Yates, R. Bechstein, E. Lira, J. Ø. Hansen, S. Wendt and F. Besenbacher, *J. Phys. Chem. C*, 2010, **114**, 3059–3062.
38 D. Matthey, J. G. Wang, S. Wendt, J. Matthiesen, R. Schaub, E. Lægsgaard, B. Hammer and F. Besenbacher, *Science*, 2007, **315**, 1692.
39 M. Reticcioli, M. Setvin, X. Hao, P. Flauger, G. Kresse, M. Schmid, U. Diebold and C. Franchini, *Phys. Rev. X*, 2017, **7**, 031053.
40 R. A. Bennett, P. Stone, N. J. Price and M. Bowker, *Phys. Rev. Lett.*, 1999, **82**, 3831–3834.
41 M. W. Chase, *NIST-JANAF Thermochemical Tables*, National Institute of Standards and Technology, Gaithersburg, Maryland, 4 edn, 1998.
42 S. Bonanni, K. Aït-Mansour, M. Hugentobler, H. Brune and W. Harbich, *Eur. Phys. J. D*, 2011, **63**, 241–249.
43 J. Reich, S. Kaiser, U. Heiz, J.-D. Grunwaldt, M. M. Kappes, F. Esch and B. A. J. Lechner, *Top. Catal.*, 2024, **67**, 880–891.
44 T. S. Lundy and W. A. Coghlan, *J. Phys. Colloq.*, 1973, **34**, C9-299–C9-302.
45 D. A. Venkatu and L. E. Poteat, *Mater. Sci. Eng.*, 1970, **5**, 258–262.
46 D. K. Lee and H. I. Yoo, *Solid State Ionics*, 2006, **177**, 1–9.
47 M. Bowker and R. A. Bennett, *J. Phys.: Condens. Matter*, 2009, **21**, 474224.
48 S. Wendt, P. T. Sprunger, E. Lira, G. K. H. Madsen, Z. Li, J. Ø. Hansen, J. Matthiesen, A. Blekinge-Rasmussen, E. Lægsgaard, B. Hammer and F. Besenbacher, *Science*, 2008, **320**, 1755–1759.
49 Y. Wang, E. Chen and J. Tang, *ACS Catal.*, 2022, **12**, 7300–7316.
50 R. Bliem, J. van der Hoeven, A. Zavodny, O. Gamba, J. Pavelec, P. E. de Jongh, M. Schmid, U. Diebold and G. S. Parkinson, *Angew. Chem.*, 2015, **127**, 14205–14208.
51 S. Kaiser, F. Maleki, K. Zhang, W. Harbich, U. Heiz, S. Tosoni, B. A. J. Lechner, G. Pacchioni and F. Esch, *ACS Catal.*, 2021, **11**, 9519–9529.

The influence of bulk stoichiometry on near-ambient pressure reactivity of bare and Pt-loaded rutile TiO_2(110)

Florian Kraushofer,[a,†] Matthias Krinninger,[a,†] Sebastian Kaiser,[a,b] Johanna Reich,[a] Agnieszka Jarosz,[a] Matthias Füchsl,[a] Gaurav Anand,[a] Friedrich Esch[b] and Barbara A.J. Lechner* [a,c]

[a] Functional Nanomaterials Group & Catalysis Research Center, Department of Chemistry, TUM School of Natural Sciences, Technical University of Munich, Lichtenbergstr. 4, 85748 Garching, Germany

[b] Chair of Physical Chemistry & Catalysis Research Center, Department of Chemistry, TUM School of Natural Sciences, Technical University of Munich, Lichtenbergstr. 4, 85748 Garching, Germany

[c] Institute for Advanced Study, Technical University of Munich, Lichtenbergstr. 2a, 85748 Garching, Germany

* bajlechner@tum.de

† These authors contributed equally.

Supplementary Figures

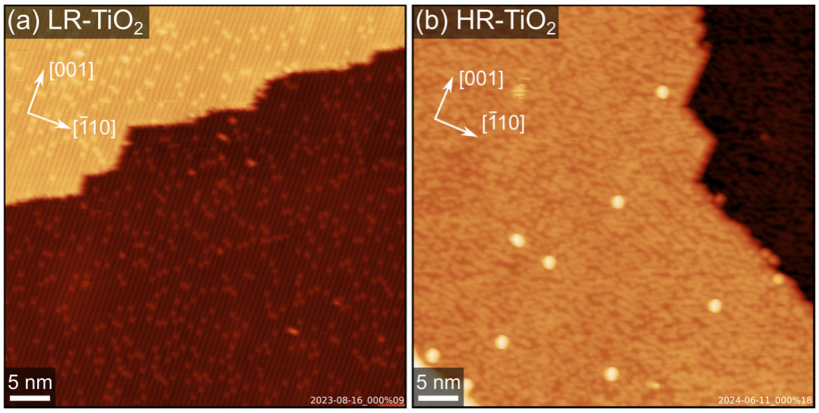

Figure S1. Additional larger-area STM images (50×50 nm^2) of as-prepared rutile TiO_2(110) surfaces, showing (a) the LR-TiO_2 sample (U_{sample} = 1.6 V, I_{tunnel} = 0.3 nA) and (b) the HR-TiO_2 sample (U_{sample} = 1.6 V, I_{tunnel} = 0.1 nA).

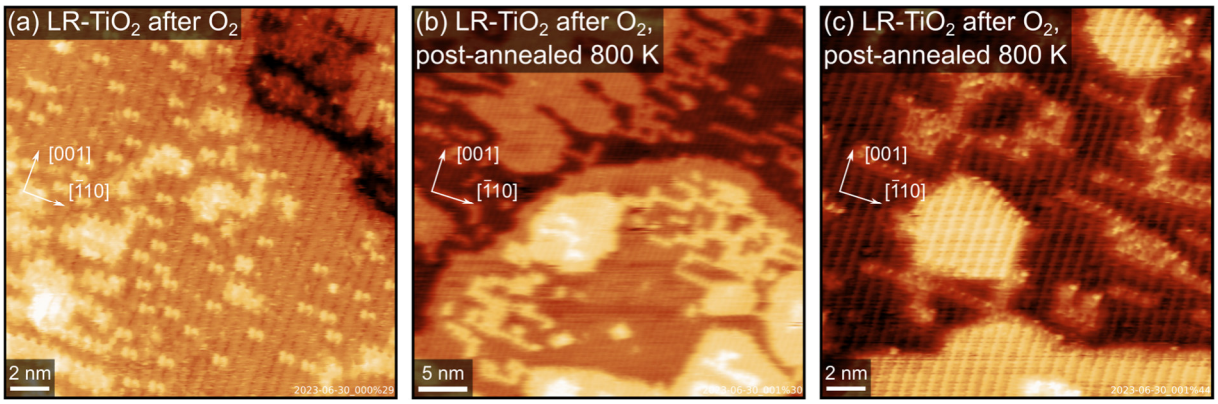

Figure S2. Additional STM images after NAP O_2 exposure of LR-TiO_2, from the same experiment as the image shown in Figure 2(a). (a) LR-TiO_2 after exposure to 0.1 mbar O_2 at 600 K for 15 minutes, and (b,c) after post-annealing at 800 K for 10 minutes in UHV. Images were acquired at RT in UHV, with scanning parameters U_{sample} and I_{tunnel} (a) 1.7 V, 0.1 nA, (b) 1.7 V, 0.2 nA and (c) 1.9 V, 0.1 nA.

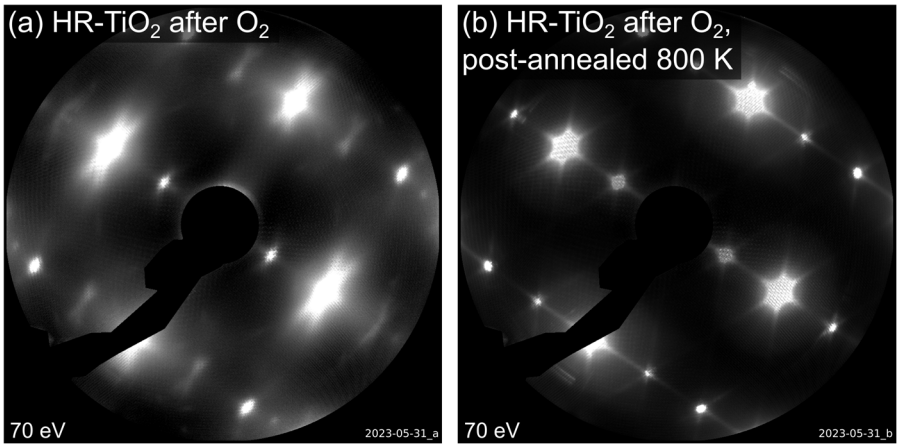

Figure S3. LEED (70 eV incident electron energy) of HR-TiO_2 (a) directly after exposure to 0.1 mbar O_2 at 600 K for 15 minutes [also shown as the inset in Figure 2(b)], and (b) after post-annealing at 1100 K for 10 minutes in UHV, corresponding to the STM image shown in Figure 2(b).

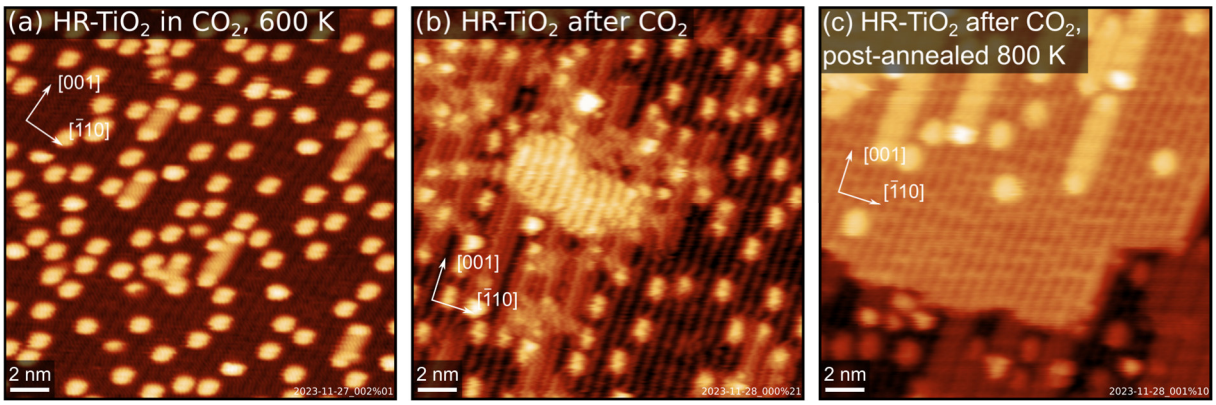

Figure S4. Additional STM images from the NAP CO_2 experiment on HR-TiO_2 shown in Figure 2(d). (a) HR-TiO_2 in 1 mbar CO_2, image acquired in gas atmosphere 10 minutes after reaching 600 K. (b) After exposure to 1 mbar CO_2 at 600 K for 30 minutes, image acquired at RT in UHV, same measurement as the image shown in Figure 2(d). (c) After post-annealing at 800 K for 10 minutes in UHV. Scanning parameters U_{sample} and I_{tunnel} were (a) 1.8 V, 0.2 nA, (b) 2.1 V, 0.2 nA and (c) 1.7 V, 3.3 nA.

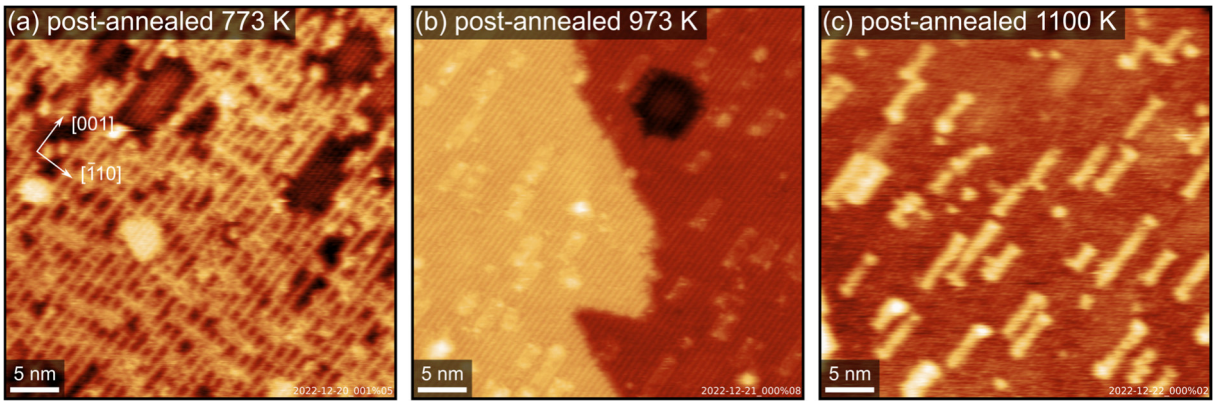

Figure S5. Additional STM images corresponding to the NAP H_2 experiment shown in Figure 2(f), showing the HR-TiO_2 sample post-annealed in UHV after exposure to 1 mbar H_2 at 600 K for 105 minutes. The sample was annealed at (a) 773 K for 10 minutes, (b) 973 K for 10 minutes, and (c) 1100 K for 20 minutes. Images were acquired at RT in UHV, with scanning parameters U_{sample} and I_{tunnel} (a,b) 1.2 V, 0.1 nA and (c) 1.2 V, 0.2 nA.

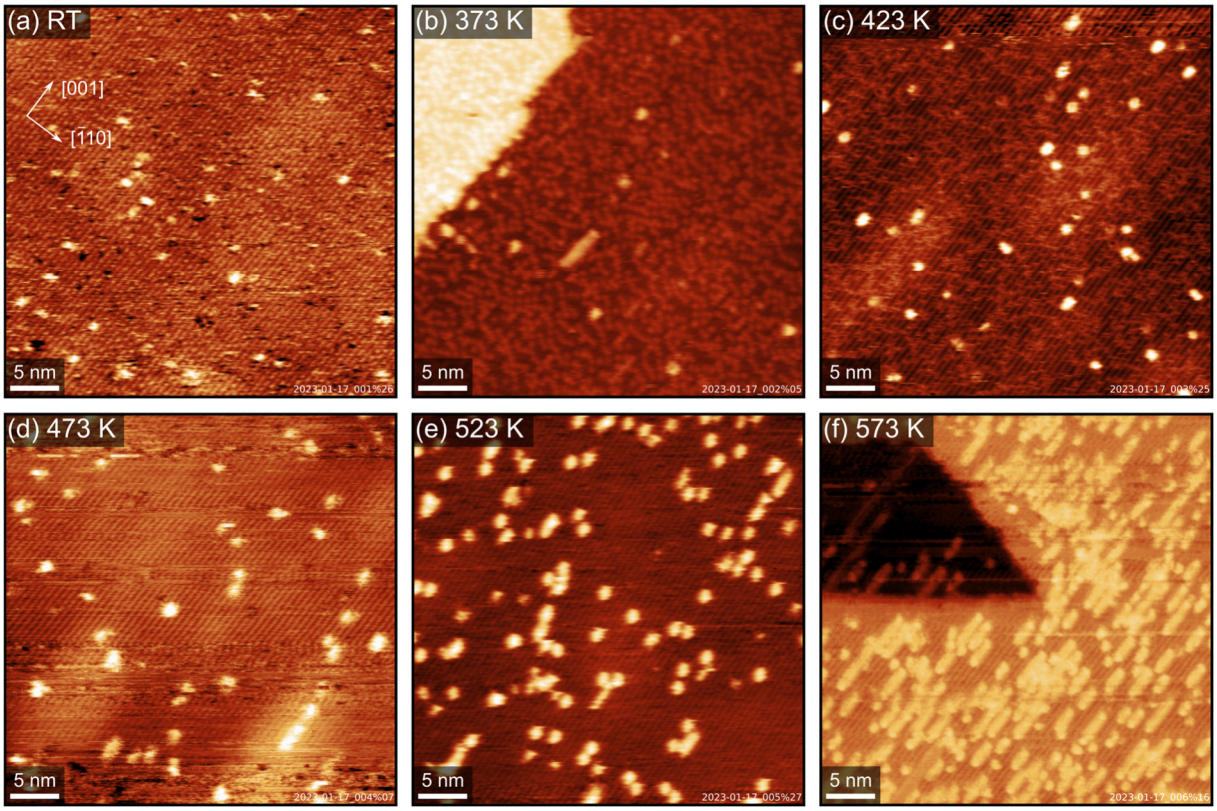

Figure S6. STM images of HR-TiO_2 in 1 mbar H_2 while heating to different temperatures. (a) RT; (b) 373 K, image acquired 7 minutes after reaching the temperature; (c) 423 K, image acquired after 27 minutes; (d) 473 K, image acquired after 13 minutes; (e) 523 K, image acquired after 21 minutes; (f) 573 K, image acquired after 74 minutes. Brightness modulations of the surface in (a), (c), (d) and (e) are due to Ar bubbles, which are typical for this surface after UHV preparation. Scanning parameters U_{sample} and I_{tunnel} were (a) 1.7 V, 0.2 nA, (b) 1.4 V, 0.1 nA, (c) 2.1 V, 0.2 nA, (d) 1.3 V, 1.0 nA, (e) 1.3 V, 0.9 nA and (f) 1.5 V, 0.7 nA.

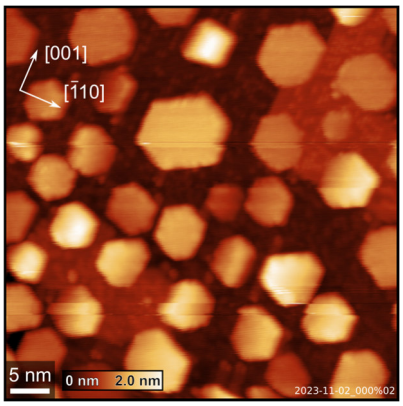

Figure S7. STM image showing Pt nanoparticles on HR-TiO_2, post-annealed at 1200 K in UHV for 30 minutes after the H_2 experiment shown in Figure 3. U_{sample} = 1.8 V, I_{tunnel} = 0.1 nA.

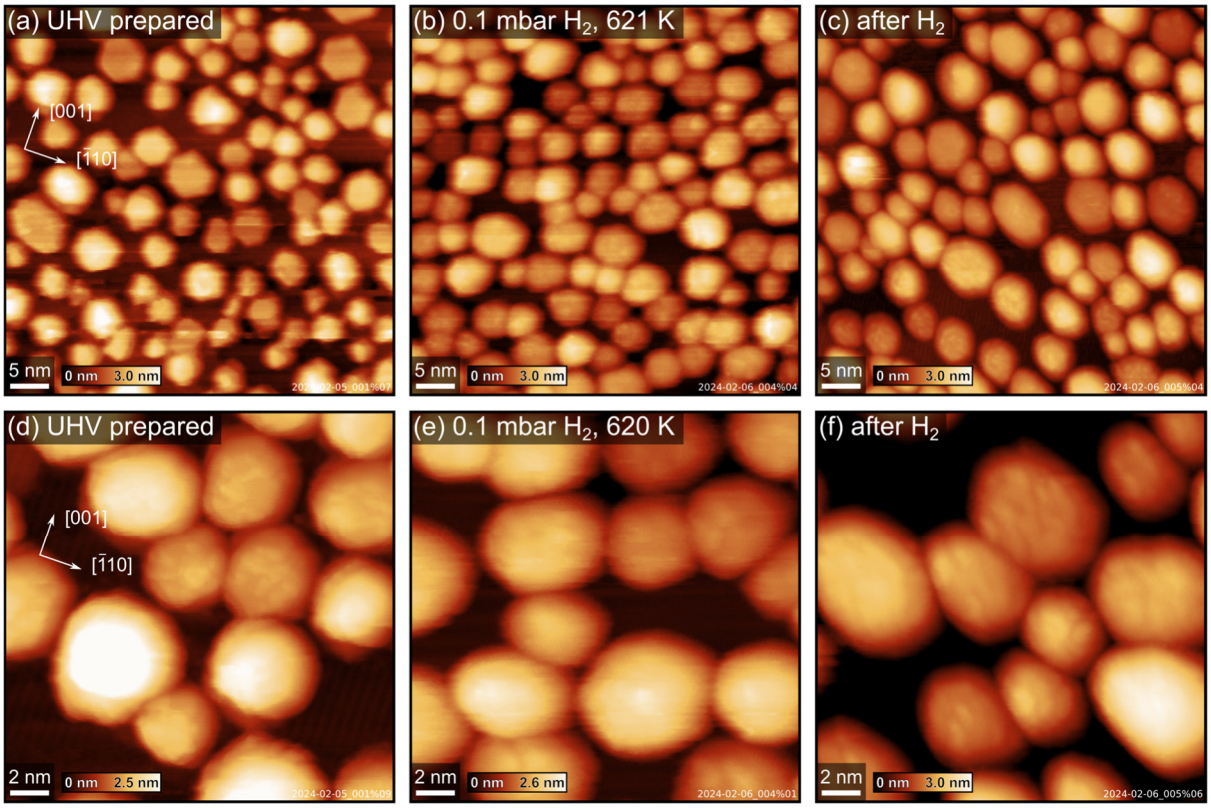

Figure S8. STM images showing the evolution of Pt nanoparticle on LR-TiO_2 in H_2. (a,d) As-sintered nanoparticles in UHV, annealed 30 minutes at 1000 K. (b,e) The same particles in 0.1 mbar H_2 at (e) 620 K, ≈15 minutes after the temperature reached 600 K and (b) 621 K, after ≈21 minutes. (c,f) Images acquired after cooling to room temperature and returning the sample to UHV after a total of 90 minutes at T ≥ 600 K in H_2. Some internal structure is resolved on some of the particles, but we did not find any well-defined superstructure. Scanning parameters U_{sample} and I_{tunnel} were (a) 1.4 V, 2.0 nA, (b) 1.4 V, 1.5 nA, (c) 1.2 V, 0.3 nA, (d) 1.4 V, 0.2 nA, (e) 1.4 V, 1.4 nA, (f) 1.2 V, 0.8 nA.

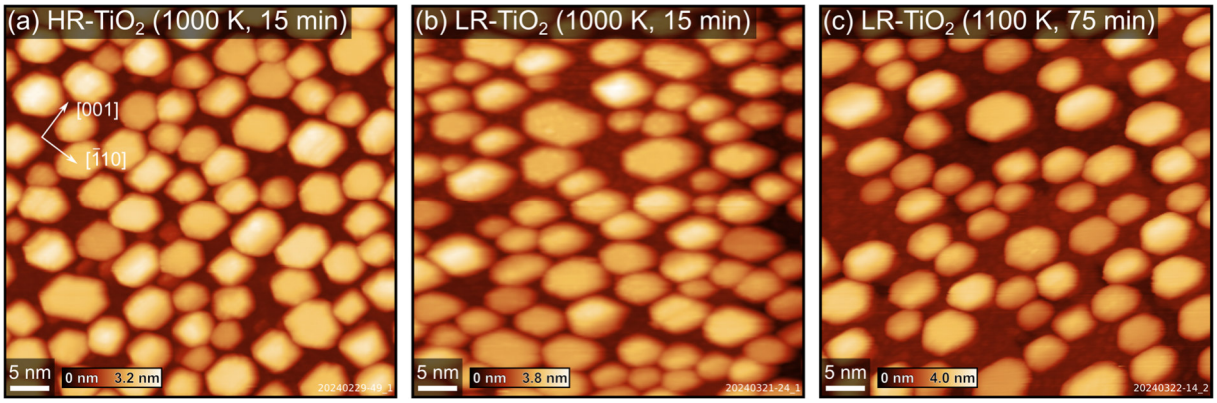

Figure S9. STM images of the Pt/LR-TiO_2 and Pt/HR-TiO_2 samples used in the $C^{18}O$ TPD experiments shown in Figure 4(a). (a) Pt particles on HR-TiO_2 after annealing in UHV at 1000 K for 15 minutes. (b) Pt particles on LR-TiO_2 after annealing in UHV at 1000 K for 15 minutes, and (c) after annealing in UHV at 1100 K for 75 minutes. Slight linear distortions in (b) and (c) are due to thermal drift of the STM scanner. Scanning parameters U_{sample} and I_{tunnel} were (a) 1.5 V, 1.0 nA and (b, c) 2.0 V, 0.3 nA.

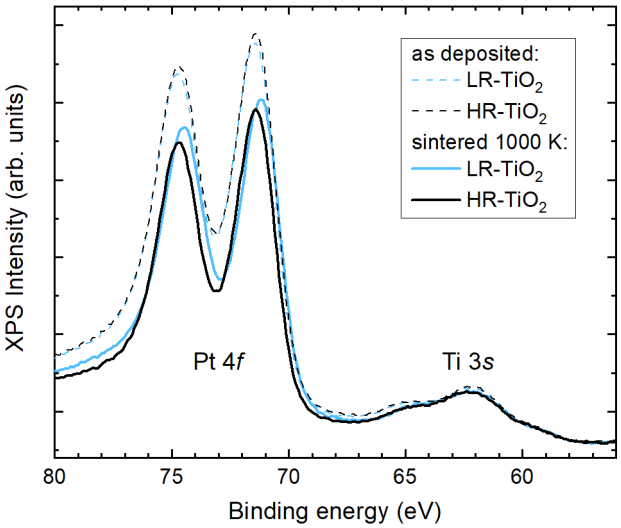

Figure S10. XPS (Al Kα, normal emission, 50 eV pass energy) of the Pt/LR-TiO_2 and Pt/HR-TiO_2 samples used in the $C^{18}O$ TPD experiments shown in Figure 4(a). Dashed lines show spectra acquired directly after depositing Pt. Solid lines show spectra acquired after annealing at 1000 K for 15 minutes. Note that the signal in the Ti 3*s* region is convoluted with duplicates of the Pt 4*f* peaks due to X-ray satellites from the non-monochromatic Al Kα source (α_3: ΔE = 9.8 eV, α_4: ΔE = 11.8 eV relative to $\alpha_{1,2}$, with relative intensities of 6.4% and 3.2%, respectively).[1]

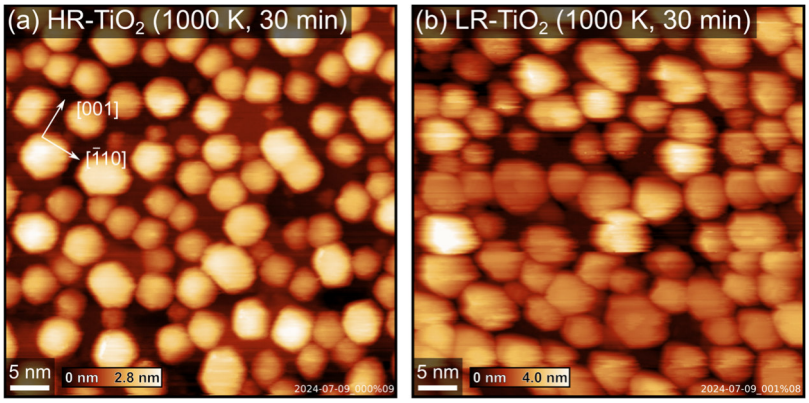

Figure S11. STM images of Pt/LR-TiO_2 and Pt/HR-TiO_2 corresponding to the LEIS data shown in Figure 4(b). (a) Pt particles on HR-TiO_2 after annealing in UHV at 1000 K for 30 minutes. (b) Pt particles on LR-TiO_2 after annealing in UHV at 1000 K for 30 minutes. Scanning parameters U_{sample} and I_{tunnel} were (a) 1.5 V, 1.2 nA and (b) 1.5 V, 0.9 nA.

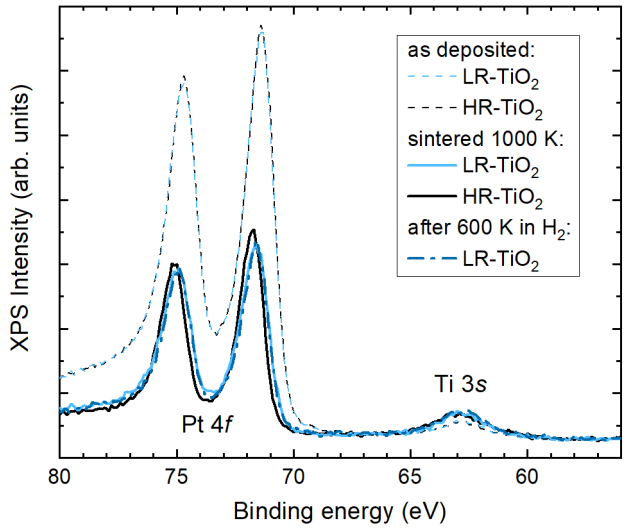

Figure S12. XPS (monochromated Al Kα, normal emission, 30 eV pass energy) of Pt/LR-TiO_2 and Pt/HR-TiO_2 corresponding to the LEIS data shown in Figure 4(b). Dashed lines show spectra acquired directly after depositing Pt. Solid lines show spectra acquired after annealing at 1000 K for 30 minutes. The dot-dashed, dark blue line was taken after exposing the LR-TiO_2 to 0.1 mbar H_2 and heating to 600 K for 30 minutes. Note the more pronounced difference between as-deposited and sintered Pt than seen in Figure S10, possibly indicating lower Pt loading in the TPD experiment.

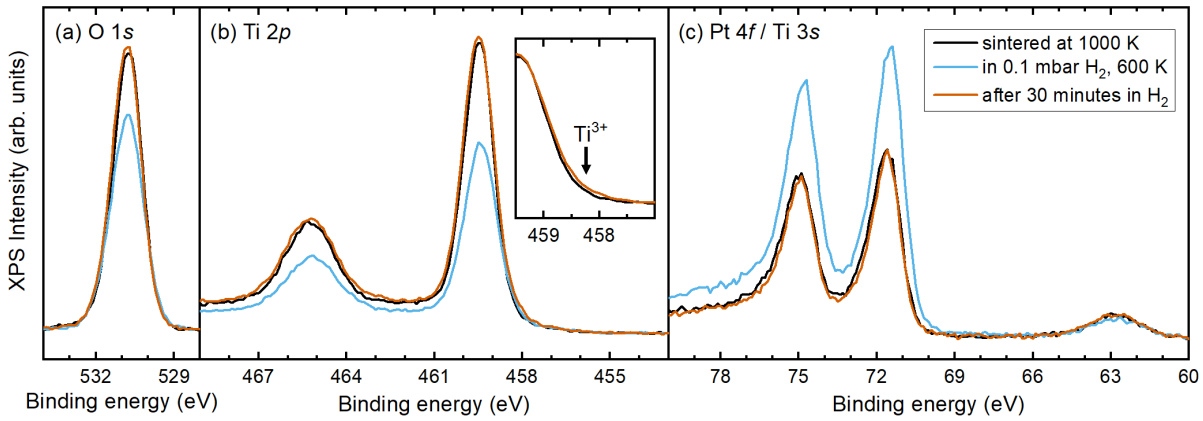

Figure S13. NAP-XPS (monochromated Al Kα, normal emission, 30 eV pass energy) of the (a) O 1s, (b) Ti 2p and (c) Pt 4f / Ti 3s regions of Pt/LR-TiO_2 exposed to 0.1 mbar H_2 at 600 K. The spectra before (black) and after (orange) H_2 exposure were acquired in UHV at room temperature, while the blue curve was acquired in 0.1 mbar H_2 at 600 K. The inset in panel (b) is a magnified view of the Ti $2p_{3/2}$ peak, indicating a slight increase in the Ti^{3+} component after H_2 exposure. The black and orange curves in panel (c) are the same as shown in Figure S12 and correspond to the LEIS data shown in Figure 4(b).

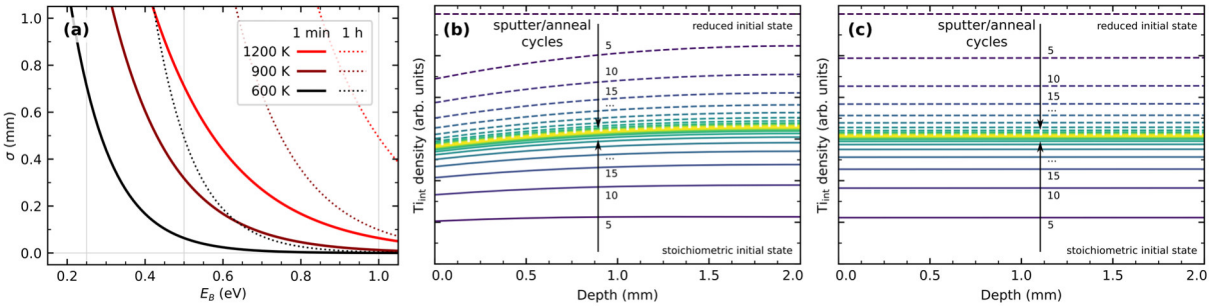

Figure S14. (a) Standard deviation σ for the position of a Ti_{int} interstitial diffusing perpendicular to the (110) surface in the bulk of rutile TiO_2(110) as a function of the activation barrier for bulk diffusion, shown for relevant temperatures and times. The interstitial is assumed to follow a one-dimensional random walk, resulting in a normal distribution with σ equivalent to the root mean square distance from the original position. (b) Simulated concentration profiles as shown in Figure 5 for a 2 mm thick rutile TiO_2(110) crystal after a given number of cycles of sputtering and annealing in O_2 for 20 minutes at 900 K. In contrast to Figure 5, here, the bulk diffusion barrier was set to 0.5 eV. The surface reaction barrier determining the rate of reoxidation was kept at 1 eV. Solid and dashed lines show equilibration when starting from a fully stoichiometric and from a homogeneously reduced initial state, respectively. (c) Same simulation as in (b), adding a 10 minute annealing step at 1100 K in each cycle. No further oxidation or reduction is assumed during this higher-temperature step.

Diffusion simulations

As discussed in the main manuscript, diffusion simulations of Ti_{int} were based on a one-dimensional random walk. This is a reasonable approximation when the diffusing particles are dilute enough that interaction between them is negligible. We further model the occupation of each layer as a floating-point concentration, rather than an integer number of diffusing particles. For each single Ti_{int}, the probability of finding it at a distance *z* from its original position is given by a normal distribution, with $\sqrt{\overline{\Delta z^2}} = \sigma = d\sqrt{n}$ after *n* steps, where *n* depends on the elapsed time, the diffusion barrier and temperature, and a preexponential factor (see main manuscript). We can then directly evaluate the concentration profile of a sample after a given annealing step by convolution of the initial concentration per layer with a normal distribution, setting the standard deviation σ to reflect annealing time and temperature. This effectively smears out each "particle" in the original concentration profile to reflect its likely position after annealing. Crucially, the result is exactly the same no matter if the concentration profile samples each atomic layer individually, or only every k^{th} layer, as long as σ is chosen according to the actual layer thickness. This treatment is therefore extremely computationally efficient, as only one calculation is required for each annealing step.

Edges of the sample must be accounted for specifically. The simplest boundary condition to implement is that when a particle at the surface (the 0^{th} layer) would diffuse out of the surface (to the -1^{st} layer), it is instead considered to still be in the 0^{th} layer. This is easily achieved by performing the convolution with the normal distribution, then "folding back" the negative space, such that all concentration in the -1^{st} layer is added to the 0^{th} layer, all concentration in the -2^{nd} layer is added to the 1^{st} layer, and so on. It is easy to see that this is still an exact solution, as any diffusion event from the -1^{st} layer is treated the same way as a diffusion event from the 0^{th} layer, with diffusion in one direction having no effect, and diffusion in the other direction leading away from the surface. Applying the same approach to the other edge of the crystal, we essentially obtain periodic boundary conditions, where the concentration is flipped in every other period. Again, this is still an exact solution within the bounds of the random walk approximation, no matter the point sampling density.

Modelling oxidation at the surface is more difficult. To avoid having to model a varying thickness of the sample, we approximate oxidation by some probability that every time a particle would diffuse out of the surface, it disappears instead of staying in the surface layer. It is trivial to choose this probability to

correspond to some surface reaction barrier by setting it to a Boltzmann factor $e^{-\varepsilon/k_B T}$, with ε being the difference between the bulk and surface barriers.

Ideally, we would implement this oxidation process in our model by applying that probability every time a particle passes through the surface, *i.e.* from the 0th to the −1st layer or vice versa. However, the approach of simply convolving a normal distribution then breaks down, as *e.g.* most atoms at the 0th layer that would remain at the 0th layer in the random walk approximation have actually passed through the origin at least once, and likely many times (assuming large *n*). This can be solved either by calculating the contributions of different paths to each point of the normal distribution and applying the loss probability accordingly, or by choosing small time steps, such that few atoms diffuse out of the surface in each step. Both approaches are computationally expensive. We have chosen the second, applying the loss factor twice in each time step to the concentration in the out-of-surface space to account for the symmetrical nature of the problem (*i.e.*, for each particle found in the −1st layer, one particle in the 0th layer is considered to have come from the −1st layer for an arbitrary initial distribution). This qualitatively captures the oxidation behaviour, especially in the limits of no oxidation (where the model is exact) or full oxidation (where every atom diffusing out of the surface is lost). However, for arbitrary surface reaction barriers, we accept some error in capturing the exact value of the barrier, because we do not correctly capture particles passing through the surface multiple times. The concentration models shown in Figure 5 and Figure S14 are still qualitatively correct within the limits of the approximation, but we only give concentrations as "arbitrary units" to reflect this error. Similarly, we model the reducing effect of sputtering simply by setting the concentration at the surface layer to an arbitrary (high) value, since we have no good estimate of how much excess Ti is introduced in each sputtering step.

1. J. F. Moulder, W. F. Stickle, P. E. Sobol and K. D. Bomben, *Handbook of X-ray Photoelectron Spectroscopy*, Perkin-Elmer Corporation, 1979.

6

Conclusions and Outlook

In summary, this thesis presents three studies in the field of model catalysis with a strong focus on the support material, ranging from a carbon-based over a non-reducible oxide to a reducible oxide. In the first one, we demonstrated a new, bottom-up synthesis of carbon nitride thin films by on-surface polymerization on Au(111) that has the potential as a novel support material for model studies in thermal, electro- and photocatalysis. We presented three different reaction pathways on Au(111): X-ray induced, UV-light induced with subsequent annealing, and thermal activation, all resulted in an amorphous, not fully closed, but largely homogeneous 2D film. In contrast, on HOPG, only X-rays and accompanying secondary electrons can activate the precursor molecule while preventing desorption at the same time. Also, the thus resulting film was only loosely connected, as STM tip displacement showed. Therefore, in order to obtain a fully metal-free support material, which would consist of a carbon nitride thin film on top of HOPG, additional optimization would be needed. One option might be to introduce defects on the HOPG surface prior to film synthesis, by, e.g., bombardment with Ar^+ or O^+ ions. A recent study showed that the thus modified HOPG surface shows an increased capability to anchor Pd nanoparticles while still being flat enough for STM.[96] On this defect-rich surface, the adhesion of the TAH precursor molecules as well as the resulting carbon nitride film might also be increased. Another possible optimization would be to increase the ordering of the building blocks in the final film in order to obtain more well-defined pores in which single atoms or clusters could be stabilized, which could be achieved by testing different annealing strategies and would allow more precise mechanistic studies on, for example, cross-coupling reactions. Nevertheless, even now, it is already planned to combine this carbon nitride thin film with cluster deposition from polyoxometalate

precursors[97] in an electrochemical environment to access studies on, e.g., electrochemical water splitting.

The second study draws a comparison of 2D silica films on Pt(111) and Rh(111). On Pt(111), we were able to optimize an established preparation method such that we now achieve fully closed, amorphous films that show a high stability against an atmosphere of CO in the near-ambient pressure range. We attributed the key factor to the excess deposition of Si, which can then form a silicate or silicide buffer layer between the Pt and the 2D silica. However, exposure to high temperatures results in the formation of holes in the film. On Rh(111), we could not optimize the synthesis to achieve fully closed films, but here additional 2D silica morphologies appeared: besides amorphous, as on Pt(111), also crystalline and "zigzag" regions were found. Furthermore, the 2D silica could be fully reduced on Rh(111) at high temperatures, which resulted in a surface silicide with $(\sqrt{19} \times \sqrt{19})R23.4^\circ$ periodicity. Upon this reduction, a large amount of Si was lost, either to the bulk or to the gas phase, in the form of SiO, which hindered recovery of the film by reoxidation, although full oxidation of the remaining silicide is possible. In consequence, these 2D silica films on Pt(111) and Rh(111) provide only limited suitability as a support in model catalysis as in both cases no fully closed films are stable at high temperatures. On Pt(111), small clusters could diffuse into the formed holes and have a strong interaction with the underlying metal, potentially influencing their properties drastically; the same holds true for the fully exposed Rh surface silicide. Indeed, preliminary results of size-selected Pt clusters, which we deposited on 2D silica on Pt(111), showed a high mobility and concomitant sintering even at room temperature. Similarly, size-selected Ta clusters have been deposited but seem to degrade the film at room temperature. With this differing behavior of the 2D silica films at high temperatures dependent on the underlying metal, this study clearly illustrates the importance of a good understanding of how the support responds under conditions that are closer to reactions in applied catalytic processes.

This fact is even more strongly emphasized in the third study. Here, we presented an altering surface reaction behavior for the same support material, namely rutile TiO_2, with just a slightly different stoichiometry. In atmospheres of CO_2, H_2 and

CO at near-ambient pressures and 600 K, only HR-TiO_2 showed a surface oxidation and reduction while LR-TiO_2 remained inert. Here, only in O_2 a slight surface oxidation appeared, which was much stronger in the case of HR-TiO_2. This difference in behavior also showed up in the interaction with Pt nanoparticles of 5–10 nm sizes. On HR-TiO_2, the SMSI-induced encapsulation already occurred upon UHV sintering after Pt deposition which was not the case for LR-TiO_2 where H_2 at 0.1 mbar and 600 K was needed. In this atmosphere, the Pt nanoparticles on HR-TiO_2 revealed an additional, deeper embedding into the oxide surface. In light of these results, it becomes clear that the extensive literature on SMSI of Pt on titania must be considered carefully. In particular, a lack of details on the sample stoichiometry often makes it difficult to gauge its reactivity. Notably, theoretical investigations typically do not take into account these defects, and thus, their results might diverge from experimental findings. Indeed, this is the topic of an ongoing collaboration with the theory group of Bjørk Hammer. Our current and future studies aim to investigate the influence of the stoichiometry even deeper, with measurements that contain more than one gas species and therefore resemble actual reaction mixtures. Here, we are specifically interested in building on the H_2 + O_2 study by Willinger and coworkers[46] as well as investigating the hydrogenation of CO_2. Finally, the question as to how transferable the results are from nanoparticles to clusters is of interest.

Overall, these three studies highlight the importance of controlling model catalyst supports down to the single atom. The precise knowledge of the atomic composition and defect identities, as well as densities, is one of the key advantages of model catalysis over investigations on realistic systems. As we have shown in the example of titania, even a small number of interstitials can completely change the reactivity and is, therefore, decisive for the outcome of the catalytic reaction. While the titania single crystals provide the most highly controlled supports, their dynamic composition changes in an ambient pressure redox environment, and hence, the support cannot be defined a priori independent from the reactants. In contrast, the non-reducible silica should be an inert support. However, in the attempt to create a conductive 2D analogon, its strong interaction with the underlying metal substrate can completely change its properties. Indeed, we have

seen that these 2D silica films are much less stable than one might think. For applications in liquids and electrochemical conditions, altogether different supports are needed. This is where the motivation for the carbon nitride film synthesis was based. In this case, the challenge lies mostly in forming a well-ordered and flat, regular network with highly defined anchoring centers. While none of these systems is universally applicable, the present thesis provides an invaluable foundation upon which NAP investigations can be built, extending the library of available supports for different studies.

In addition to these studies on model supports, I have built two new Faraday cups for cluster generation setups. Both are designed with three copper grids for a maximum amount of shielding when a retarding field is applied. The first one serves as an addition to a well-established laser ablation cluster source, enables optimization of cluster current during sample preparation and shows a remarkably good signal-to-noise ratio. The other Faraday cup, which will be installed in a new magnetron sputter source, also increases sample throughput by allowing parameter optimization while the load lock, where the sample is introduced, is pumped. With its five independent electrodes, it is additionally possible to characterize the cluster beam profile more accurately. Once completely built up, this setup will be used to enable studies of size-selected clusters in the NAP-STM.

Finally, I created several software packages and libraries that optimize data management and analysis with the experimental data produced by the used setup. On the one hand, they help to speed up the analysis workflow and make it more convenient, and on the other, they create a data management structure that is in line with the widely desired FAIR (Findable, Accessible, Interoperable, Reusable)[98] principles as they allow parsing of proprietary file formats and store experimental data and metadata together. As such, this thesis attempts to set an example for fully transparent and sustainable data management and makes our findings available and verifiable for future generations.

Bibliography

[1] C. Marcilly, *J. Catal.* **2003**, *216*, 47–62, DOI 10.1016/S0021-9517(02)00129-X.

[2] M. G., *Stud. Surf. Sci. Catal.* **2000**, *130*, 83–103, DOI 10.1016/S0167-2991(00)80946-5.

[3] J. Humphreys, R. Lan, S. Tao, *Adv. Energy Sustain. Res.* **2021**, *2*, 2000043, DOI 10.1002/aesr.202000043.

[4] F. Dalena, A. Senatore, A. Marino, A. Gordano, M. Basile, A. Basile, *Methanol Production and Applications: An Overview*, Elsevier B.V., **2018**, pp. 3–28, DOI 10.1016/B978-0-444-63903-5.00001-7.

[5] C. A. Busacca, D. R. Fandrick, J. J. Song, C. H. Senanayake, *Adv. Synth. Catal.* **2011**, *353*, 1825–1864, DOI 10.1002/adsc.201100488.

[6] B. Martín-Matute, M. A. Meier, T. X. Métro, S. G. Koenig, H. F. Sneddon, P. Sudarsanam, P. Watts, *ACS Sustain. Chem. Eng.* **2021**, *9*, 13395–13398, DOI 10.1021/acssuschemeng.1c06526.

[7] G. Centi, P. Ciambelli, S. Perathoner, P. Russo, *Catal. Today* **2002**, *75*, 3–15, DOI 10.1016/S0920-5861(02)00037-8.

[8] A. F. Lee, K. Wilson, *Catal. Today* **2015**, *242*, 3–18, DOI 10.1016/j.cattod.2014.03.072.

[9] R. Mülhaupt, *Macromol. Chem. Phys.* **2003**, *204*, 289–327, DOI 10.1002/macp.200290085.

[10] D. R. Vardon, N. A. Rorrer, D. Salvachúa, A. E. Settle, C. W. Johnson, M. J. Menart, N. S. Cleveland, P. N. Ciesielski, K. X. Steirer, J. R. Dorgan, G. T. Beckham, *Green Chem.* **2016**, *18*, 3397–3413, DOI 10.1039/c5gc02844b.

[11] W. Reschetilowski, *Einführung in die Heterogene Katalyse*, Springer Spektrum, Berlin, **2015**, DOI 10.1007/978-3-662-46984-2.

[12] J. M. Thomas, *Proc. R. Soc. A Math. Phys. Eng. Sci.* **2012**, *468*, 1884–1903, DOI 10.1098/rspa.2012.0196.

[13] U. A. MacRae, *Science* **1963**, *139*, 379–388, DOI 10.1126/science.139.3553.379.

[14] K. Siegbahn, K. Edvarson, *Nucl. Phys.* **1956**, *1*, 137–159, DOI 10.1016/s0029-5582(56)80022-9.

[15] G. Binnig, H. Rohrer, *Angew. Chemie Int. Ed. English* **1987**, *26*, 606–614, DOI 10.1002/anie.198706061.

[16] P. Hohenberg, W. Kohn, *Phys. Rev.* **1964**, *136*, B864, DOI 10.1103/PhysRev.136.B864.

[17] W. Kohn, L. J. Sham, *Phys. Rev.* **1965**, *140*, A1133, DOI 10.1103/PhysRev.140.A1133.

[18] W. P. Halperin, *Rev. Mod. Phys.* **1986**, *58*, 533–606, DOI 10.1103/RevModPhys.58.533.

[19] M. Valden, X. Lai, D. W. Goodman, *Science* **1998**, *281*, 1647–1650, DOI 10.1126/science.281.5383.1647.

[20] J. F. Eckhard, T. Masubuchi, M. Tschurl, R. N. Barnett, U. Landman, U. Heiz, *J. Phys. Chem. C* **2018**, *122*, 25628–25637, DOI 10.1021/acs.jpcc.8b07729.

[21] H. Häkkinen, M. Moseler, O. Kostko, N. Morgner, M. A. Hoffmann, B. V. Issendorff, *Phys. Rev. Lett.* **2004**, *93*, 1–4, DOI 10.1103/PhysRevLett.93.093401.

[22] W. Huang, M. Ji, C. D. Dong, X. Gu, L. M. Wang, X. G. Gong, L. S. Wang, *ACS Nano* **2008**, *2*, 897–904, DOI 10.1021/nn800074b.

[23] H. Häkkinen, S. Abbet, A. Sanchez, U. Heiz, U. Landman, *Angew. Chemie - Int. Ed.* **2003**, *42*, 1297–1300, DOI 10.1002/anie.200390334.

[24] H. R. Siekmann, C. Lüder, J. Faehrmann, H. O. Lutz, K. H. Meiwes-Broer, *Zeitschrift für Phys. D Atoms Mol. Clust.* **1991**, *20*, 417–420, DOI 10.1007/BF01544026.

[25] U. Heiz, F. Vanolli, L. Trento, W. D. Schneider, *Rev. Sci. Instrum.* **1997**, *68*, 1986–1994, DOI 10.1063/1.1148113.

[26] C. Zhang, H. Tsunoyama, H. Akatsuka, H. Sekiya, T. Nagase, A. Nakajima, *J. Phys. Chem. A* **2013**, *117*, 10211–10217, DOI 10.1021/jp406521v.

[27] S. M. Lang, T. M. Bernhardt, *Phys. Chem. Chem. Phys.* **2012**, *14*, 9255–9269, DOI 10.1039/c2cp40660h.

[28] J. F. Eckhard, T. Masubuchi, M. Tschurl, R. N. Barnett, U. Landman, U. Heiz, *J. Phys. Chem. A* **2021**, *125*, 5289–5302, DOI 10.1021/acs.jpca.1c02384.

[29] G. Ertl, *Angew. Chemie - Int. Ed.* **2008**, *47*, 3524–3535, DOI 10.1002/anie.200800480.

[30] M. Bowker, A. Dickinson, D. James, R. D. Smith, P. Stone, R. A. Bennett, *Stud. Surf. Sci. Catal.* **2001**, *133*, 3–17, DOI 10.1016/s0167-2991(01)81946-7.

[31] Z. Gao, G. Wang, T. Lei, Z. Lv, M. Xiong, L. Wang, S. Xing, J. Ma, Z. Jiang, Y. Qin, *Nat. Commun.* **2022**, *13*, 1–9, DOI 10.1038/s41467-021-27785-5.

[32] U. Heiz, E. L. Bullock, *J. Mater. Chem.* **2004**, *14*, 564–577, DOI 10.1039/b313560h.

[33] S. Kaiser, F. Maleki, K. Zhang, W. Harbich, U. Heiz, S. Tosoni, B. A. J. Lechner, G. Pacchioni, F. Esch, *ACS Catal.* **2021**, *11*, 9519–9529, DOI 10.1021/acscatal.1c01451.

[34] A. S. Crampton, M. D. Rotzer, U. Landman, U. Heiz, *ACS Catal.* **2017**, *7*, 6738–6744, DOI 10.1021/acscatal.7b01844.

[35] K. Chen, Z. Chai, C. Li, L. Shi, M. Liu, Q. Xie, Y. Zhang, D. Xu, A. Manivannan, Z. Liu, *ACS Nano* **2016**, *10*, 3665–3673, DOI 10.1021/acsnano.6b00113.

[36] F. Polo-Garzon, T. F. Blum, Z. Bao, K. Wang, V. Fung, Z. Huang, E. E. Bickel, D. E. Jiang, M. Chi, Z. Wu, *ACS Catal.* **2021**, *11*, 1938–1945, DOI 10.1021/acscatal.0c05324.

[37] J. C. Matsubu, S. Zhang, L. DeRita, N. S. Marinkovic, J. G. Chen, G. W. Graham, X. Pan, P. Christopher, *Nat. Chem.* **2017**, *9*, 120–127, DOI 10.1038/NCHEM.2607.

[38] J. Zhu Chen, A. Talpade, G. A. Canning, P. R. Probus, F. H. Ribeiro, A. K. Datye, J. T. Miller, *Catal. Today* **2021**, *371*, 4–10, DOI 10.1016/j.cattod.2020.06.075.

[39] S. D. Kaiser, PhD thesis, Technische Universität München, **2023**, https://mediatum.ub.tum.de/1719858.

[40] S. Tauster, S. Fung, R. Garten, *J. Am. Chem. Soc.* **1978**, *100*, 170–175, DOI 10.1021/ja00469a029.

[41] S. Tauster, *Acc. Chem. Res.* **1987**, *20*, 389–394, DOI 10.1021/ar00143a001.

[42] O. Dulub, W. Hebenstreit, U. Diebold, *Phys. Rev. Lett.* **2000**, *84*, 3646–3649, DOI 10.1103/PhysRevLett.84.3646.

[43] M. Bowker, *Chem. Soc. Rev.* **2007**, *36*, 1656–1673, DOI 10.1039/b412139m.

[44] K. Zhang, S. Shaikhutdinov, H. J. Freund, *ChemCatChem* **2015**, *7*, 3725–3730, DOI 10.1002/cctc.201500328.

[45] P. Petzoldt, M. Eder, S. Mackewicz, M. Blum, T. Kratky, S. Günther, M. Tschurl, U. Heiz, B. A. J. Lechner, *J. Phys. Chem. C* **2022**, *126*, 16127–16139, DOI 10.1021/acs.jpcc.2c03851.

[46] H. Frey, A. Beck, X. Huang, J. A. van Bokhoven, M. G. Willinger, *Science* **2022**, *376*, 982–987, DOI 10.1126/science.abm3371.

[47] X. Wang, K. Maeda, A. Thomas, K. Takanabe, G. Xin, J. M. Carlsson, K. Domen, M. Antonietti, *Nat. Mater.* **2009**, *8*, 76–80, DOI 10.1038/nmat2317.

[48] X. Wang, S. Blechert, M. Antonietti, *ACS Catal.* **2012**, *2*, 1596–1606, DOI 10.1021/cs300240x.

[49] P. Kumar, E. Vahidzadeh, U. K. Thakur, P. Kar, K. M. Alam, A. Goswami, N. Mahdi, K. Cui, G. M. Bernard, V. K. Michaelis, K. Shankar, *J. Am. Chem. Soc.* **2019**, *141*, 5415–5436, DOI 10.1021/jacs.9b00144.

[50] H. Schlomberg, J. Kröger, G. Savasci, M. W. Terban, S. Bette, I. Moudrakovski, V. Duppel, F. Podjaski, R. Siegel, J. Senker, R. E. Dinnebier, C. Ochsenfeld, B. V. Lotsch, *Chem. Mater.* **2019**, *31*, 7478–7486, DOI 10.1021/acs.chemmater.9b02199.

[51] Z. Chen, E. Vorobyeva, S. Mitchell, E. Fako, M. A. Ortuño, N. López, S. M. Collins, P. A. Midgley, S. Richard, G. Vilé, J. Pérez-Ramírez, *Nat. Nanotechnol.* **2018**, *13*, 702–707, DOI 10.1038/s41565-018-0167-2.

[52] S. M. Hosseini, M. Ghiaci, H. Farrokhpour, *Mater. Res. Express* **2019**, *6*, 105079, DOI 10.1088/2053-1591/ab3cbd.

[53] K. W. Kolasinski, *Surface Science: Foundations of Catalysis and Nanoscience*, Second Ed., John Wiley and Sons, **2012**, DOI 10.1002/9781119941798.

[54] M. E. Grass, P. G. Karlsson, F. Aksoy, M. Lundqvist, B. Wannberg, B. S. Mun, Z. Hussain, Z. Liu, *Rev. Sci. Instrum.* **2010**, *81*, 053106, DOI 10.1063/1.3427218.

[55] S. Bonanni, K. Aït-Mansour, M. Hugentobler, H. Brune, W. Harbich, *Eur. Phys. J. D* **2011**, *63*, 241–249, DOI 10.1140/epjd/e2011-10532-7.

[56] J. Reich, S. Kaiser, U. Heiz, J. D. Grunwaldt, M. M. Kappes, F. Esch, B. A. J. Lechner, *Top. Catal.* **2024**, *67*, 880–891, DOI 10.1007/s11244-024-01920-0.

[57] M. König, PhD thesis, Technische Universität München, **2015**, https://mediatum.ub.tum.de/1256288.

[58] A. Bourgund, PhD thesis, Technische Universität München, **2020**, https://mediatum.ub.tum.de/1535053.

[59] G. Binnig, H. Rohrer, *Surf. Sci.* **1983**, *126*, 236–244, DOI 10.1016/0039-6028(83)90716-1.

[60] B. Voigtländer, *Scanning probe microscopy*, Springer-Verlag Berlin Heidelberg, **2015**, DOI 10.1002/9783527612451.ch3.

[61] M. Salmeron, B. Eren, *Chem. Rev.* **2021**, *121*, 962–1006, DOI 10.1021/acs.chemrev.0c00429.

[62] B. J. McIntyre, M. Salmeron, G. A. Somorjai, *Rev. Sci. Instrum.* **1993**, *64*, 687–691, DOI 10.1063/1.1144198.

[63] C. T. Herbschleb, P. C. Van Der Tuijn, S. B. Roobol, V. Navarro, J. W. Bakker, Q. Liu, D. Stoltz, M. E. Cañas-Ventura, G. Verdoes, M. A. Van Spronsen, M. Bergman, L. Crama, I. Taminiau, A. Ofitserov, G. J. Van Baarle, J. W. Frenken, *Rev. Sci. Instrum.* **2014**, *85*, 083703, DOI 10.1063/1.4891811.

[64] M. Rössler, P. Geng, J. Wintterlin, *Rev. Sci. Instrum.* **2005**, *76*, 023705, DOI 10.1063/1.1841951.

[65] E. Laegsgaard, L. Österlund, P. Thostrup, P. B. Rasmussen, I. Stensgaard, F. Besenbacher, *Rev. Sci. Instrum.* **2001**, *72*, 3537–3542, DOI 10.1063/1.1389497.

[66] SPECS Surface Nano Analysis GmbH, https://www.specs-group.com/nc/specs/products/detail/spm-aarhus-150-nap/ (visited on 08/16/2024).

[67] X. Ma, S. Günther, *Phys. Chem. Chem. Phys.* **2018**, *20*, 21844–21855, DOI 10.1039/c8cp03197e.

[68] A. Einstein, *Ann. Phys.* **1905**, *322*, 132–148, DOI 10.1002/andp.19053220607.

[69] J. W. Niemantsverdriet, *Spectroscopy in Catalysis: An Introduction*, Third Ed., Wiley-VCH Verlag, **2007**, DOI 10.1002/9783527611348.

[70] S. Hüfner, *Photoelectron spectroscopy*, Third Ed., Springer-Verlag Berlin Heidelberg, **2003**, DOI 10.1007/978-3-662-09280-4.

[71] M. Seah, W. Dench, *Surf. Interface Anal.* **1979**, *1*, 2–11, DOI 10.1002/sia.740010103.

[72] D. E. Starr, *ACS Symp. Ser.* **2021**, *1396*, 1–17, DOI 10.1021/bk-2021-1396.ch001.

[73] H. Siegbahn, *Proc. Soc. Anal. Chem.* **1985**, *89*, 897–909, DOI 10.1021/j100252a005.

[74] R. W. Joyner, M. W. Roberts, K. Yates, *Surf. Sci.* **1979**, *87*, 501–509, DOI 10.1016/0039-6028(79)90544-2.

[75] H. J. Ruppender, M. Grunze, C. W. Kong, M. Wilmers, *Surf. Interface Anal.* **1990**, *15*, 245–253, DOI 10.1002/sia.740150403.

[76] J. Pantförder, S. Pöllmann, J. F. Zhu, D. Borgmann, R. Denecke, H. P. Steinrück, *Rev. Sci. Instrum.* **2005**, *76*, 014102, DOI 10.1063/1.1824351.

[77] D. F. Ogletree, H. Bluhm, G. Lebedev, C. S. Fadley, Z. Hussain, M. Salmeron, *Rev. Sci. Instrum.* **2002**, *73*, 3872–3877, DOI 10.1063/1.1512336.

[78] H. Bluhm, M. Hävecker, A. Knop-Gericke, E. Kleimenov, R. Schlögl, D. Teschner, V. I. Bukhtiyarov, D. F. Ogletree, M. Salmeron, *J. Phys. Chem. B* **2004**, *108*, 14340–14347, DOI 10.1021/jp040080j.

[79] D. F. Ogletree, H. Bluhm, E. D. Hebenstreit, M. Salmeron, *Nucl. Instruments Methods Phys. Res. Sect. A Accel. Spectrometers Detect. Assoc. Equip.* **2009**, *601*, 151–160, DOI 10.1016/j.nima.2008.12.155.

[80] P. Auger, *J. Phys. le Radium* **1925**, *6*, 205–208, DOI 10.1051/jphysrad:0192500606020500.

[81] Staib Instruments GmbH, https://www.staibinstruments.com/energy-analyzers-with-cylindrical-mirror-symmetry-cma/ (visited on 08/16/2024).

[82] K. Oura, V. G. Lifshits, A. A. Saranin, A. V. Zotov, M. Katayama, *Surface Science*, First Ed., Springer-Verlag Berlin Heidelberg, **2003**, DOI 10.1007/978-3-662-05179-5.

[83] D. Necas, P. Klapetek, *Cent. Eur. J. Phys.* **2012**, *10*, 181–188, DOI 10.2478/s11534-011-0096-2.

[84] matkrin/gwy-z-module, https://github.com/matkrin/gwy-z-module (visited on 10/01/2024).

[85] N. Bock, PhD thesis, Technische Universität München, **2021**, https://mediatum.ub.tum.de/1595316.

[86] matkrin/proespm-py3, https://github.com/matkrin/proespm-py3 (visited on 10/01/2024).

[87] matkrin/quickplot, https://github.com/matkrin/quickplot (visited on 10/01/2024).

[88] A. Savitzky, M. J. E. Golay, *Anal. Chem* **1964**, *36*, 1627–1639, DOI 10.1021/ac60214a047.

[89] matkrin/xps-peaks, https://github.com/matkrin/xps-peaks (visited on 10/01/2024).

[90] matkrin/spm-rs, https://github.com/matkrin/spm-rs (visited on 10/01/2024).

[91] K. L. Brown, G. W. Tautfest, *Rev. Sci. Instrum.* **1956**, *27*, 696–702, DOI 10.1063/1.1715674.

[92] V. N. Popok, I. Barke, E. E. Campbell, K. H. Meiwes-Broer, *Surf. Sci. Rep.* **2011**, *66*, 347–377, DOI 10.1016/j.surfrep.2011.05.002.

[93] U. Heiz, U. Landman, *Nanocatalysis*, First Ed., Springer-Verlag Berlin Heidelberg, **2007**, DOI 10.1007/978-3-540-32646-5.

[94] A. Sattler, PhD thesis, Ludwig-Maximilians-Universität München, **2010**, https://edoc.ub.uni-muenchen.de/11666/.

[95] T. Saplinova, V. Bakumov, T. Gmeiner, J. Wagler, M. Schwarz, E. Kroke, *Zeitschrift fur Anorg. und Allg. Chemie* **2009**, *635*, 2480–2487, DOI 10.1002/zaac.200900311.

[96] M. Kettner, C. Stumm, M. Schwarz, C. Schuschke, J. Libuda, *Surf. Sci.* **2019**, *679*, 64–73, DOI 10.1016/j.susc.2018.08.022.

[97] N. Bock, A. De Clercq, L. Seidl, T. Kratky, T. Ma, S. Günther, U. Kortz, U. Heiz, F. Esch, *ChemElectroChem* **2021**, *8*, 1280–1288, DOI 10.1002/celc.202100131.

[98] M. D. Wilkinson, M. Dumontier, I. J. Aalbersberg, G. Appleton, M. Axton, A. Baak, N. Blomberg, J. W. Boiten, L. B. da Silva Santos, P. E. Bourne, J. Bouwman, A. J. Brookes, T. Clark, M. Crosas, I. Dillo, O. Dumon, S. Edmunds, C. T. Evelo, R. Finkers, A. Gonzalez-Beltran, A. J. Gray, P. Groth, C. Goble, J. S. Grethe, J. Heringa, P. A. t Hoen, R. Hooft, T. Kuhn, R. Kok, J. Kok, S. J. Lusher, M. E. Martone, A. Mons, A. L. Packer, B. Persson, P. Rocca-Serra, M. Roos, R. van Schaik, S. A. Sansone, E. Schultes, T. Sengstag, T. Slater, G. Strawn, M. A. Swertz, M. Thompson, J. Van Der Lei, E.

Van Mulligen, J. Velterop, A. Waagmeester, P. Wittenburg, K. Wolstencroft, J. Zhao, B. Mons, *Sci. Data* **2016**, *3*, 160018, DOI 10.1038/sdata.2016.18.

Acknowledgements

First, I want to thank Barbara Lechner for giving me the chance to work in her group and for her excellent supervision during my PhD studies. With her passion for our work, she always provided guidance and help, no matter what time. Also, I want to thank Friedrich Esch for his mentorship, his inspiring enthusiasm, and his invaluable guidance, particularly on STM-related things. Many thanks to all other members of the Functional Nanomaterial group, especially my colleagues in the same STM lab, Johanna Reich and Sebastian Kaiser, who created an enjoyable work environment at all times. In particular, I want to thank Florian Kraushofer. With his profound knowledge, he contributed a lot to this work and it was a pleasure working with him. Furthermore, I want to thank all Bachelor and internship students as well as visitors that I supervised during my studies: Vivian Meier, Alina Bach, Moritz Bohn, Aya Haj Abdulkader, Elisabeth Springl, Patrick Micheler, Sofia Beliakova, Matthias Füchsl, Agnieszka Jarosz, Jiming Liu, Xinran Liu, Umi Shin and Nathan Durand Brousseau. Special thanks to Howe Simpson and Nils Refvik from the University of Alberta for their great contributions during their visit in our group and for welcoming me to the University of Alberta.

I am also very grateful to Ueli Heiz and all members of his chair for their welcoming spirit, which made me always feel like I was part of two groups. Here, special thanks to Robert Spitzenpfeil and Christian Schmid for their immensely helpful technical support. The same is true for our electrical workshop and the mechanical workshops of the chemistry department and the WSI who I thank for their excellent work, especially on the parts for both Faraday cups.

I also want to thank Jeppe Lauritsen for hosting me during a short stay in Aarhus and Sigmund Jensen, one of his PhD at the time, who introduced me to their work with the NAP-STM. Many thanks also to Moni Blum for hosting my colleagues and

me at the ALS several times and for instructing us on the use of the NAP-XPS setup there. Last but not least, I thank Frank Hegmann for welcoming me into his group on my research exchange through the ATUMS program at the University of Alberta. I thoroughly enjoyed my time in his fantastic group.

Statement on AI Tool Usage

During the writing process of this thesis, the AI tools ChatGPT, DeepL, and Grammarly were employed for language refinement and translation purposes. The content generated by these tools was never used verbatim. Instead, all suggestions were carefully evaluated and adjusted to ensure clarity, accuracy, and adherence to academic standards.